CARL VON OSSIETZKY universität OLDENBURG

Experimental and theory-based studies of silicic acid formation under hydrothermal conditions – evaluation of various methods

Von der Fakultät für Mathematik und Naturwissenschaften der Carl von Ossietzky Universität Oldenburg zur Erlangung des Grades und Titels

Doktors der Naturwissenschaften

-Dr. rer. nat-

angenommene

Dissertation

von

Herrn

M.Sc. Jaybalan Tamahrajah

geb. am 13.04.1985

in Kuala Lumpur, Malaysia

Oldenburg, September 2015

Erstgutachter:	Apl. Prof. Dr. Axel Brehm
Zweitgutachter:	Prof. Dr. Michael Wark
Promotionsausschuss:	Prof. Dr. Thorsten Klüner

Tag der Disputation: 30. 10. 2015

1 INTRODUCTION 1

2 OBJECTIVE OF RESEARCH WORK 5

3 FUNDAMENTALS OF HYDROTHERMAL CONDITIONS 14

3.1 THERMODYNAMICS 14
3.1.1 SOLUBILITY 15
3.1.2 REACTION EQUILIBRIA 16
3.1.2.1 Multiple reaction equilibria 17
3.1.3 PHASE EQUILIBRIUM 18
3.1.3.1 Phase equilibria of pure components 18
3.1.3.2 Phase equilibria of mixtures 20
3.2 HYDROTHERMAL CONVERSION OF SILICIC ACID SPECIES 21
3.3 QUANTUM CHEMISTRY 29
3.3.1 QUANTUM CHEMICAL METHODS 29
3.3.2 SOLVENT EFFECTS 29
3.4 EVALUATION OF POSSIBLE EXPERIMENTAL METHODS FOR THE CHARACTERISATION OF SILICIC ACID SPECIES 30
3.4.1 DETERMINATION OF CONCENTRATION VIA UV-VIS SPECTROSCOPY 30
3.4.2 DETERMINATION OF SILICIC ACID SPECIES VIA ESI-MS SPECTROSCOPY 30
3.4.3 DETERMINATION OF THE DISSOCIATION CONSTANT OF TOTAL SILICIC ACID SPECIES BY MEANS OF A ELECTROCHEMICAL CELL - POTENTIOMETRY 32
3.4.3.1 The cell potential in the presence of stainless steel - corrosive conditions 36
3.4.4 DETERMINATION OF TOTAL SILICIC ACID SPECIES IN THE VAPOUR PHASE 41

4 RESULTS 42

4.1 RESULTS QUANTUM CHEMICAL CALCULATION OF SILICIC ACID SPECIES 42
4.1.1 DETERMINATION OF THE STANDARD GIBBS FREE ENERGY, ENTHALPY, AND ENTROPY FOR CYCLISATION AND CONDENSATION REACTIONS 43
4.1.2 QUANTUM CHEMICAL VALUES FOR DISSOCIATION CONSTANT CALCULATIONS WITH SOLVENT EFFECTS 51
4.2 EXPERIMENTAL RESULTS 57
4.2.1 LIQUID PHASE EXPERIMENTS 57
4.2.1.1 Solubility experiments 57
4.2.1.1.1 Setup of apparatus at 25°C 57
4.2.1.1.2 Setup of apparatus for measurements from 60°C to 170°C 58

4.2.1.1.3 Results of solubility measurements 60
4.2.1.1.3.1 UV-Vis Results 60
4.2.1.1.3.2 ESI-MS (Electron Spray Ionisation- Mass Spectrometry) results 61
4.2.1.2 Results from electrochemical measurements – potentiometry 72
4.2.1.2.1 Setup of experimental apparatus 72
4.2.1.2.2 The streaming potential 76
4.2.1.2.3 Calibration measurements 76
4.2.1.2.4 Measurements with silica source (dried at 105°C (24h) and calcined at 550°C (24h) LUDOX AS-40) 77
4.2.1.2.5 Results of potentiometry 79
4.2.1.3 Proof of corrosion effects 85
4.2.1.3.1 The electrochemical potential measurement (ECP) of iron corrosion by means of linear sweep measurements 87
4.2.1.3.2 SEM and EDX-measurements 90
4.2.1.3.3 IR measurements. 92
4.2.1.3.4 Raman measurements 93
4.2.1.4 Reaction equilibria 95
4.2.2 RESULTS FROM VAPOUR PHASE EXPERIMENTS 99
4.2.2.1 Vapour phase equilibrium measurements of total silicic acid species 99
4.2.2.1.1 Setup of Quartz Crystal Microbalance 99
4.2.2.1.2 Experimental Results of Quartz Crystal Microbalance 101
4.2.2.1.3 VLE Results 101

5 CONCLUSION AND OUTLOOK 102

6 REFERENCES 109

7 APPENDIX 116

7.1 LINEAR FITTING OF SOLUBILITY DATA DETERMINED BY THE UV-VIS METHOD 116
7.2 CORROSION EFFECTS 117
7.2.1 TAFEL PLOTS 117
7.2.2 CORROSION MODEL 118
7.3 WATER SORPTION RESULTS – FOR LUDOX AS 40 121
7.4 XRD DATA OF LUDOX AS-40 121
7.5 FITTING EQUATIONS FROM ESI-MS DATA 122
7.6 IMAGES OF CORROSION OF HIGH TEMPERATURE CELL AND GLASS CELL STAINLESS STEEL ELECTRODES 123

7.7 VLE CALCULATION DATA 123
7.8 FORMATION AND REACTION ENERGIES FROM QUANTUM CHEMICAL CALCULATIONS..... 124
7.8.1 THE COMPARISON OF THE TEMPERATURE DEPENDENT LNK WITH THE HOFF EQUATION 126
7.8.2 COMPARISON OF LNK, $LNK_{298.15K}$ AND LNK_p FOR CYCLIC TRISILICIC (CYCLOTRISILICIC) AND FUSED-CYCLIC PENTASILICIC (CYCLOPENTASILICIC) ACID 127
7.8.3 DERIVATION OF THE SECOND LAW FROM THE VAN'T HOFF EQUATION 128

8 NOMENCLATURE 128

Hear the 9th Symphony,
Beethoven, deaf was he,
How can a deaf man ever,
Be able to show that one can defy
The notes of impossibility
It is to show that if only one was in the valley
That one can appreciate the comforts of acme

Foreword

This work is done between the period of April 2011 and August 2015 in the Multiphase Chemical Reaction Engineering working group of Prof. Dr. Axel Brehm in the Institute of Chemistry at the Carl von Ossietzky University of Oldenburg.

I thank Prof. Dr. Axel Brehm for the opportunity of performing research in his group and the interesting choice of topic in the field of Industrial Chemistry. His support during the course of this work was monumental.

I would like to thank Prof. Dr. Michael Wark for accepting the role of a second supervisor. I would like to thank the group of Prof. Dr. Wark and especially Dr. Dereje Taffa for useful discussions on electrochemistry.

I thank Prof. Dr. Throsten Klüner and his working group for providing me the resources and knowledge of theoretical chemistry with great patience for me to proceed with my work.

Many thanks to the Wittstock group for providing the necessary instruments for UV-Vis measurements and platinising procedures and the group of Prof. Wark for providing instruments of water sorption measurements as well as linear sweep electrochemical potential measurements. I also thank the group of Prof. Dr. Beckhaus for providing instruments for IR-measurements, Next Energy-EWE Forschungszentrum für Energietechnologie e.V. for Raman measurements and the Biology Department for SEM and EDX measurements.

I would like to thank the group of Prof. Dr. Christoffers, especially Dipl.-Ing. Francesco Fabretti for ESI-MS measurements. I would also like to thank the group of Prof. Wickleder for XRD measurements. I certainly would like to thank the current Technical Chemistry Group of Prof. Dr. Wark and the previous group of Prof. Dr. Jürgen Gmehling for the friendly working atmosphere and useful insights in chemistry and chemical thermodynamics.

I would like to thank the mechanical, electronic and carpentry workshops of the University for the design and construction of reactors, controllers and wooden housing for the apparatuses used in this work.

I thank the current and previous members of the Brehm Group of Chemical Reaction Engineering, especially MSc. Benjamin Burfeind and MSc. Jan Ohlert for the great, cooperative team-spirited work conditions and treasured ideas acquired from the group. I would like to thank MSc. Daniel Rosenkranz for his useful insights to this work

The good atmosphere provided by new and old friends in Oldenburg, Bremerhaven and Malaysia during these times has lent a helping hand during this period. Last but not least, I would like to thank my family for their support during my academic stay in Germany.

1 Introduction

Processes occurring by hydrothermal means (presence of water, heat and autogenous pressure) [1] are controlled by thermodynamic parameters, which is the inter-relation of pressure, temperature, pH and composition in a system of interest. As conventional of a method as it may be, it serves a useful purpose to understand the behaviour of chemical substances in a solution or system at hydrothermal conditions existing in equilibrium. Thermodynamic calculations at hydrothermal conditions provide the first hints of possibility for a reaction to occur and the magnitude in which it occurs.

Hydrothermal phenomena occur in nature with elevated temperatures and pressure occurring in natural basins with the presence of water. Natural products at compositions given by thermodynamics are produced under these conditions, which constitute the natural environment. Hydrothermal carbonisation (HTC) [2] is a valuable method to upgrade organic waste [3] such as waste water sludge[4]. Latest research focuses on the hydrothermal carbonisation of agricultural waste products [5]. Even silicates of different forms such as amorphous silica, crystalline quartz, and opals form under hydrothermal conditions. Formation of silicates at different hydrothermal conditions especially their condensation from soluble silicic acid species offers a wide range of purposes. Silicates have been used for medical purposes (for tuberculosis) and investigated by geologist and chemist. Natural zeolites offer a good example for the formation of chemical substances under hydrothermal conditions by taking advantage of equilibrium reactions in the ecosystem. Soluble silicates at hydrothermal conditions (silicic acid) play an important role in the formation of these silicates, especially zeolites. The reaction pathways during the formation of zeolites remain a matter of discussion [6]. Thermodynamic investigations concerning silicic acid provide a good starting point for the elucidation of the reaction paths of silicates and even zeolites. This work attempts to show the feasibility of different theoretical and experimental approaches. This is done by comparing each approach separately (between theories and between experiments) and then comparing between approaches (between theory and experiment)

Zeolites are natural occurring minerals in natural geological basins in voids or cavities of basaltic and volcanic rock at suitable hydrothermal conditions and alkalinity ([7]-p.175). Even under the sea, near volcanic regions, the temperatures are sufficient for hydrothermal equilibrium conditions, in which zeolites form. Early on, scientists have tried to mimic hydrothermal conditions and synthesise crystalline porous materials for specific applications. The term zeolite comes from the Greek term “zeo” - stone and “lithos”, which translates to be

boiling stone defined by Crønsted in 1756. It is observed that water is removed from the silicates as they were heated, which is the dehydration of the respective zeolite.
Zeolites are important porous materials in the field of industrial chemistry, renewable and sustainable energy. They consists of TO_4 tetrahedra primary units (T is often Si or Al), which make up the microporous zeolite structure through secondary building units and hence the known zeolite structures [8, 9]. They are crystalline materials, in which their structures are characterised by connections of linking TO_4 tetrahedra. These consist of a metal cation bonded with 4 oxygen atoms, surrounding it. The scaffold-like structure form hollow spaces in the form of channels and cage structures. The channels are of sufficient size to allow guest molecules to enter the spaces. For hydrated phases, the reversible dehydration can occur at temperatures under 400°C.

As useful as they are, the proper reaction mechanism during the hydrothermal syntheses of zeolites remains to be an issue of discussion ([6, 10-12]; 10-p.39-241). The T-units and the explicit reaction mechanism are still of doubt as recent findings show different forms of primary building units [13-19].
This work attempts to explore the reaction mechanisms in the first stages of zeolite syntheses. The reactants and product of the syntheses are considered and classical and modern measuring methods and theoretically derived information are used to understand the syntheses pathway.
This work focusses on the initial stages of zeolite syntheses. If the reaction path can be found, specific tailor-made porous networks can be produced for their specific applications in catalysis and adsorption of chemical compounds. Possible pathways are to be verified based on chemical thermodynamics. Kinetics of silica dissolution is considered in order to determine the equilibrium of the dissolution and its calculations are disregarded. Since the dissolution of the silica is a basic requirement for the hydrothermal synthesis of zeolites, appropriate investigations are chosen as a starting point. The advantage of this is that the same procedure could be used for more complex blends or synthetic solutions. Nor it is confined to the complex blends of zeolite syntheses. This procedure takes a universal approach to elucidating unknown reaction paths. The work has achieved to determine the methods needed to elucidate the reaction path. A combination of the classical and state of the art experimental and theoretical methods with the validation of literature data for their (between classical and state of the art) consistency has been the main task of this work.
Chapter 2 attempts to show the objective of the research work and the path taken in this work. Chapter 3 encompasses all aspects based on silicic acid, covering the thermodynamics of

phase equilibria and reaction equilibria, the reactions for silicic acid conversion and quantum chemical theory. This chapter is considered to be of significance for the fundamentals of zeolite syntheses. Chapter 4 discusses the results of thermodynamic properties in the liquid and vapour phases and quantum chemical calculations. Results in both phases in equilibrium (Vapour and Liquid Equilibria) are also analysed. In Chapter 5, a conclusion of this work is given and an outlook for further research is given as well. References, appendix and nomenclature are divided into chapters 6, 7 and 8 respectively.

Einleitung

Prozesse unter hydrothermalen Bedingungen [1] (in Gegenwart von Wasser, Wärme und autogenem Druck) sind von Parametern wie Temperatur, Druck, pH und Zusammensetzung des Reaktionsgemisches abhängig. Thermodynamische Berechnungen zeigen die Parameterbereiche auf, für die Reaktionen unter hydrothermalen Bedingungen möglich sind. Hydrothermaler Bedingungen können in Laborautoklaven erzeugt werden, sind aber auch unter geothermalen Bedingungen in der Natur zu finden. Die hydrothermale Carbonisierung (HTC) [2] dient der Aufarbeitung von kohlenwasserstoffhaltigen Reststoffen [3], wie beispielsweise von Klär- und Faulschlämmen [4]. Weitere aktuelle Untersuchungen beschäftigen sich mit der Synthese von hydrothermal karbonisierten Produkten aus Grünschnitt u. a., die als torfähnliches Bodenzusatzmaterial für die Landwirtschaft bereitgestellt werden können [5]. Silikate, wie amorphe SiO_2, Quartz, Opale bildeten sich ebenfalls unter hydrothermalen Bedingungen in der Natur. Dabei spielen die Reaktionen der gelösten Kieselsäure sowie das mögliche Auftreten von SiO_2-Spezies in der Dampfphase eine wichtige Rolle. Hier bieten thermodynamische quantenmechanische Berechnungen eine praktikable Möglichkeit, um zum Verständnis der Reaktionswege der Kieselsäurespezies zu den Silikaten und sogar zu den Zeolithen beizutragen. Deshalb ist auch für das Verständnis der Zeolithsynthese die Aufklärung der Bildungsmechanismen hydrothermal entstandener Silikate von grundlegender Bedeutung. Die Reaktionsmechanismen bei der Herstellung von Zeolithen sind zurzeit in der Diskussion [6].

Zeolithe (Zeo – Gestein, lithos – siedende) wurde von Crønstedt als siedende Gesteine im Jahr 1756 bezeichnet. Diese Bezeichnung basiert auf der Eigenschaft von Zeolithen (bei Temperaturänderung) reversibel Wasser abzugeben bzw. aufzunehmen, ohne dass diese dabei ihre Kristallstruktur verlieren bzw. ändern. Zeolithe sind als natürliche Mineralien in geologischen Hohlräumen basaltischer (vulkanischer) Gesteine zu finden [7]. Während der

Entstehung dieser Gesteine treten hydrothermale Bedingungen auf, die ihre Bildung ermöglichen. Synthetisch hergestellte Zeolithe haben in den letzten Jahrzehnten diverse Anwendungen gefunden und werden in sehr großem Maßstab industriell synthetisiert. Sie werden als Katalysatoren und als Adsorber unter anderem in der Raffinerietechnik, der organischen Synthesechemie, zum Trocknen von Gasen, zum Temperieren und im Umweltschutz verwendet.

Zeolithe bestehen aus primären Baueinheiten (PBU) (TO_4-Tetraeder, mit T ≙ meist Si- und Al-Zentralatome), die zu sekundären Baueinheiten (SBU) verknüpft werden [8, 9]. Diese dienen wiederum als Bausteine und kombinieren zu kristallinen Gerüststrukturen mit definierten Kanälen und/oder käfigartigen Hohlräumen. Dieser Reaktionsweg ist zwar prinzipiell unumstritten, der detaillierte Mechanismus zur Bildung der SBU´s wird aber kontrovers diskutiert [6, 10-12]. Diese Diskussionen wurden in den letzten Jahren dadurch angeregt, dass verschiedene Kieselsäurespezies identifiziert werden konnten [13-19].

In dieser Arbeit werden die verschiedenen theoretischen und experimentellen Untersuchungsmethoden für die Bestimmung der Reaktionsmechanismen in Hinblick auf ihre Umsetzbarkeit angewendet und verglichen. Die Untersuchungen ziehen sowohl die Reaktionsabläufe in der flüssigen als auch in der Dampfphase ein und berücksichtigen das Phasengleichgewichtsverhalten (VLE). Sie sind dabei fokussiert auf die Initialisierung der Zeolithsynthese und der hier auftretenden SiO_2-Spezies. Darauf basierend werden die Reaktionsmechanismen qualitativ postuliert. Diese werden mit publizierten Aussagen verglichen.

Da die Auflösung von amorphem Silika als initialer Schritt von hoher Wichtigkeit ist, wird dies als erstes Fundamental näher beleuchtet. Anschließend werden die Reaktionsgleichgewichte mit Hilfe thermodynamischer Berechnungen ermittelt, um die möglichen chemischen Mechanismen zu verifizieren. Die Ergebnisse können auf Lösungen mit komplexen Mischungen erweitert werden. Daneben werden in dieser Arbeit die experimentellen Methoden zur Bestimmung der Reaktionsmechanismus evaluiert. Die Evaluierung zwischen klassischen und modernen experimentellen Methoden, deren vergleichende Bewertung sowie das Einbeziehen theoriebasierter (computergestützter) Prädiktiven thermodynamischen Berechnungen sowie der Untersuchungen der

Quantenmechanik sind Hauptaufgaben dieser Arbeit. Die Kinetik der Entstehung der reaktiven Spezies wird nicht verfolgt.

Kapitel 2 definiert die Zielsetzung der Arbeit und erklärt die Wege und Methoden, die in dieser Arbeit genutzt wurde. Kapitel 3 umfasst alle Aspekte der Thermodynamik der Kieselsäure - Phasengleichgewicht, Reaktionsgleichgewicht, postulierte Reaktionen der Kieselsäureumsetzung bis zu den quantenchemischen Berechnungen zur Kieselsäure und deren Spezies. Kapitel 4 beschreibt die erhaltenden Resultate. Im Kapitel 5 werden die Ergebnisse verglichen und diskutiert. Ferner werden in einem Ausblick die Potentiale für weiterführende Forschungsarbeiten aufgezeigt. Das Literaturverzeichnis, Anhänge insbesondere zu den experimentellen Methoden sowie eine Auflistung der verwendeten Nomenklatur befinden sich in den Kapiteln 6, 7 und 8.

2 Objective of research work

The objective of this work is to evaluate the feasibility of methods to elucidate the thermodynamic pathways for the initialisation of zeolite syntheses. This is done by evaluating the results of the respective methods. The most important reactants in hydrothermal zeolite syntheses are taken for the evaluation.

The thermodynamics of dissolved silica is to be investigated further by theoretical and experimental means with conventional and state of the art methods. The respective methods provide insights on the initialisation of hydrothermal zeolite syntheses. The insights are the specific thermodynamic pathways taken to initialise the formation of zeolites. The determinations of these pathways provide useful information to systematically produce tailor-made zeolites for specific purposes. The tailor made zeolite may ease the environmental challenges confronted by mankind today.

The reactant is amorphous silica ($SiO_{2(am)}$) and water reacting into its dissolved form, which is silicic acid. This system of $SiO_{2(am)}/H_2O$ is chosen as literature data are abundant for comparison. It is important to start with a simple system to evaluate the methods through comparison of reliable data. The evaluation can be further extended to more complex blends for zeolite syntheses precursors.

The thermodynamics of silica has been and still being extensively investigated in literature [20-29]. The solubility of silica in different forms (amorphous, quartz, α-cristobalite) is shown with great accuracy in these literatures. They show that the solubility of silica, especially amorphous silica, which is of importance in this investigation, is low at mild conditions, however increasing with temperature.

Apart from temperature, the pH value can be increased to increase the solubility further. It is also possible to increase the pressure for further increase in solubility. This is however at extreme pressure conditions and will not be considered here due to the investigation at mild conditions for zeolite syntheses and to assure of the validity of the van't Hoff equation.

Due to the low solubility, other precursors are used to increase the amount of silicic acid in the solution such as sodium silicate and tetraalkylorthosilicates. Sodium silicates can be in their solid form or amorphous silica can be homogeneously dispersed and stabilized in a sodium hydroxide solution (HS-LUDOX) or ammonium hydroxide solution (AS-LUDOX). This serves well as a precursor in zeolite syntheses. The common chemical formula given for zeolites is:

$$M^{\upsilon+}_{nAl_2O/\upsilon}\left[\left(AlO_2\right)^{-}_{nAl_2O}\left(SiO_2\right)_{nSiO_2}\right]\bullet n_{H_2O,ZEO}H_2O$$

The expression in the squared brackets defines the number of tetrahedra in the unit cell. The quotient x_{SiO2}/x_{Al2O} describes the module. The silica to alumina (Si/Al) ratio of smaller than 1 is not possible according to Löwenstein's rule, as Al-O-Al bonds cannot occur due to energetic purposes. The ratio of SiO_2 and Al_2O_3 is defined as the module. *M* represents the metal cation, which possesses the oxidation number υ of one or two, hence giving the charge of the metal cation. It does not take part in formation of the scaffold structure of the zeolite, but the structure can only be neutralised through the insertion of Al_2O^- into the anionic network. The number of hydrated water molecules is represented by $n_{H2O,ZEO}$.

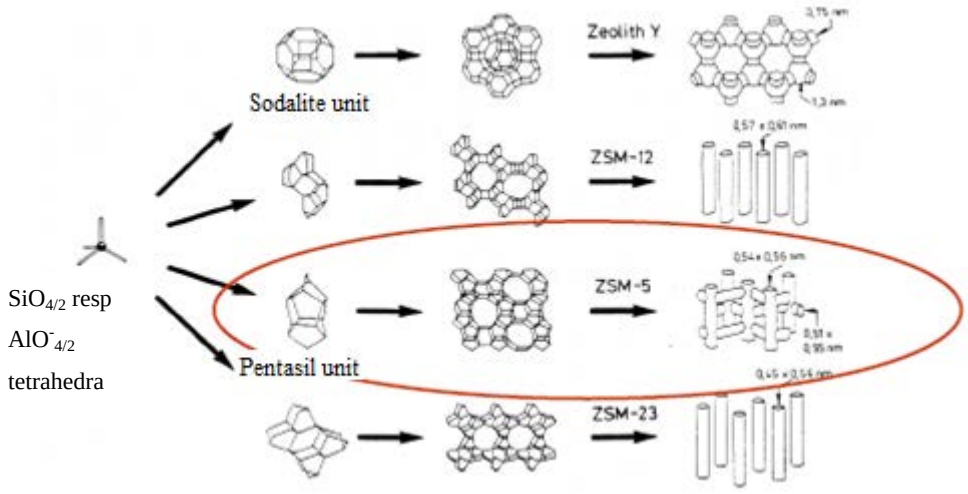

Figure 2-1 – The different secondary building units forming different zeolite compounds [30].

Different zeolite structures are possible just through the number of TO_4-linkage possibilities. These tetrahedra are known as the primary building units (PBU). They continue to form secondary building units (SBU) and further towards zeolite structures, depicted in figure 2-1. However, if the zeolite building structures are independent of these structural definitions, there may be a smooth transition by reaction mechanisms from the PBUs to the SBUs.

These may be condensation reactions from the PBUs to the SBUs rather than a clear distinction between the two units. There are currently 191 known natural and synthetic zeolite structures, abbreviated with three capital letters (e.g. MOR). One of the most useful zeolite known today is the Zeolite Socony Mobil-5, abbreviated as ZSM-5. The synthesis of ZSM-5 was first reported in a patent by Argauer and Landolt in 1972 [31].

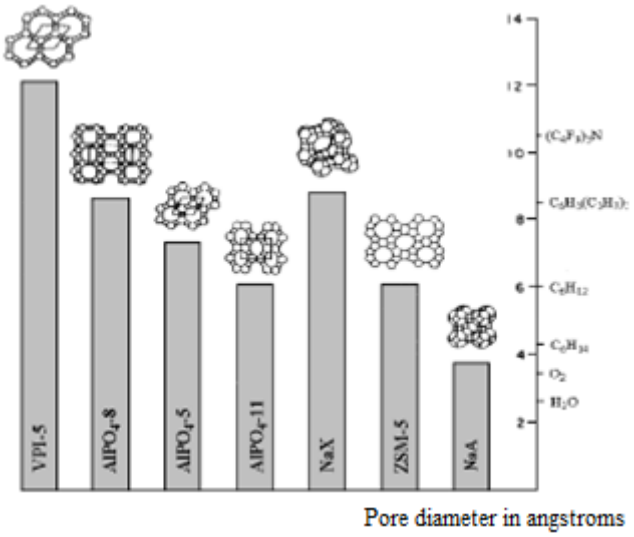

Figure 2-2 – The effective pore diameter and appropriate molecules which access the pore passage for aluminosilicates, aluminophosphates [32].

Zeolites, such as ZSM-5 (eight 5-ring pentasil SBU-MFI type framework) provide means of producing useful products, separation of mixtures and purifying chemical compounds. They are used in refineries, power plants, as catalyst and adsorption materials ([33]-p.226). The multiple application fields for zeolites occurred from their useful properties of:

- Mobile cations
- Large pore surface area
- Defined pore structure and hollow spaces in molecular dimension. These allow guest molecules to enter the hollow spaces (see figure 2-2)
- Regenerative catalytic active sites
- High thermal and hydrothermal stability.

The synthesis of zeolites by the hydrothermal method is the most common method used currently. Another special method include the sol-gel zeolite syntheses, in which the temperature is lower, however, the control of the crystallisation process (rapid condensation to amorphous materials) prove to be more difficult than in hydrothermal processes.

Typical reactants for the zeolite syntheses are Si-O and Al-O containing precursors, which are added to an alkaline solution from 50°C to 200°C. The alkali is normally alkaline metal hydroxides, which serve as a mineraliser, in which the transport of the precursors are

facilitated. Furthermore, templates are usually added to direct the structure formation (hence the term structure-directing agent), which is of interest and specified prior to the syntheses. The formula of the reactants is as follows:

$$n_{Al_2O_3}\, Al_2O_3 : n_{SiO_2}\, SiO_2 : n_M\, M_{2/\upsilon}O : n_{OR}\, OR : n_{H_2O}\, H_2O$$

M represents the cation with the charge of υ, OR is the template, which is an organic chemical compound. The reaction time may vary from a few hours to a few weeks depending on the composition, reaction conditions and the zeolite of interest. Reactions beginning at 100°C and above are conducted in a Teflon-protected stainless-steel reaction autoclave, in which the reaction takes place under autogenous pressure (vapour pressure property of solution given by the reaction temperature).

The specific transformation of the amorphous precursors into crystalline zeolites remains eluded despite attempts of describing the mechanism. However, a universal general scheme agreed by the zeolite community is divided into 3 phases:

1. Induction phase
- Formation of gel or colloid phase through rigorous mixing of reactants (figure 2-3a)
- Achievement of a quasi-stationary equilibrium between the amorphous region of the Si-O and Al-O bonds and the pre-stages and dissolved silicic acid ion and aluminosilicic acid anions through repeating and reversible condensation and hydrolysis, cyclisation and dissociation reactions (bonding and cleavage of T-O-T bonds). The importance of this work lies at this point.
- Development of partially crystalline scaffold structures.

2. Nuclei formation phase
- Formation of adequately defined phases and further regions capable of growth (figure 2-3b)

3. Growth phase
- Growth of nuclei and suppression of amorphous phase (figure 2-3c and d).

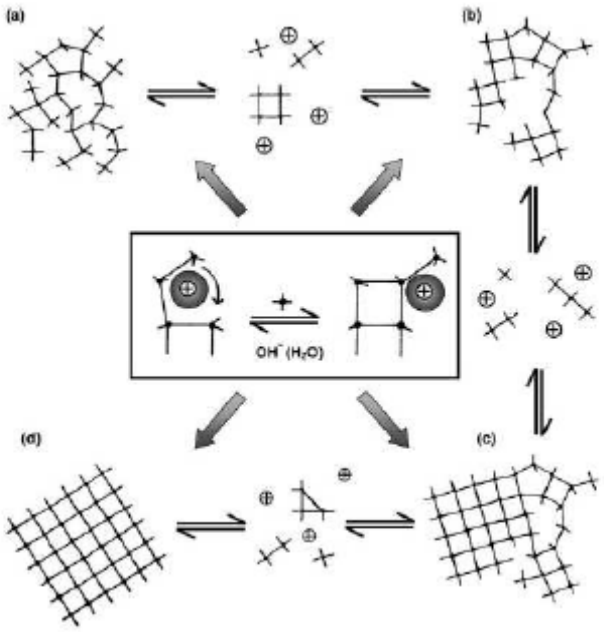

Figure 2-3 – The figure shows the complete depiction of the reaction mechanism during hydrothermal zeolite syntheses [6].

The cations and template play a structure directing role in the syntheses. The developed structure accumulate by addition of existing silicate and aluminosilicate anions through successive exchange of the hydrate capsule in order to achieve the new aluminosilicate (new T-units) structure of lowest energy at given conditions. The crystalline structure is formed around the cation through the reaction equilibria of the above figure (figure 2-3).

A review [6] revealed a general description on the reaction path of zeolite syntheses under hydrothermal conditions (see Figure 2-4). The initial stages of the syntheses pathway will be taken into account in this work according to this scheme of Cundy and Cox [6]. In this work, the methods used are to validate its feasibility to elucidate the initial pathway only.

Many researches from the field such as Cundy and Cox [6] and Mintova [12] have attempted to describe the complete reaction pathway of hydrothermal zeolite syntheses. Althoff et al. have even suggested that zeolite syntheses in the vapour phase are possible in the presence of hydrogen fluoride [34].

This work does not attempt to elucidate the whole reaction pathway. This work attempts to compare and validate all available methods (both theoretical and experimental – see figure 2-5) for feasibility of these methods to study the beginning of the zeolite syntheses pathway.

To achieve this target, it is important to have the knowledge of the chemical components involved in the hydrothermal zeolite syntheses. One must find a method to understand the behaviour of these components in a complex simultaneous equilibria involving condensation steps [12].

It is decided to take the thermodynamic pathway in order to understand the SiO_2/H_2O system under hydrothermal conditions. These conditions are at different temperatures, surpassing the normal boiling point of the solvent involved (H_2O) and different pH-values as zeolite syntheses are performed at higher alkalinity. This system is chosen because the formation of zeolites is negligible in a $SiO_{2(am)}/H_2O$ system known in literature.

Hence, the position III is non-existent and equilibrium conditions actually exist between position I and II (see figure 2-4). This thermodynamic pathway is chosen, as it is a simple form of a black box investigation that is performed without prior details of the system being investigated.

The thermodynamic results from a qualitatively assumed equilibrium reaction model are compared with actual experimental results. With this comparison, details behind the system are deduced after analysing the thermodynamic data. It is also chosen as literature data are available for the system considered in this work. This has a similar approach of Šefcík [21].

I:-amorphous SiO_2 →II:-dissolved SiO_2/silicic acid →III:-porous scaffold structures (zeolites)

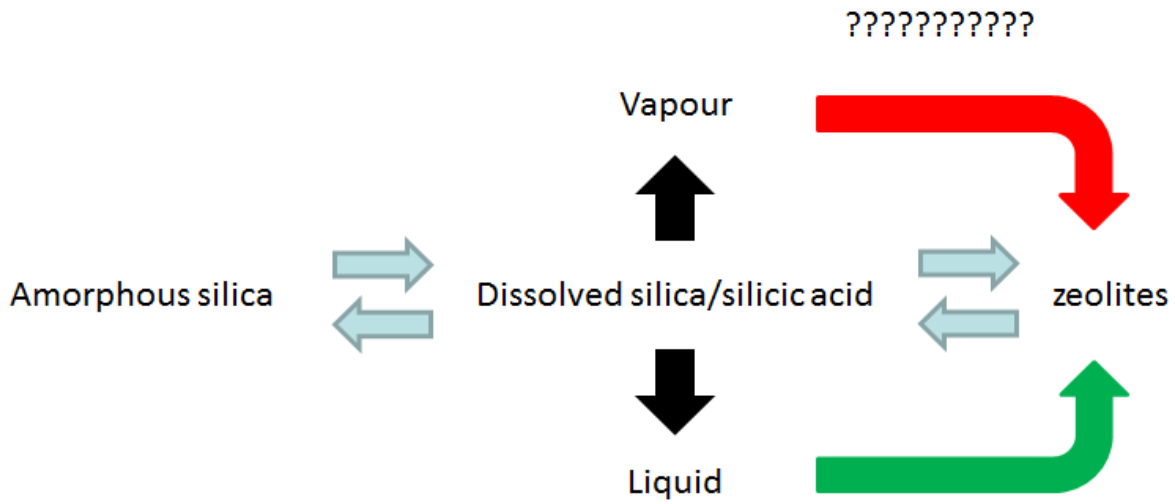

Figure 2-4 – The simplified version of zeolite syntheses pathway with a synergy of pathways postulated by Cundy and Cox[6] as well as Althoff, Unger, and Schüth [34].

Emphasis and focus is put on the initialisation pathway denoted from I to II in Figure 2-4. The elucidation of the specific primary building units (PBUs) at position I and II at hydrothermal conditions is identified by theoretical and experimental methods available in literature. The theoretical and experimental results are compared.

The interplay of the silicic acid species between the liquid and vapour phase at equilibrium under hydrothermal conditions is investigated. Therefore, multiphase thermodynamic equilibrium is taken into account. If the initialisation of the syntheses pathway could be understood by means undertaken by this work, it will direct further work for targeted hydrothermal syntheses of zeolites for specific purposes and open a new area of tailor made zeolites synthesised hydrothermally.

The chemical thermodynamics tool used in this work deserves a separate subsection, as it is an important feature in this study.

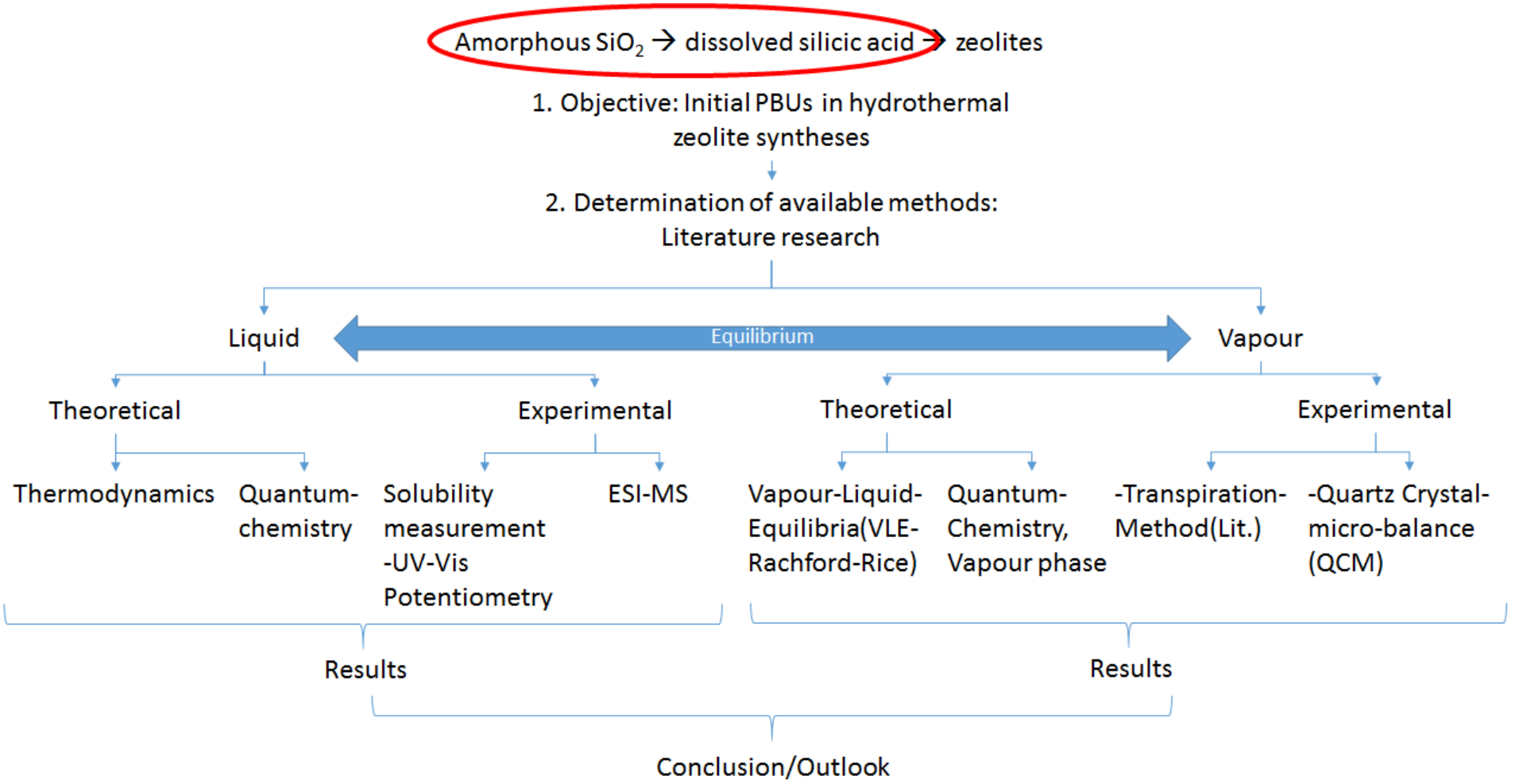

Figure 2-5 – The flow diagram of this whole work [35, 36].

3 Fundamentals of hydrothermal conditions

3.1 Thermodynamics

In this investigation, the conventional method is taken to be that of the thermodynamic method, as reasonable amount of work for silicic acid based on thermodynamics has been done ([37]-Ch.1 p.6-50). In the chemical thermodynamics of silica, the free energy will be considered as much emphasis is put on it in literature. This will be made clear along the course of this work, such as the determination equilibrium constants for silicic acid solubility in the liquid and vapour phase. Furthermore, it is used for the dissociation constant of dissolved silica (synonym: silicic acid) by the application of the Gibbs free energy in electrochemistry through its relation of the Nernst equation.

The change in Gibbs free energy of a pure component is described as follows:

$$dg = sdT + vdp \qquad \text{Equation 3-1}$$

For mixtures in a phase:

$$dg = sdT + vdp + \sum_{i=1}^{N} \mu_i dn_i \qquad \text{Equation 3-2}$$

As hydrothermal syntheses of zeolites are conducted at temperatures greater than the normal boiling point of water, the existence of two phases, namely the liquid and vapour phase is formed. Under the condition that two phases are in thermodynamic equilibrium, the chemical potential in both phases must be equal:

$$\mu_i^V = \mu_i^L = \left(\frac{dg^V}{dn_i}\right)_{T,p,n_j} = \left(\frac{dg^L}{dn_i}\right)_{T,p,n_j} \qquad \text{Equation 3-3}$$

Hence:

$$[\Delta g]^V = v[\Delta p]^V + \sum_{i=1}^{N} \left(\frac{dg^V}{dn_i}\right)_{T,p,n_j} [\Delta n]^V \qquad \text{Equation 3-4}$$

$$[\Delta g]^L = v[\Delta p]^L + \sum_{i=1}^{N} \left(\frac{dg^L}{dn_i}\right)_{T,p,n_j} [\Delta n]^L \qquad \text{Equation 3-5}$$

The phase equilibrium of two co-existing phases will be explained in a section 3.1.3. However, the above equation 3-4 and equation 3-5 provide all information done in this work.

It is known that under the consideration of the van't Hoff equation, the equilibrium constant relates to the Gibbs free energy of the system.

In dissolution (solubility) and dissociation reactions, the van't Hoff equation (equation 3-21) and the Nernst equation (equation 3-26) are respectively used. Furthermore, the reaction equilibria for the phases of concern can be determined by the following reactions:

$$[\Delta g]^V = \sum_{i=1}^{N} \left(\frac{dg^V}{dn_i} \right)_{T,p,n_j} [\Delta n]^V \qquad \text{Equation 3-6}$$

$$[\Delta g]^L = \sum_{i=1}^{N} \left(\frac{dg^L}{dn_i} \right)_{T,p,n_j} [\Delta n]^L \qquad \text{Equation 3-7}$$

Hence, the free energy can be determined experimentally from the composition of species involved in the solution. It is also possible to determine the free energy and enthalpy by theoretical means such as the ab-initio quantum chemical procedures.

3.1.1 Solubility

The solubility of chemical substances is the amount of a pure component (gas, liquid, solid) dissolved in a solvent. It is dependent upon the temperature pH, polarity of the pure component and the solvent. Gases dissolve easily at higher pressures whereas solid compounds dissolve easily at higher temperature in a given solvent. The solubility of a solid in a solvent is investigated throughout this investigation. The chemical potential for the solubility of solid compound in a solvent is given as:

$$\mu_S - \mu_D = \frac{-\Delta g_{sol}}{RT} = \ln x_D \qquad \text{Equation 3-8}$$

$$\frac{d\left(-\Delta g_{sol} / RT \right)}{dT} = \frac{\Delta h_{sol}}{RT^2} \qquad \text{Equation 3-9}$$

Substituting *ln* x_D and integration over all x_D and temperature:

$$\ln x_D = -\frac{\Delta h_{sol}}{R}\left(\frac{1}{T} - \frac{1}{T^o} \right) \qquad \text{Equation 3-10}$$

The negative sign vanishes if T^o is the melting temperature. However, it is difficult to go to melting temperatures of silica as it involves extremely high temperatures and design of

apparatuses will prove to be challenging with respect to time and cost. In order to stay at mild zeolite syntheses conditions, the investigation is started at standard conditions

Furthermore, the dissolved substance changes in form due to its reaction with water to become silicic acid:

$$SiO_2 + 2H_2O \rightleftarrows Si(OH)_4$$ Equation 3-11

Therefore, the reaction equilibria towards dissolved silica or silicic acid have to be taken into account rather than the melting enthalpy of pure amorphous SiO_2.

3.1.2 Reaction equilibria

The chemical equilibria in a solution are related to the rate of conversion of reactant to products and vice versa. The solubility of a solid in a solvent is described by thermodynamics as the solubility (or equilibrium) constant, which is the ratio between activities of products and reactants. In ideal cases the ratio of the respective molar concentrations are taken. The equation 3-2 is valid here as well. However, at constant temperature and pressure:

$$\Delta g_{reaction} = \sum_{i=1}^{N} \left(\frac{dg}{dn_i} \right)_{T,p,n_j} [\Delta n_i]$$ Equation 3-12

$$\Delta g_{reaction} = \sum_{i=1}^{N} (\mu_i)_{T,p,n_j} [\Delta n_i]$$ Equation 3-13

If one considers $\left(\frac{dg}{dn_i} \right) = \mu_i$ and $\Delta n = \nu_i \xi$

$$\Delta g_{reaction} = \sum_{i=1}^{N} (\mu_i)_{T,p,n_j} [\nu_i \xi]$$ Equation 3-14

$$\Delta g_{reaction} = \sum_{i=1}^{N} (\nu_i \mu_i)_{T,p,n_j} [\xi]$$ Equation 3-15

$$dg = \sum_{i=1}^{N} (\nu_i \mu_i)_{T,p,n_j} d[\xi]$$ Equation 3-16

$$\Delta g_{reaction} = \left(\frac{dg}{d[\xi]} \right)_{T,p,n_j} = \sum_{i=1}^{N} (\nu_i \mu_i)_{T,p,n_j}$$ Equation 3-17

Moreover, at equilibrium, $\Delta g_{reaction}$ is zero at equilibrium, negative if exothermic and positive if endothermic. The equilibrium constant is the product of the products and reactants:

$$K_{reaction} = \prod_{i=1}^{N} A_i^{\nu}$$ Equation 3-18

$$\Delta g^{o}_{reaction} = \sum \nu_{products} \Delta g^{o}_{f,products} + \sum -\nu_{reac\,tants} \Delta g^{o}_{f,reac\,tants}$$ Equation 3-19

The natural logarithm of the equilibrium constant is directly related to the free energy, described by the Gibbs-Helmholtz equation:

$$\ln K^{o}_{reaction} = \frac{-\Delta g^{\circ}_{reaction}}{RT}$$ Equation 3-20

$$\frac{d\left(\ln K_{reaction}\right)}{dT} = \frac{\Delta h_{reaction}}{RT^2}$$

If $\Delta h^{o}_{reaction}$ is considered to be constant at the temperature range given, integration of the above equation with consideration of the equilibrium constant at standard condition with integration limits gives:

$$\ln K_{reaction} = -\frac{\Delta g^{\circ}_{reaction}}{RT^{o}} - \frac{\Delta h^{\circ}_{reaction}}{R}\left(\frac{1}{T} - \frac{1}{T^{o}}\right)$$ Equation 3-21

with: $\Delta g^{o}_{reaction} = \sum_{i=1}^{N} \nu_i \Delta g^{o}_{f,i}$ Equation 3-22

and $\Delta h^{o}_{reaction} = \sum_{i=1}^{N} \nu_i \Delta h^{o}_{f,i}$ Equation 3-23

The general equilibrium constant shown in literature is as follows:

$$K_{p,total} = \frac{\left[Si(OH)_4\right]}{\left[SiO_2\right]\left[H_2O\right]^2}$$ Equation 3-24

With the relation $\Delta g = -zF\Delta E$

$$\Delta g = \Delta g^{o} + RT \ln K$$ Equation 3-25

$$E = E^{o} - \frac{RT}{zF} \ln K$$ Equation 3-26

3.1.2.1 Multiple reaction equilibria

The relaxation method is a convenient method to determine the reaction equilibrium of multiple reactions. The mass balance is already taken into account with the description of the equilibrium constant with respect to their molar concentrations and stoichiometry. This method is used in this work for the multiple reaction equilibria of silicic acid species.

In the relaxation method shown in figure 3-1, each reaction is assigned to a virtual reactor, where only the respective reaction assigned to the reactor takes place. All the reactors are then successively coupled with each other for the number of reactions involved. The concentrations of the reactants and products are calculated with a target concentration of one of the products for the respective reaction. The concentrations leaving the first reactor are applied in the calculation of the equilibrium concentrations in the second reactor. This step is repeated for the number of available reactions. The mixture leaving the last reactor is recycled into the first reactor, hence changing its equilibrium concentrations. The simulation is continued until no difference in concentration of all components in all reactors is observed.

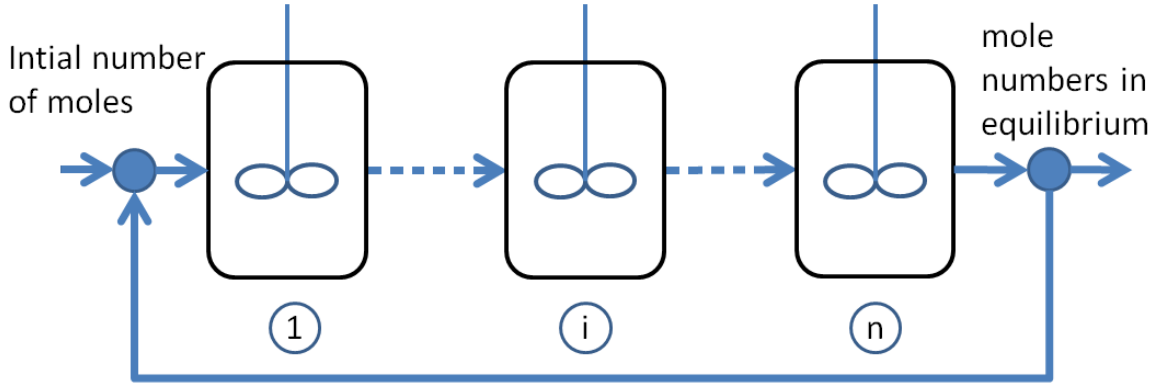

Figure 3-1 – A generalised scheme of the relaxation method is depicted above([38]-p.552).

3.1.3 Phase equilibrium

Phase equilibrium is the state of balance between two phases of a system. It occurs when the transfer of matter or heat energy from one phase to another phase is equal to the rate of transfer of matter or heat energy in the reverse direction. Therefore, it describes the co-existence of two or more phases (e.g. vapour, liquid, solid) in equilibrium. The description of phase equilibria in the next subsection explains the phase equilibrium for a pure component system.

3.1.3.1 Phase equilibria of pure components

For ideal gases, the relation of a pure component is given by the ideal gas law

$$Pv = nRT \qquad \text{Equation 3-27}$$

However, real fluids deviate from the ideal gas behaviour. The residual functions as well as the fugacity and fugacity coefficients have to be taken into account in such a case. The residual function is the difference between the thermodynamic property of a real fluid and the corresponding ideal gas state at the same temperature and pressure. The fugacity is defined as

the capability of a molecule to escape from its current phase to another corresponding phase. The fugacity coefficient is the residual function of the Gibbs free energy. As the system in this work has mainly water to be dealt with below 20 bars, the difference of the fugacity and pressure is assumed to be negligibly small. The pure component system is dependent upon pressure, volume and temperature (see figure 3-2). The temperature dependence of the fugacity coefficient can be described by the Gibbs-Helmholtz equation, which is also the basis equation for the determination of the equilibrium constant in this work.

$$\frac{\partial g/RT}{\partial T} = -\frac{h}{RT^2}$$, where h is the enthalpy Equation 3-28

The phase equilibrium of two difference phases for a pure component requires that the Gibbs free energy in both phases is equal:

$$\Delta g^V = \Delta g^L$$ Equation 3-29

A convenient way to express the phase equilibrium of a pure component is with the equation of state. For real fluids, the cubic equation of state is commonly used such as the van der Waals, Redlich-Kwong, Soave-Redlich-Kwong equations of state. Some virial equations of state are also used such as in the Leiden or Berlin forms. Caloric information such as the heats of vaporisation can be retrieved.

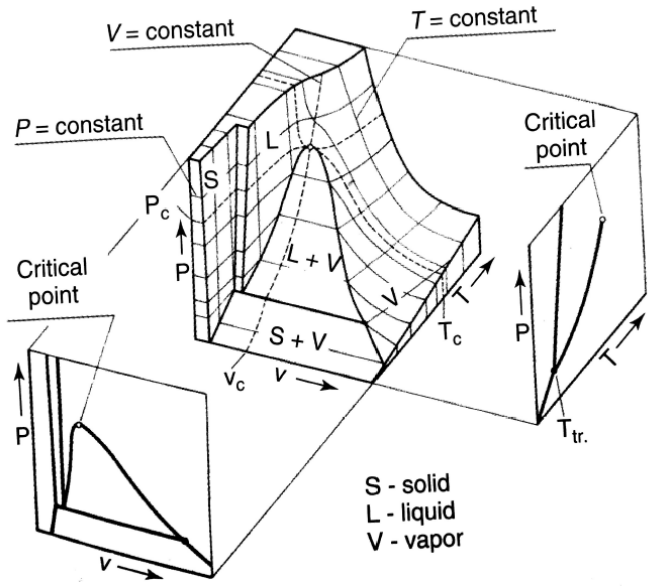

Figure 3-2 – A three dimensional view of the pressure, volume, temperature surface of a pure component ([38]-p.6).

3.1.3.2 Phase equilibria of mixtures

If an arbitrary thermodynamic state variable is taken into account, the respective state variable is a function of other state variables. These are pressure, temperature and volume. Furthermore, unlike for a pure component, it is also a function molar composition of the chemical components in the system (in our case silicic acid and water-2 component system).

$$m = f\left(p, T, x_i\big|_{1<i<N}\right) \qquad \text{Equation 3-30}$$

A simple form of the mixture property of a state variable is simply the sum of the state variable and its molar composition

$$m = \sum_i^N m_i x_i \qquad \text{Equation 3-31}$$

The property change of mixing, Δm comes into play as soon as a mixture exist (Δm = 0 for a pure component).

$$\Delta m = m - \sum_i^N m_i x_i \qquad \text{Equation 3-32}$$

The Gibbs-Duhem equation defines all thermodynamic state variables needed for a mixture as follows:

$$d\left(n_T m\right) = n_T \left(\frac{\partial m}{\partial T}\right)_{\mathrm{p,n_i}} dT + n_T \left(\frac{\partial m}{\partial p}\right)_{\mathrm{p,n_i}} dp + \sum_i^N m_i dn_i \qquad \text{Equation 3-33}$$

If one observes equation 3-6 and 3-7 (see page 15 of this work) carefully, if the Gibbs free energy and the concentration in the respective phase are known, the chemical potential is determined. The chemical potential in both phases must be equal under equilibrium conditions (see figure 3-3). This is defined as the phase equilibria for the mixture.

$$\left(\frac{\partial g}{\partial n_i}\right)_i^L = \mu_i^L = \left(\frac{\partial g}{\partial n_i}\right)_i^V = \mu_i^V \qquad \text{Equation 3-34}$$

Furthermore, excess properties, fugacity and the excess property of the Gibbs energy, termed the activity coefficient for description of real mixtures can be added. Calculation of the phase equilibria can be made by the Rachford-Rice method developed mainly for hydrocarbons in the oil refining industry. However, its application has extended its purpose due to its flexible approach ([39]-p.185-195;p.219-222).

$$\partial g = \left(\mu_i^V - \mu_i^L\right)\partial n_i \qquad \text{Equation 3-35}$$

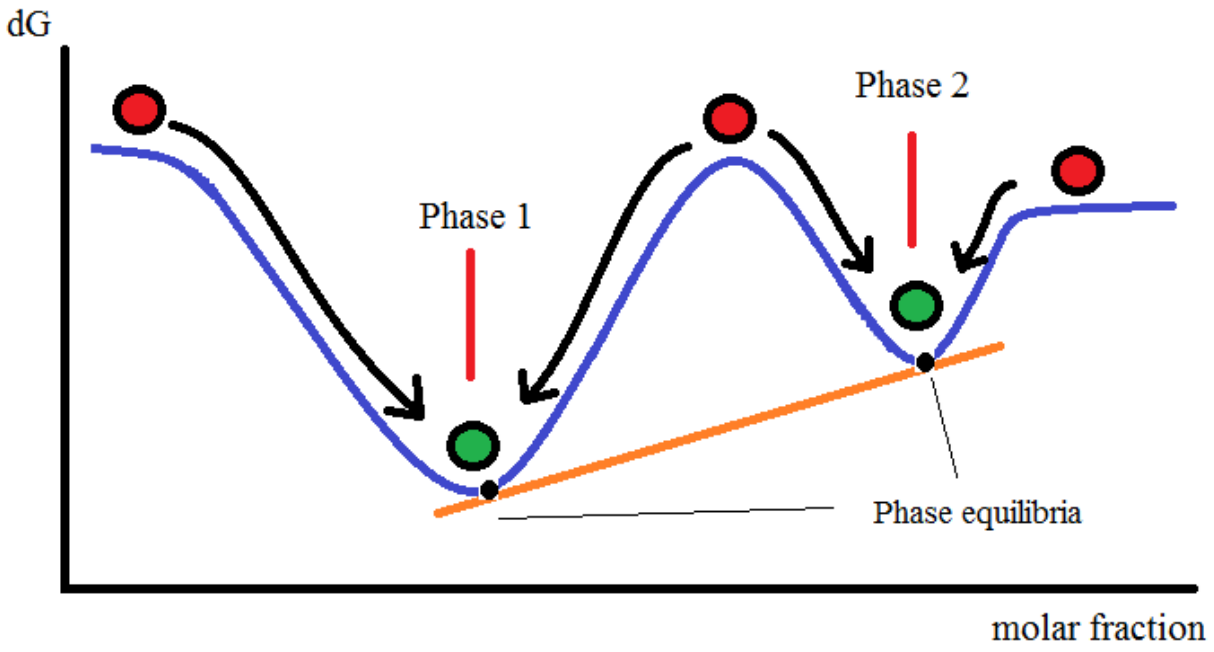

Figure 3-3 – A simplified sketch to the calculation method of the Vapour Liquid Equilibria (VLE) according to Rachford and Rice [40].

3.2 Hydrothermal conversion of silicic acid species

Hydrothermal syntheses occur at high temperatures and pressures. In nature, these natural phenomena occur at above 200°C and its saturation pressure corresponds to the vapour pressure of aqueous solution [7]. In laboratory syntheses of zeolites, it is normally lower than natural conditions (< 200°C) with the assistance of structure directing agents (e.g. tetrapropyl ammonium bromide) or templates and transporting agents, which are known as mineralisers. These substances help to advocate the structure desired, in which the templates give the structure and the mineraliser performs rapid transport of the building blocks and hence the temperature needed does not exceed the conditions exhibited in natural reservoirs. Nevertheless, it is advantageous to choose low temperatures and neutral pH as a starting point. These are to be used, as hydrothermal system parameters are available from early investigations. It is also possible to increase the sensitivity of the custom made apparatuses as the experiments are conducted at higher temperatures and pH. This equilibrium constant relates to the total free energy of system from condensation, cyclisation and the dissociation of all dissolved silica species, in which has been so far simply described as the solubility of monosilicic acid in literature (see equation 3-11) [22]. The equilibrium constant is described in literature as in equation 3-24:

$$K_{p,total} = \frac{\left[Si(OH)_4\right]}{\left[SiO_2\right]\left[H_2O\right]^2}$$

In this work, theoretical equilibrium constants for all species are given by energies of formation of the respective species involved in polymerisation, cyclisation and dissociation reactions in section 4.1.1 and 4.1.2. The experimental K_p values are derived from UV-Vis and ESI-MS experiments. Linear silicic acid species are simply straight and not branched. The reactions are categorised as condensation reaction type 1 (K1) A cyclic species is defined if all Si atoms are connected to each other and their reactions are denoted as C1. These are both simple-cyclic and fused-cyclic species. Upon absence of one Si-O-bond to another Si-atom, the species is considered branched-cyclic and categorised under mixed condensation reactions (K2), as shown in figure 3-4. The dissociation reactions of K1 and K2 are denoted as D1 and the dissociation reaction of cyclic species are given the abbreviation D2.

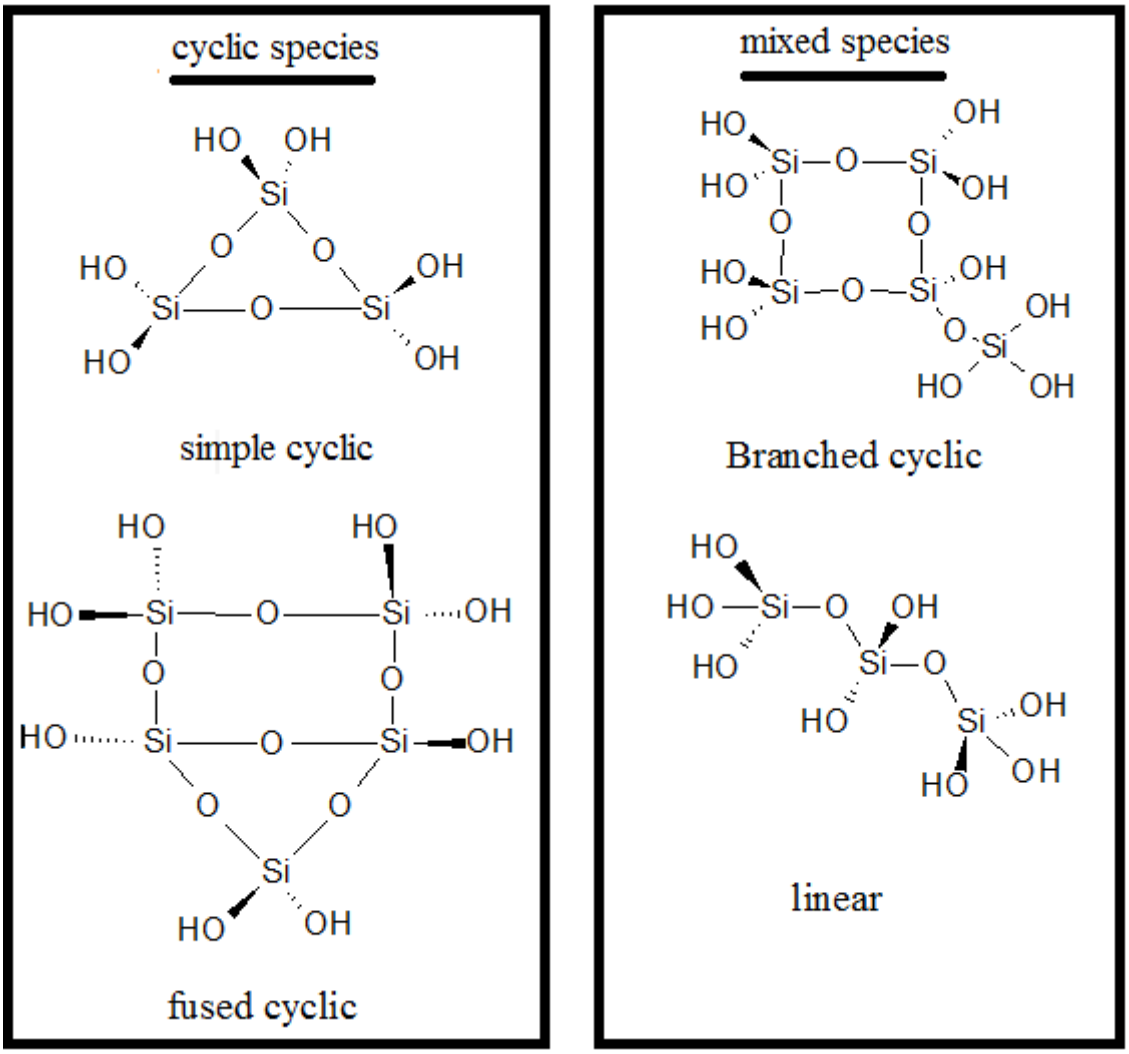

Figure 3-4 – The figure depicts the difference between cyclic (simple-cyclic for Si ≤ 4and fused-cyclic Si > 4) and mixed (linear for Si ≤ 4 and branched-cyclic for Si > 4) species.

In literature, many reaction paths of dissolved silica have been reported, both in terms of experimental studies [22, 41-57] as well as theoretical studies [58-69]. The main reactions are:

1. Mixed (linear) condensation (K1)-linear species with number of Si-atoms ≤ 4
2. Mixed condensation (K2)-branched-cyclic species with number of Si-atoms > 4
3. Cyclisation (C1) – simple-cyclic with number of Si-atoms ≤ 4 and fused-cyclic species with number of Si-atoms > 4
4. Mixed dissociation (D1)
5. Cyclic dissociation (D2)

The reactions are shown in Figure 3-6 (see page 28 of this work). Furthermore, the type of reactions (K1, K2, C1, D1, and D2) is shown for each silicic acid species in Table 3-1. The respective abbreviations are also written and used throughout this work.

Table 3-1 – The abbreviation of silicic acid reactions considered in this work.

Condensation (K1 and K2)	Dissociation (D1)
-	$Si(OH)_4 \rightleftarrows H_3SiO_4^- + H^+$ (D1-Si1)
$Si(OH)_4 + Si(OH)_4 \rightleftarrows Si_2(OH)_6O + H_2O$ (K1-Si2)	$Si_2(OH)_6O \rightleftarrows Si_2(OH)_5O_2^- + H^+$ (D1-Si2)
$Si(OH)_4 + Si_2(OH)_6O \rightleftarrows Si_3(OH)_8O_2 + H_2O$ (K1-Si3)	$Si_3(OH)_8O_2 \rightleftarrows Si_3(OH)_7O_3^- + H^+$ (D1-Si3)
$Si(OH)_4 + Si_3(OH)_8O_2 \rightleftarrows Si_4(OH)_{10}O_3 + H_2O$ (K1-Si4)	$Si_4(OH)_{10}O_3 \rightleftarrows Si_4(OH)_9O_4^- + H^+$ (D1-Si4)
$Si(OH)_4 + Si_4(OH)_{10}O_3 \rightleftarrows Si_5(OH)_{10}O_5 + 2H_2O$ (K2-Si5)	$Si_5(OH)_{10}O_5 \rightleftarrows Si_5(OH)_9O_6^- + H^+$ (D1-Si5)
$Si(OH)_4 + Si_5(OH)_{10}O_5 \rightleftarrows Si_6(OH)_{12}O_6 + H_2O$ (K2-Si6)	$Si_6(OH)_{12}O_6 \rightleftarrows Si_6(OH)_{11}O_7^- + H^+$ (D1-Si6)
$Si(OH)_4 + Si_6(OH)_{12}O_6 \rightleftarrows Si_7(OH)_{14}O_7 + H_2O$ (K2-Si7)	$Si_7(OH)_{14}O_7 \rightleftarrows Si_7(OH)_{13}O_8^- + H^+$ (D1-Si7)
$Si(OH)_4 + Si_7(OH)_{14}O_7 \rightleftarrows Si_8(OH)_{16}O_8 + H_2O$ (K2-Si8)	$Si_8(OH)_{16}O_8 \rightleftarrows Si_8(OH)_{15}O_9^- + H^+$ (D1-Si8)

Cyclisation (C1)	Cyclic dissociation (D2)
-	-
-	-
$Si_3(OH)_8O_2 \rightleftarrows Si_3(OH)_6O_3 + H_2O$ (C1-$_{Si3cyc}$)	$Si_3(OH)_6O_3 \rightleftarrows Si_3(OH)_5O_4^- + H^+$ (D2-$_{Si3cyc}$)
$Si_4(OH)_{10}O_3 \rightleftarrows Si_4(OH)_8O_4 + H_2O$ (C1-$_{Si4cyc}$)	$Si_4(OH)_8O_4 \rightleftarrows Si_4(OH)_7O_5^- + H^+$ (D2-$_{Si4cyc}$)
$Si_5(OH)_{10}O_5 \rightleftarrows Si_5(OH)_8O_6 + H_2O$ (C1-$_{Si5cyc}$)	$Si_5(OH)_8O_6 \rightleftarrows Si_5(OH)_7O_7^- + H^+$ (D2-$_{Si5cyc}$)
$Si_6(OH)_{12}O_6 \rightleftarrows Si_6(OH)_8O_8 + 2H_2O$ (C1-$_{Si6cyc}$)	$Si_6(OH)_8O_8 \rightleftarrows Si_6(OH)_7O_9^- + H^+$ (D2-$_{Si6cyc}$)
$Si_7(OH)_{14}O_7 \rightleftarrows Si_7(OH)_{10}O_9 + 2H_2O$ (C1-$_{Si7cyc}$)	$Si_7(OH)_{10}O_9 \rightleftarrows Si_7(OH)_9O_{10}^- + H^+$ (D2-$_{Si7cyc}$)
$Si_8(OH)_{16}O_8 \rightleftarrows Si_8(OH)_8O_{12} + 4H_2O$ (C1-$_{Si8cyc}$)	$Si_8(OH)_8O_{12} \rightleftarrows Si_8(OH)_7O_{13}^- + H^+$ (D2-$_{Si8cyc}$)

Desorption of silanol group from the surface of the amorphous silica should be considered in this case as well. The dissolution process starts with the adsorption of OH-groups on the surface of amorphous silica and the desorption of silanol groups via the cleavage of the silica from the arbitrarily structured lattice of amorphous silica. This creates monosilicic acid first in the liquid phase. Some adsorption of silanol groups on the surface of amorphous silica has been reported by Zhuravlev [70, 71].Quantum chemical simulations on OH^-group attack on quartz surfaces was done by Xiao [62] and plane critstobalite by Pelmenschikov [72]. However, reports on OH^- attack on amorphous silica surfaces are scarce. Ideally, the energy of desorption should be added to the equilibrium constant, but the results of this work only became worse after its inclusion. Therefore, the actual relation to the contribution of the desorption energy is not clear in this work. However, it should be mentioned that it contributes to the equilibrium constant for the dissolution of silica as observed from water sorption results done in this work (see Appendix section 7.3). Only the reactions in table 3-1 (see page 23 and 24 of this work) are considered in this work.

Firstly, the condensation reaction of mixed species is considered and these mixed species considered in this work are of linear and branched-cyclic nature. The systems in this work

contain mainly silicic acid and water. According to Kolbe ([73]-p.57-59), the existence of linear silicic acid species only prevails under the addition of organic templates of the like in the solution. This is especially valid for longer linear species than tetrasilicic acid. The condensation reaction scheme is important for the supply of reactants for further reactions towards scaffolding materials needed in the zeolite syntheses solution. Furthermore, the cyclisation scheme is most certainly important for the supply of scaffolding material which is desired for the respective zeolite syntheses (controlled by temperature and pH and structure directing agent-if any) after the condensation reaction. These species are transition building blocks existing between PBUs to SBUs in the zeolite syntheses [60, 61, 69]. The last reaction scheme is the dissociation reaction of the mixed (linear and branched-cyclic-see page 22 of this work) and cyclic (simple-and fused-cyclic-see page 22 of this work) silicic acid species. As OH-groups in a silanol bond are plenty in the silicic acid species considered, they are likely to deprotonate due to the high rate of hydrogen bonding at a magnitude at least comparable to that of the dissociation of water, deviating to a few orders of magnitude [41-44]. Since trimolecular reaction according to literature [74, 75], are highly unlikely, only dimolecular reactions are considered. Similarly, higher molecular reactions are excluded.

This work attempts to couple all reaction paths mentioned in Figure 3-6 (see page 28 of this work). This method is used for best possible description of the chemical reactions and interaction existing in the solution supported by data provided in literature ([13-16, 18, 19, 37, 41-44, 46, 47, 54, 58-61, 65-67, 69, 73, 74, 76-81]; 68-p.57.59). This provides one possible equilibrium description of a solution with dissolved silica in equilibrium. It is advised to take more feasible reaction equilibrium models and perform a Monte Carlo simulation [82]. This gives a distribution of the possible reaction pathways and the most likely to occur under hydrothermal conditions. However, this is not done in this work due to the many combinations of the reaction pathways.

The method used for each reaction path is termed the relaxation method (see section 3.1.2.1). It is a common method used in the field of chemical engineering to simulate complex reactions provided that the free energy and enthalpy of the system or the equilibrium constant for the system in consideration is known. The reactions are coupled with each other by entering another reaction unit with the successfully achieved equilibrium state of the previous reaction. The relaxation method in this work is explained best with Figure 3-5 (see page 26):

Furthermore, the dissociation constants are calculated but cannot be introduced with its actual values in the equilibrium model of figure 3-5 (see page 26). The dissociation constants based on quantum chemical calculations were too low to be considered in the model. It is known that low but substantial amounts of the silicic acid species would be dissociated and a deficit in the recycling event of the silicic acid species would occur in the course of the iteration in the relaxation model. Therefore, the dissociation constants were assigned appropriately to accommodate to the model based on significant literature data.

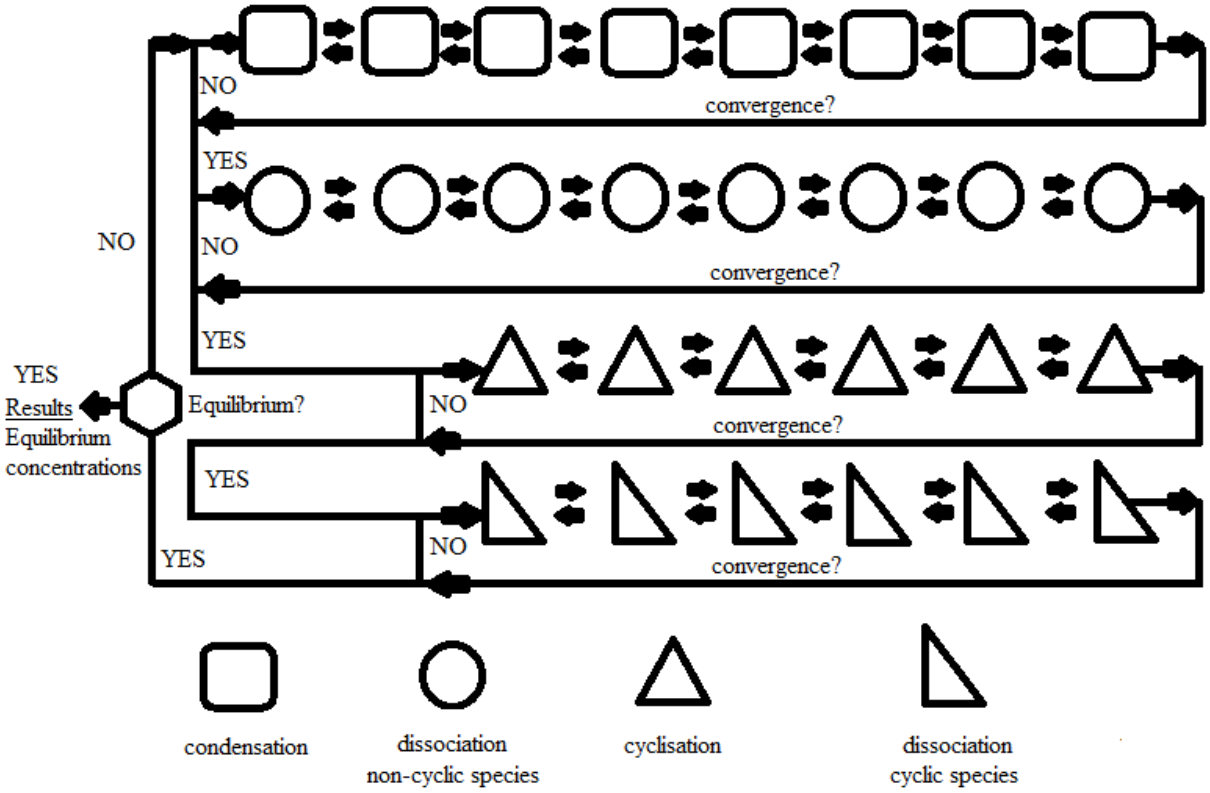

Figure 3-5 – The schematic flow of the equilibrium model consisting all reaction pathways and coupled with each other is clarified above.

For each reaction mechanism employed, the equilibrium constant was assigned an initial value. The fitted values from ESI-MS (see section 4.2.1.1.3.2, figure 4-15 and 4-16) were taken as a reference for the initial value and modified to achieve a more consistent value to the reaction scheme in Figure 3-5. This modification also corresponds to explanations from previous works of Gunnarsón, Elmer and Norberg, Hill and Sauer, Sefcík, Busey and Mesmer, Ingri and Sjöberg, Garofalini, Kagan, Montero-Cabrera, Xiao and Lasaga [20-22, 41-44, 48, 58-63, 65, 77, 78]. All equilibrium constants are related to the concentration ratio of products and reactants (see equation 3-18). The first derivatives of the equation 3-18 were determined with respect to the silicic acid product of the respective reaction. Hence, the equilibrium concentration of the silicic acid species of concern (denoted with *i*) is iteratively

calculated with the Newton procedure. Concentrations of all linear species ($linear_i$), all branched-cyclic species ($branched_i$) and all cyclic ($cyclic_i$) species are denoted accordingly

$$TF_{K1-Si(i)} = K_{mixed,K1-Si(i),\exp} - \frac{[linear,i][H_2O]^{\nu_{H2O}}}{[linear,i-1][Si(OH)_4]}$$

condensation (K1)

Equation 3-36

$$TF_{K2-Si(i)} = K_{mixed,K2-Si(i),\exp} - \frac{[branched,i][H_2O]^{\nu_{H2O}}}{[branched,i-1][Si(OH)_4]}$$

condensation (K2)

Equation 3-37

$$TF_{C1-Si(i)cyc} = K_{cyc,C1-Si(i)cyc,\exp} - \frac{[cyclic,i][H_2O]^{\nu_{H2O}}}{[branched,i]}$$

cyclisation (C1)

Equation 3-38

$$TF_{D1-Si(i)} = K_{DISS,D1-Si(i),\exp} - \frac{[mixed^-,i][H^+]}{[mixed,i]}$$

mixed dissociation (D1)

Equation 3-39

$$TF_{D2-Si(i)cyc} = K_{DISS,D2-Si(i)cyc,\exp} - \frac{[cyclic^-,i][H^+]}{[cyclic,i]}$$

cyclic dissociation (D2)

Equation 3-40

$$[silicic\ acid]_{i,iter+1} = [silicic\ acid]_{i,iter} - \frac{TF}{\partial TF / \partial [silicic\ acid]_{i,iter}}$$

Equation 3-41

$$TF_{total} = \sum_{i=1}^{N} \left(n_{silicic\ acid,i,iter+1} - n_{silicic\ acid,i,iter} \right) < eps, \text{eps} = 1\text{x}10^{-4}$$

Equation 3-42

It must be recognised that once an equilibrium concentration is determined, it will reduce the reactants of the previous reaction. Therefore, the equilibrium concentration calculated in the previous reaction has changed and the equilibrium constant does not correspond to the one assigned to it. In order to achieve a minimal amount of change in the equilibrium constant, namely the convergence, the equilibrium concentrations calculated in one cycle is recycled back to the start of the reaction scheme. New equilibrium concentrations according to the equilibrium constants assigned to each respective reaction in the reaction scheme will be calculated again until convergence is achieved.

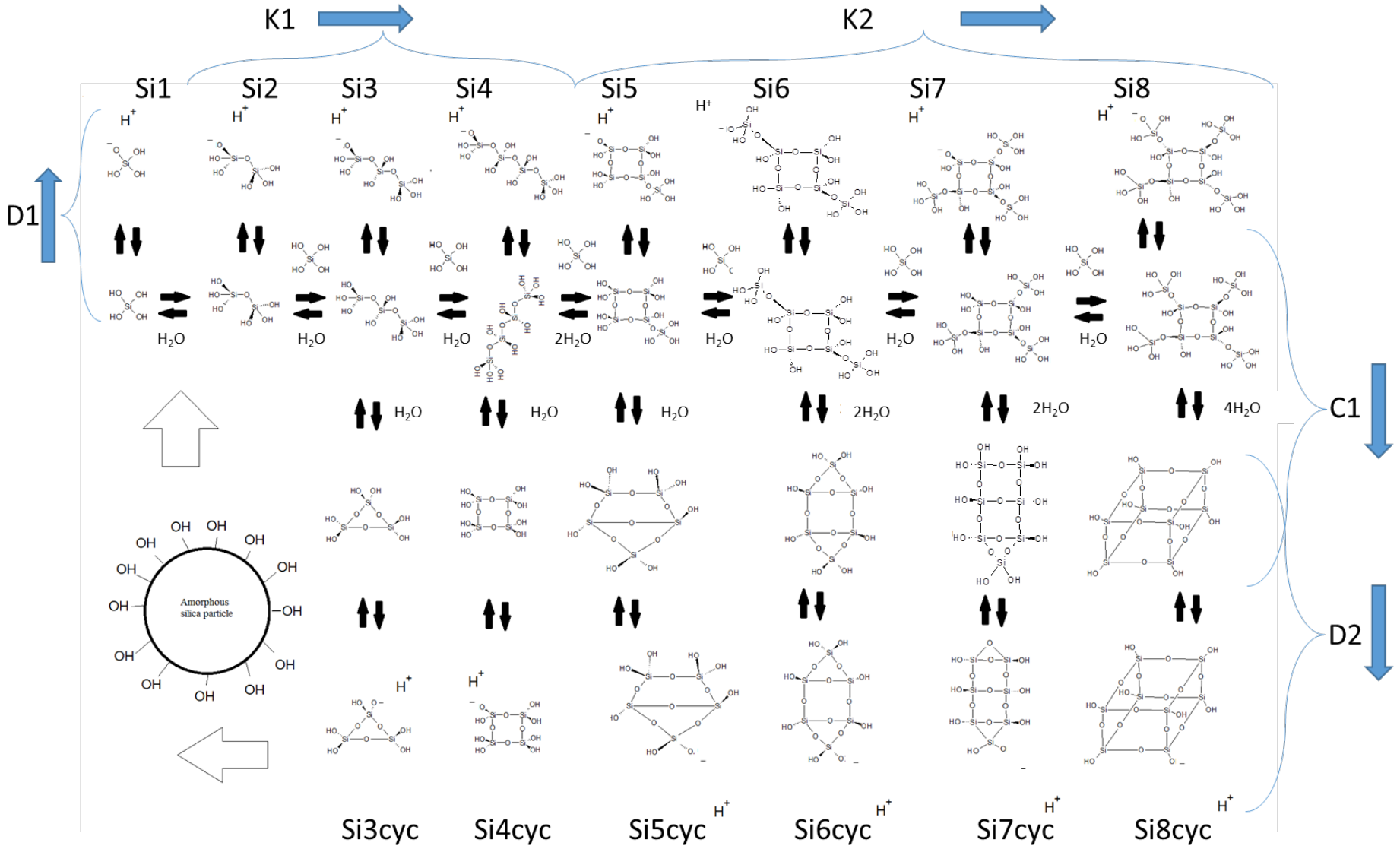

Figure 3-6 – The probable reaction pathways of respective silicic acid species chosen for this work derived according to data from literature is shown above.

3.3 Quantum chemistry

The quantum chemical calculations are based on the electronic Schrödinger equation. This work applies the non-relativistic and time independent version of the Schrödinger equation:

$$\hat{H}_{el} \left| \Phi \right\rangle = \varepsilon \Phi \rangle$$ Equation 3-43

A variety of methods are available to approximate solutions to Schrödingers equation [83]. These are the Hartree Fock solutions and their extensions, as well as Density Functional Theories.

3.3.1 Quantum chemical methods

As mentioned above briefly in section 3.3, the Hartree-Fock extension and the density functional theories are available for calculation purposes. In this work, it has been decided to perform calculations with the B3LYP method, being a method derived from density functional theory, and appropriate for thermochemistry [84].

3.3.2 Solvent effects

The free energies and enthalpies of formation and reaction of silicic acid species are partly calculated with the consideration of solvent effects, as water is abundant in our considered system. The method used to simulate solvent effects is one of the pioneering methods in quantum chemistry dealing with solvent effects. This is the so-called Dielectric Polarised Continuum Method (DPCM or PCM). The PCM defines a dielectric field which simulates the existence of the solvent around the vicinity of the molecule of interest and the surface of the molecular system is assigned an apparent surface charge (ASC). The reaction potential between the dielectric and the ASC is given by a distribution function. The intensity of the reaction potential is given by the Poisson equation [85]. The PCM defines a local contribution of the solvent around the continuum of the molecule. Figure 3-7 depicts the explanations in this section.

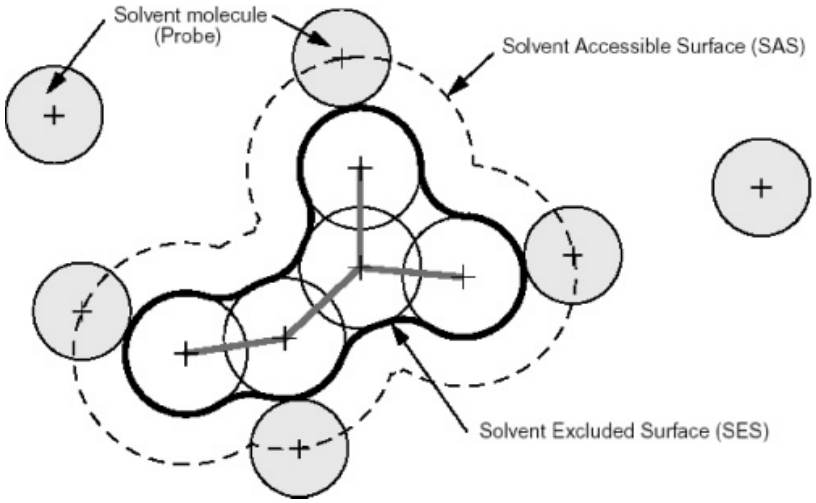

Figure 3-7 – Figure taken from Tomasi and Menucci for the depiction of the Apparent Surface Charge (ASC) [85].

3.4 Evaluation of possible experimental methods for the characterisation of silicic acid species

3.4.1 Determination of concentration via UV-Vis spectroscopy

The concentration of dissolved silica is measured photospectrometrically (UV-Vis) by addition of ammonium heptamolybdate treated with diluted ammonium hydroxide and diluted sulphuric acid to the sample solution. The method used is the molybdenum yellow method [86-88] recommended by Iler ([37]-p.97). The molybdate[VI] anion method traps one Si-atom cleaved from its hydroxyl bonds in the tetrahedrally coordinated space of 12 MoO^{-}_{6} octahedra. The measurement is done in the UV-Vis range obeying the Beer Lambert law.

$$\overline{E} = \ln\left(\frac{I}{I_{base}}\right) = \overline{\varepsilon}\left[Si\,Mo_{12}O_{40}^{4-}\right]d \qquad \text{Equation 3-44}$$

3.4.2 Determination of silicic acid species via ESI-MS spectroscopy

The types of species in both phases (especially the liquid phase) are determined from Electron Spray Ionisation Mass Spectrometry (ESI-MS). It is important to determine the existing species to find the free energy and enthalpy of a given silicic acid molecule from the relative intensities of the detecting mass spectrometer. It is also useful to provide information on the molecular formula for energy calculations in quantum chemical procedures.

The ESI-MS measurement is a measurement technique used to preserve the solution as present in equilibrium with no cleavage of molecules as proven by Pelster [15] by applying a fine spray technique with the nozzle known as the Taylor cone. A high voltage is applied to

attract negatively charged or positively charged ions in the solution at the user's desire. The separation of the droplets into smaller ones reach a limit, as the surface tension of the solution holding the molecules together is surpassed by the Coulombic effect of the charged molecules. The molecules hence deflect according to the magnitude of the voltage applied and their respective masses. This phenomenon is described by the Rayleigh discharge relation:

$$q_{Rayleigh} = 8\pi\left(\varepsilon_0 \gamma r_{drop}^3\right)^{1/2} \qquad \text{Equation 3-45}$$

The reduction of the droplets size by separation is however described by two models. The Charged Residue Model (CRM) states that the droplet separates into smaller droplets until the one molecule of the analyte exist. The last solvent molecule evaporated from the droplet leaves the ionic charged analyte for its bombardment on the detector or photomultiplier. Another theory of the ion evaporation model (IEM) states that the droplets evaporate to a certain critical radius, at which the ionic compound is pulled out by the voltage applied by the two poles in the measuring chamber. According to these two models, no fragmentation could occur due to the fine separation technique of the ions from the droplet. Only an excess voltage can induce the fragmentation.

The counts of molecules bombarding the detector is then measured in real-time with respect to the time period of the experiment and added together over the whole time period measured.

As the silicic acid species are negatively charged in a dissociated state, the negative measurement side is considered in this work. Measurements of this work from 25°C to 170°C and pH value of 7 to 13 identified the species in Table 3-2 and many others.

It is well known in literature that even if the existence of monosilicic acid dominates in the liquid phase, there are higher order polymeric silicic acid species, which exists in the solution. Many past literatures have mentioned this and even tried to prove it with the inventive technologies of that time. Real breakthrough was achieved when Kinrade and especially Knight [16-19, 89-91] as well as Pelster and Schüth [13, 15, 76] elucidated the structure with the assistance of NMR and ESI-MS methods respectively. Knight however elucidated the structure with a highly enriched isotope solution of dissolved silica (~ 99.35%) [18, 19]. Hence, it is not the optimal method for the purpose of this work to change the concentration at equilibrium. The method of ESI-MS however suits this work since the method maintains the structural integrity of the silicic acid species (no or little fragments involved). The method has the ability to measure at lower concentrations as well, as is the case in this work (in the range of ppm). Therefore, higher concentration solutions are not needed as for the NMR method.

Table 3-2 – The mixed (linear and branched-cyclic) and cyclic (simple and fused cyclic) silicic acid species considered in this work

Mixed (see page 22)	Cyclic (see page 22)
Monosilicic acid	-
Disilicic acid (linear)	-
Trisilicic acid (linear)	Cyclotrisilicic acid (simple-cyclic)
Tetrasilicic acid (linear)	Cyclotetrasilicic acid (simple-cyclic)
Pentasilicic acid (branched-cyclic)	Cyclopentasilicic acid (fused-cyclic)
Hexasilicic acid (branched-cyclic)	Cyclohexasilicic acid (fused-cyclic)
Heptasilcic acid (branched-cyclic)	Cycloheptasilcic acid (fused-cyclic)
Octasilicic acid (branched-cyclic)	Octahydroxyoctasilsequioxane (fused-cyclic)

The silicic acid species, which are important for the zeolite syntheses (see above table 3-2) are determined with ESI-MS. The enthalpy and free energy calculation of these species at an optimal state of energy is conducted with quantum chemical methods and compared with the equilibrium constant found from experiments done in this work.

3.4.3 Determination of the dissociation constant of total silicic acid species by means of a electrochemical cell - potentiometry

The dissociation constants are measured by a high temperature flow-through electrochemical cell. It is possible to observe the dissociation of all silicic acid species with the dissociation constant by conducting experiments in a electrochemical cell and measuring the potential of the cell containing two half-cells, one being filled with a reference solution and another with a solution with dissolved silica, as done similarly by Busey and Mesmer [42]. The concentration of all dissociated silicic acid species is determined with the Nernst equation (equation 3-26). The Nernst equation is related to the free energy of the half-cells being reduced and oxidised:

$$\Delta E = -\frac{RT}{zF}\ln Q_{DISS} = -\frac{RT}{zF}\ln\frac{\left[H^+\right]^2}{\left[H_2\right]}$$ Equation 3-46

$$Q_{DISS,H_2} = \frac{\left[H^+\right]^2}{\left[H_2\right]}$$ Equation 3-47

Potentiometric studies of the deprotonation or dissociation of silicic acid in an electrochemical cell has been described by Busey et al. [42], Mesmer [92-94] and Becker et al. [79]. The potentiometric cell designed for this work is based on their work. The cell is designed with circulating flows of the reference and sample solution in the respective half-cells.

For this, two separate reactors (one for the reference **[WS]** and one for the sample solution **[SS])** serve as reservoirs of the respective solutions. The solutions are circulated with a micro gear pump for each half-cell (anode and cathode). The flow-through type electrochemical cell with consideration to explanations of Lvov is designed to ensure enhanced mixing effects of the solution and the reduction of the Nernst layer ([95, 96];91-p.126).

This increases the probability of hydrogen dissociation in continuous fresh circulating solution. This hence increases the probability of silicic acid and water reacting with dissociated hydrogen. The extent of water dissociation is the same in both half-cells prior to the addition of amorphous silica, which is slowly dissolved through a filter. However, a calibration measurement must be made to remove all uncertainties. After adding amorphous silica, the voltage difference is a measure of the silicic acid dissociation upon the relation to the Nernst equation (equation 3-26).

It is also designed for the purpose of in-situ observation of the zeolite syntheses. This was done by Yang et al. [80] by periodic dosage of the syntheses solution in a separate reactor. However, the periodic dosage would mean that the concentration of the precursors in the half-cell changes. Yang also reported a phenomenon of crystallisation at different template concentrations and pH at 95°C [80]. This may also describe the evolution of the vapour phase at the given saturation temperature and autogenous vapour pressure.

They compensated the concentration change by controlling the pH of the solution (by addition of NaOH or HCl). It is decided in this work that a flow-through cell would prevent the artificial control of the solution by addition of new substances and keep the integrity of the syntheses solution. Hence the custom-made flow-through cell is designed.

The following reactions are taken into account

$$H_2 \rightleftarrows 2H^+ + 2e^- \qquad \text{R1}$$

This facilitates the following reactions

$$H^+ + OH^- \rightleftarrows H_2O. \qquad \text{R2}$$

$$H^+ + H_3SiO_4^- \rightleftarrows H_4SiO_4 \qquad \text{R3}$$

R1 and R2 occur in both half-cells. Dissociation constants of water and silicic acid are low but measureable compared to the dissociation of hydrogen on the Pt-wires. Hence, it can be safely assumed that the difference of the dissociation of hydrogen on the Pt-wire is dictated by R2 and R3 (if R3 is present in sample solution). Hence calibration measurements are conducted to determine the reference electrochemical potential (E_{REF}) at given reaction conditions in the cell at temperatures of ϑ=25°C to 170°C and pH=7, 12, 13. The potential gives the reaction quotient, $\ln Q_{DISS}$. At equilibrium, the reaction quotients are the equilibrium constant, $\ln K_{DISS}$.

The pH calibration measurements were done by increasing the pH in only one half-cell, as this were the cases for the measurements as well. This calibration corresponds to the dissociation of ΔR2 prior to addition of amorphous silica to the sample solution [SS]. The difference in voltage should correspond to the shift in the reaction due to the additional reaction of R3 in one of the half-cells in the presence of dissociated silicic acid.

It is assumed that R3 is not affected by R2 due to the higher dissociation constant of R3 [42]. Hence, the difference in the consumption of hydrogen is related to the difference of the calibration and sample measurement caused by the dissociation of silicic acid. The dissociation reaction of R1 concerning the hydrogen dissociation is directly related to the dissociation of silicic acid.

E° for hydrogen dissociation (R1) is 0.00V by definition [97]. The half-cell potential is:

$$E_{HC,REF} = E^{\circ}_{HC,REF} + \frac{RT}{zF}\ln\left(\frac{\left[H^{+}\right]^{2}}{\left[H_{2}\right]}\right) \qquad \text{Equation 3-48}$$

The total cell potential is:

$$\Delta E_{C,REF} = \left[\left(E^{\circ}_{HC,1} - E^{\circ}_{HC,2}\right) + \frac{RT}{zF}\left(\ln\left(\frac{\left[H^{+}\right]^{2}}{H_{2}}\right)_{HC,1} - \ln\left(\frac{\left[H^{+}\right]^{2}}{H_{2}}\right)_{HC,2}\right)\right]_{C} \qquad \text{Equation 3-49}$$

$E^{\circ}_{HC,1}$ and $E^{\circ}_{HC,2}$ are defined as 0.00V by definition and the partial pressure of H_2 is given as unity [97]. If the reactions taking place are equal at both half-cells, the standard potential cancels independent of the respective type of reaction. The silicic acid side is taken the cathode (HC, 1). If no silica is present, then $\Delta E_{C,REF} = 0.00V$

$$\Delta E_{C,REF} = \left[\frac{RT}{zF}\ln\left(\frac{\left[H^{+}\right]^{2}_{HC,1}}{\left[H^{+}\right]^{2}_{HC,2}}\right)\right] \qquad \text{Equation 3-50}$$

$$\left[\Delta H^{+}\right] = \frac{\left[H^{+}\right]^{2}_{HC,1}}{\left[H^{+}\right]^{2}_{HC,2}} \qquad \text{Equation 3-51}$$

Under the presence of silica in half-cell 1:

$$Q_{DISS,H_2O} = \frac{\left(\left[H^{+}\right]_{HC,1,Si(OH)_4} - 1\right)\left[OH^{-}\right]}{\left[H_2O\right]} \qquad \text{Equation 3-52}$$

$$\Delta pH = -\log\left(\Delta H^{+}\right) \qquad \text{Equation 3-53}$$

R2 occurs in both half-cells and therefore there should be no voltage difference observed. If the R3 reaction occurs in one of the half-cells, the voltage difference is directly related to the consumption of protons from R1 by R3.

$$\Delta E_{C,SAM} = \left[\frac{RT}{zF}\ln\left(\left[\Delta H^{+}\right]^{2}_{C,SAM}\right)\right]_{C} \qquad \text{Equation 3-54}$$

$$\Delta E_{C,Si(OH)_4} = \left[\frac{RT}{zF} \ln \left(\frac{\left[H^+\right]^2_{HC,1,Si(OH)_4}}{\left[H^+\right]^2_{HC,2}} \right) \right] \qquad \text{Equation 3-55}$$

As silicic acid is a weak acid, the following relation applies:

$$\left[H^+\right]_{HC,1,Si(OH)_4} - 1 = \left[H_3SiO_4^-\right] \qquad \text{Equation 3-56}$$

The relation above is related to concentrations of non-dissociated silicic acid ($Si(OH)_4$), which ranges from 10^{-3} to 10^{-1} at different temperatures and pH values. These values are retrieved from UV-Vis measurements.

$$Q_{DISS,Si(OH)_4} = \frac{\left(\left[H^+\right]_{HC,1,Si(OH)_4} - 1\right)\left[H_3SiO_4^-\right]_{HC,1}}{\left[Si(OH)_4\right]_{HC,1}} \qquad \text{Equation 3-57}$$

This study takes the general silicic acid species into account first [42] for simplicity whereas further segregation of the species are possible with the inclusion of quantum chemical [58-61, 69] and state of the art experimental studies, such as ESI-MS.

3.4.3.1 The cell potential in the presence of stainless steel - corrosive conditions

It is known that silica inhibits corrosion at hydrothermal conditions, provided that the silica deposition is uniform. It also has to cover the stainless steel layer completely. If some inhomogeneity occurs on the stainless steel surface and the stainless steel is exposed, corrosion is facilitated in the form of localised corrosion ([98, 99]- 99-p.171).

At corrosive conditions, the proton concentration is related to the pH of the solution. This is due to the fact that the corrosion is the interfacial phenomena of stainless steel and has no relation to the proton concentration at the Pt-wire. The concentration of protons at HC,1 and HC,2 at their respective Pt-wire is equal. Hence, no difference between Pt-wire is detected. Only the corrosion phenomenon is detected through the Pt-wire. The different hydrogen

concentration available for the corrosion process on stainless steel is responsible for the voltage. A schematic description of the corrosion process is given in figure 3-8.

The anodic and cathodic half-cells remain as conventional oxidising and reducing terminals respectively. Furthermore, qualitative assumptions are made to proceed with the simulation of corrosion reactions. The concentration of hydroxide ions is determined by taking the dissociation constant of water into account. The subscript HC is dropped and only the integers 1 and 2 are used to denote the respective half-cells. The index 1/2 is the ratio of an arbitrary component concentration between half-cell 1 and 2.

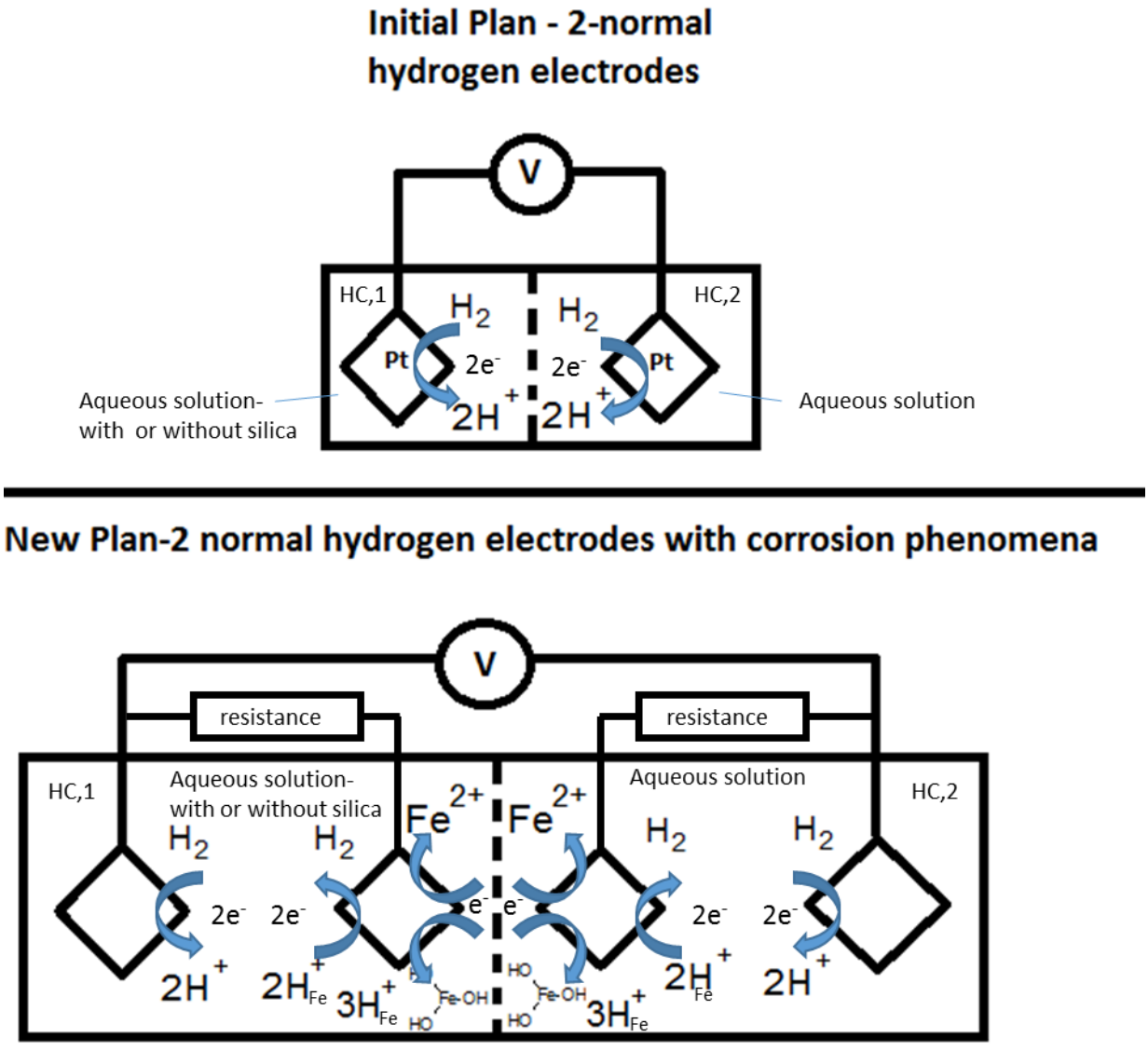

Figure 3-8 – A simplified scheme of the initial plan to measure silicic acid dissociation and the eventual plan of measuring corrosion in the presence of dissolved silica.

Upon injection of H_2 to achieve saturation in the cell, the pH at the interface is high enough to propagate corrosion. $[H^+]_{Fe}$ corresponds to the proton concentration on the stainless steel surface. The following reactions from the Pourbaix Diagram of iron ([98, 100-102]; 97-p.288 and 98-p.177) are considered (appendix 7.2.2 for Pourbaix Diagram of iron). After the determination of the total cell potential as determined for the normal hydrogen electrochemical cell, the following terms are found:

$$H_2 \rightleftarrows 2H^+ + 2e^- \qquad \text{(R1)}$$

$$E_{H_2} = -\frac{RT}{zF}\ln\frac{\left[H_2\right]_{Fe,1/2}}{\left[H^+\right]^2_{Fe,1/2}} \qquad \text{Equation 3-58}$$

$$Q_{H^+} = \frac{\left[H_2\right]_{Fe,1/2}}{\left[H^+\right]^2_{Fe,1/2}} \qquad \text{Equation 3-59}$$

$$Fe_{(s)} \rightleftarrows Fe^{2+} + 2e^- \qquad \text{(RC2)}$$

$$E_{Fe^{2+}} = -\frac{RT}{zF}\ln\frac{\left[Fe^{2+}\right]_{1/2}}{\left[Fe_{(s)}\right]_{1/2}} \qquad \text{Equation 3-60}$$

$$Q_{Fe^{2+}} = \frac{\left[Fe^{2+}\right]_{1/2}}{\left[Fe_{(s)}\right]_{1/2}} \qquad \text{Equation 3-61}$$

$$Fe^{2+} + 3H_2O \rightleftarrows Fe(OH)_{3(s)} + 3H^+ + e^- \qquad \text{(RC3)}$$

$$E_{Fe(OH)_{3(s)}} = -\frac{RT}{zF}\ln\frac{\left[Fe(OH)_{3(s)}\right]_{1/2}\left[H^+\right]^3_{Fe,1/Fe,2}}{\left[Fe^{2+}\right]_{1/2}\left[H_2O\right]^3_{1/2}} \qquad \text{Equation 3-62}$$

$$Q_{Fe(OH)_3} = \frac{\left[Fe(OH)_{3(s)}\right]_{1/2}\left[H^+\right]^3_{Fe,1/2}}{\left[Fe^{2+}\right]_{1/2}\left[H_2O\right]^3_{1/2}} \qquad \text{Equation 3-63}$$

These are the reactions, which play a role in the charge transfer, creating a voltage across the cell. It is also important that the dissociation constant of water remains constant, the change in acidity is directly related to the dissociation of silica. Initial concentrations of H_2, H^+, H_2O are unity. The dissociation of water at one half-cell is considered, mainly at the side, which contains silica (HC, 1)

$$H_2O \rightleftarrows H^+ + OH^- \qquad \text{(R2)}$$

$$Q_{DISS,H_2O} = \frac{\left[OH^-\right]_1 \left[H^+\right]_1}{\left[H_2O\right]_1} \qquad \text{Equation 3-64}$$

Initial concentration of OH^- is retrieved from the dissociation constant of water and the hydrogen concentration at the interface of the stainless steel on half-cell 1 (HC, 1).

$$H_4SiO_4 \rightleftarrows H^+ + H_3SiO_4^- \qquad \text{(R3)}$$

After the convergence of the relaxation method, the hydrogen ion concentration is inserted into the equations below and compared with the values of Busey and Mesmer [42] to observe the discrepancy of silicic acid dissociation due to corrosion:

$$Q_{DISS,Si(OH)_4} = \frac{\left(\left[H^+\right]_{Fe,1,Si(OH)_4}\right)\left[H_3SiO_4^-\right]_1}{\left[Si(OH)_4\right]_1} \qquad \text{Equation 3-65}$$

$$x_{H^+,Fe,1,H_3SiO_4^-} = x_{H_3SiO_4^-} \qquad \text{Equation 3-66}$$

$$Q_{DISS,H_2O} = \frac{\left(x_{H^+,Fe,1,Si(OH)_4}\right)\left(x_{OH^-,1}\right)}{x_{H_2O,1}} \qquad \text{Equation 3-67}$$

These reactions are taken into account since they occur at high partial pressures of hydrogen of the interface of the metal, gas phase and Pt-wire, as is the case in this work. The reactions R1 and RC2 and RC3 are of significance as they provide the potential corresponding to the experimental voltage. R1, RC2 and RC3 dictate the relaxation of other reactions considered here.

The reaction quotients of R1, RC2 and RC2 above are coupled to each other to have a reaction model with respect to the relaxation method (see section 3.1.2.1). The reaction quotients are calculated from the redox potential of the reactions involved with the Nernst relation (equation 3-26). Upon convergence of the relaxation method, the hydrogen ion concentration is substituted in the dissociation of silicic acid (reaction R3)

An attempt to couple the quotients of all significant reactions in this investigation was done. It provides a relaxation of all the reactions in the solution that is proven in this investigation (presence of $Fe_2O_3/Fe(OH)_3$ by optical photography, SEM, EDX, Raman, H_2 by injection into cell, Fe^{2+} already by existence of goethite and H_2O due to aqueous solution used). However, only the pure/non-hybrid reactions are taken into account and the formation of the Si-O-Fe are not quantified.

This is rather done by the quotient-coupled relaxation of the above mentioned reactions of iron corrosion and dissociation of silicic acid. The hybrid reaction mechanism of Si-O-Fe is not clear, although some investigations are made previously [103], [104, 105]. It is not appropriate to use state of the art reaction mechanism before validation of the widely known mechanism. This should be done in a later stage.

The coupling of the reactions is shown in the Figure 3-8 (see page 37 of this work). The initiation of the corrosion together with the dissociation of the injected hydrogen is internally coupled:

$$Q_{DISS,CORR} = \frac{\left[H_2\right]_{1/2}}{\left[H^+\right]^2_{Fe,1/2}} \times \frac{\left[Fe^{2+}\right]_{1/2}}{\left[Fe_{(s)}\right]_{1/2}} \times \frac{\left[Fe(OH)_{3(s)}\right]_{1/2}\left[H^+\right]^3_{Fe,1/2}}{\left[Fe^{2+}\right]_{1/2}\left[H_2O\right]^3_{1/2}} \qquad \text{Equation 3-68}$$

The equation can be simplified as follows assuming that the concentrations of H_2O, H_2, $[Fe_{(s)}]$ and $Fe(OH)_3$ are unity:

$$Q_{DISS,CORR} \approx \left[H^+\right]_{Fe,1/2} \qquad \text{Equation 3-69}$$

Equation 3-68 is strictly used for the corrosion model calculations, which can be seen in Appendix 7.2.2. However, the above equation will prove to be useful for further explanations of the results for corrosion model (see section 4.2.1.3) as it is loosely based on equation 3-68.

The value of $Q_{DISS,CORR}$ is given by the product of individual dissociation constants in equation 3-68, respectively from their relation to the Nernst equation, $Q_{DISS,CORR,EXP}$ is given by:

$$Q_{DISS,CORR,EXP} \approx \exp\left\{-\left(\Delta E_{\exp}\right)\frac{zF}{RT}\right\} \qquad \text{Equation 3-70}$$

Passivation occurs in the presence and absence of silica. This equation must, given from the Nernst relation, give a measure of the concentrations (activity coefficient of unity). The concentration to be found is that of ΔH^+ as it is the key component and no corrosion occurs without its presence. The concentration of water, $[H_2O]$ and iron hydroxide, $[Fe(OH)_3]$ are unity by definition.

All the reactions in $Q_{DISS,CORR}$ are coupled with each other to allow relaxation of all concentrations involved, as they are determined with the key concentration of Δn_{H^+}.

3.4.4 Determination of total silicic acid species in the vapour phase

The vapour phase investigations of silicic acid is rare as its presence in the respective phase is negligibly low. However, it seems appropriate to pay some attention to its existence in the vapour phase. A report by Althoff, Unger and Schüth [34] show that zeolite syntheses in the vapour phase is not to be excluded. The presence and measurement of silicic acid species in the vapour phase was successfully conducted by Jacobson and Opila [106, 107]. They conducted the measurement with the transpiration method followed by gas chromatographic identification of the sole species ($Si(OH)_4$). The transpiration method consists of a hollow oven with the sample of solid phase silica in the oven. Water vapour is sent through the oven at given measurement temperatures and the vaporous silicic acid is carried away by the water vapour by means of the Stefan flow mass transfer effect ([108]-p.50 and p.120). The corresponding mass loss for a given period is recorded until the mass loss in the sample container or the mass surplus in the given volume of the sample stagnates. The concentration is calculated via the mass surplus, the volume flow and the time period towards equilibrium.

This design is not feasible to be realised for the purpose of this work, as Jacobson and Opila [106, 107] analysed the concentration at high temperature and respectively high

concentrations of silicic acid. The accuracy of the respective method may suffer at lower concentration, which is the case for silicic acid concentrations in this work. Another approach was attempted, in which the solubility of amorphous silica in solution was let to run in a Teflon coated stainless steel reactor of 220mL.

However only 170mL was filled with the solution with solid amorphous silica in the solution, the rest was left empty (with air) to allow the evolution of the vapour phase upon achieving the boiling point of the solution. The measurement involves deposition of the silicic acid species evolving in the vapour phase from the liquid phase in equilibrium on a vibrating quartz crystal at resonance frequency. It is connected to a 5V circuit to ensure constant vibration and an Arduino measurement device for frequency counting and data acquisition on a computer. Upon deposition, the frequency of the vibration changes and the mass surplus on the quartz crystal can be calculated via the difference in frequency by the Sauerbrey equation [109].

$$\Delta f = \frac{2 f}{A_{SiO2,q} \sqrt{\rho_{SiO_2,q} \mu_{SiO_2,q}}} \Delta mass \qquad \text{Equation 3-71}$$

This method is known as the quartz crystal microbalance method (QCM). It is a reverse method of the transpiration method and serves this work well as the transpiration method is used for very high temperatures (T > 1000K) and concentrations. This does not correspond to the temperatures of zeolite syntheses. The measurement of low concentration by the QCM method has been established [110].

4 Results

4.1 Results quantum chemical calculation of silicic acid species

The quantum chemical approach for silicic acid species and even building blocks of zeolites has been conducted successfully by Hill and Sauer [60, 61] and many others. Hill and Sauer were focused on the determination of optimal geometries and energies of zeolite primary and secondary building blocks by applying the HF-SCF (Hartree-Fock-Self Consistent Field) to the force field method introduced by Lasaga [63].

Others such as McIntosh [74] were interested in the kinetic model and the theoretical prediction of condensation reactions up to tetramers. Henschel et al. [69] made investigations on the reaction paths of dimerization, trimerisation and cyclisation reactions whereas Garofalini [58] simulated the condensation in terms of a network for 216 monosilicic acid molecules.

Solvent effects for silicic acids were simulated by Šefcík [20] by applying solvent models such as the COSMO model. Montero-Cabrera [65] modelled the encapsulation the silicic acid of interest by an optimal number of water molecules and retrieved hydration energies thereof. Dissolution studies of quartz were made by Xiao and Lasaga [62]. As some work has been done in this field for silicic acid species, the quantum chemical method of calculating thermodynamic properties seems to be appropriate. In this work, it is not attempted to reproduce results determined by the literature but rather to use them as validation tools to be consistent with known literature.

The optimal geometries of monosilicic acid and disilicic acid (or pyrosilicic acid) are given in literature and are consistent to our results [13-15, 18, 19, 76]. As mentioned earlier, simple-cyclic (see page 22 of this work) and linear trimers and tetramers are considered in this study. Furthermore, fused-cyclic and branched-cyclic pentamers to octamers are investigated. The cyclic (see page 22 of this work) and branched-cyclic pentamers to octamers are taken from the consistent recommended structures of Pelster and Knight [13, 18, 19]. The branched-cyclic pentamers to octamers are just the cyclic tetramers, which are branched namely by replacing one trihydroxysilyl group with one of the 2 hydroxyl-groups at Si-site of the cyclic tetramer. This yields the necessary branched-cyclic pentamer to octamers if 1 to 4 trihydroxysilyl groups are substituted, respectively. The silicic acid species which, were calculated, are discussed in section 4.1.1.

4.1.1 Determination of the standard Gibbs free energy, enthalpy, and entropy for cyclisation and condensation reactions

This work does not attempt to make an in-depth study of quantum chemical procedures with respect to the silicic acid systems considered here. It is rather treated as a tool to achieve validation of our results and useful information for the determination of the standard free energy, enthalpy and entropy of reactions mentioned. The optimised calculation of literature

serves as good reference. It is also done to determine the equilibrium constants (see equation 3-20) of each reaction involved in Figure 3-5. In this work, the free energy, enthalpy and entropy have negligible change with temperature (see Appendix 7.8.2). Hence, the equilibrium constant is derived from the second law of thermodynamics at standard conditions, which is better known as the van't Hoff equation.

This provides a direct relation of the second law of thermodynamics and the van't Hoff equation (see derivation in Appendix 7.8.1), as standard reaction energies and entropies are considered. Temperature dependent reaction energies and entropies calculated show negligible difference (see Appendix 7.8.2). The slope corresponds to $-d_rh°/RT$ and the intersect of the y-abscissa $d_rs°/RT$. The reaction energies are calculated in Hartrees and then converted to kJ/mol with the equivalence of 2625 kJ/mol to 1 Hartree. Hence, we determine all equilibrium constants by the van't Hoff equation, as this will be a consistent comparison with experimental results. Experimental results in literature [22] were calculated using the van't Hoff equation.

Solvent effects of silicic acid species in water are complicated due to hydrogen bridging. These occur in products and reactants for condensation and cyclisation reactions and the errors of solvent effects may compensate for energy differences. However, the solvent effects are taken into account for dissociation reactions as it stabilises the anionic silicic acid species.

To calculate the free energy, frequency calculation of the geometry-optimised system (for a specific molecular species) is used. The frequency calculation takes the theory of the harmonic oscillator into account. The following energies resulted from the calculations done in Gaussian 09 [111].

The reactions in section 3.2 (table 3-1 in page 23 and figure 3-6 in page 28 of this work) are taken into account. These reactions represent the general reactions based on literature information. The theoretical explanations of this equilibrium reaction model is based on McIntosh [74], who mentioned the exclusion of trimolecular reactions and hence the reaction scheme is reduced to a maximum of dimolecular reactions for the condensation reaction.

Other dimerization, trimerisation and tetramerisation reactions are described by Garofalini, Henschel and McIntosh, respectively [58, 59, 69, 74, 75, 81]. The solvent effect of aqueous

silica has been described by Sefcík [20]. Montero-Cabrera has simulated the solvent effect locally by encapsulating solvent molecules (H_2O) around the silicic acid species of interest [65].

The condensation reactions comprises linear silicic acids for reactions K1-$_{Si,i}$= K1-$_{Si1}$ and K1-$_{Si2}$. Linear trisilicic acid (for reaction K1-$_{Si3}$) and tetrasilicic acid (for reaction K1-$_{Si4}$) structures are taken into account for the condensation reactions as well. Other higher order linear species do not exist in absence of structure directing agents since they are energetically less stable ([73] -p.57-59). Adequate proof of this reason is based on the consistent silicic acid structures elucidated by Knight et al. and Pelster et al. [13-15, 18, 19, 76].

Other higher order branched-cyclic species (for reactions K2-$_{Si,i}$= K2-$_{Si5}$, K2-$_{Si6}$, K2-$_{Si7}$ and K2-$_{Si8}$) are simply substitution of the trihydroxysilyl-groups of cyclotetrasilicic acid (see table 4-1). These species are detected in the ESI-MS spectra and successfully identified by Knight et al. consistently [18, 19]. Hence, these structures are taken as model structures in our calculation in figure 3-5. The other reason for choosing these structures is that the intramolecular reaction towards cyclisation is more probable than intermolecular reaction between two reactants [69].

Cyclic structures of common nature (in zeolite syntheses) are taken, which are qualitatively identified by Pelster by ESI-MS [13-15, 76] as well as Knight by NMR [18, 19]. The silicic acid species calculated has to correspond to the species detected in ESI-MS and NMR by Pelster [13-15, 76] and Knight [18, 19].

Table 4-1 – The optimized geometries of the silicic acid species involved with their respective nomenclature and molar mass[36].

Branched-cyclic species/ molar mass	Cyclic species / molar mass
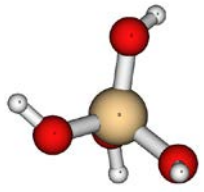 Monosilicic acid – *Si*1 / 96	No feasible cyclic structure at equilibrium

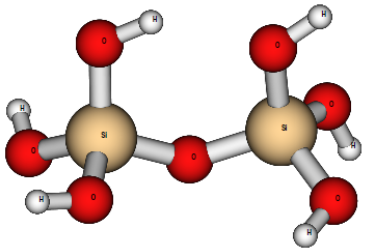 Disilicic acid – *Si*2 / 174	No feasible cyclic structure at equilibrium
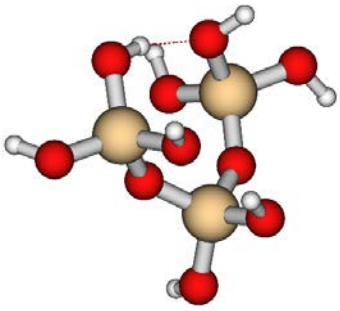 Trisilcic acid *Si*3 / 252	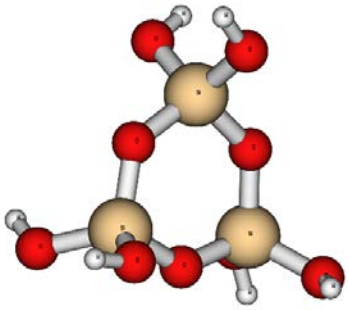 Cyclotrisilicic acid – *Si*3*cyc* / 234
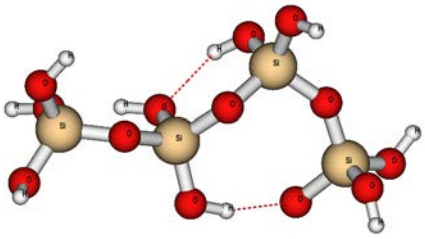 Tetrasilicic acid – *Si*4 / 330	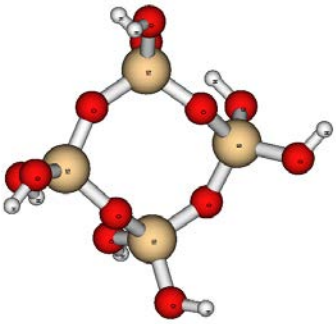 Cyclotetrasilicic acid – *Si*4*cyc* / 312
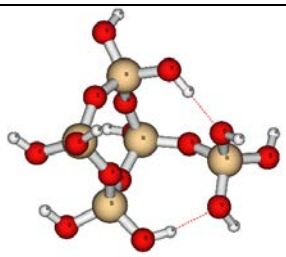 Pentasilicic acid – *Si*5 / 390	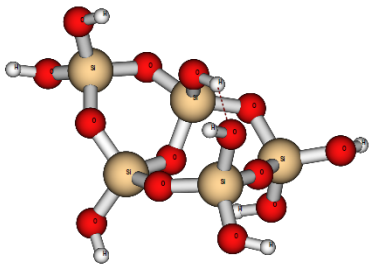 Cyclopentasilicic acid – *Si*5*cyc* / 372
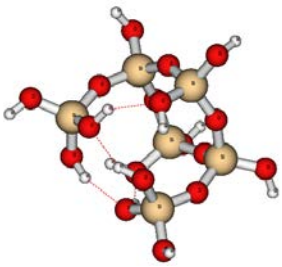 Hexasilicic acid – *Si*6 / 468	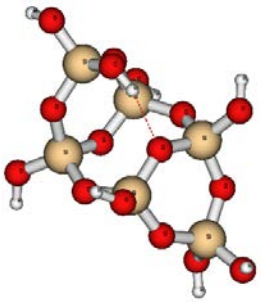

	Cyclohexasilicic acid – *Si*6*cyc* / 432
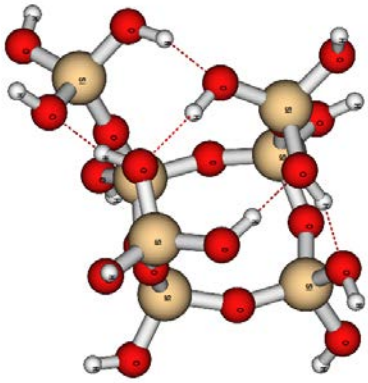 Heptasilicic acid – *Si*7 / 546	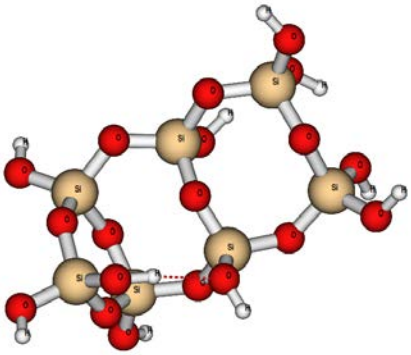 Cycloheptasilicic acid – *Si*7*cyc* / 510
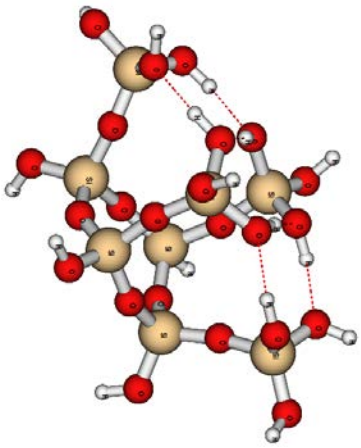 Octasilicic acid – *Si*8 / 624	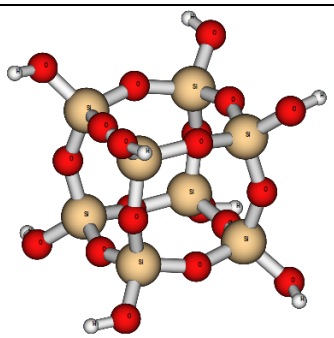 Octahydroxyoctasilsequioxane – *Si*8*cyc* / 552

The structures considered here are taken from consistent results from Knight et al. [18, 19] and Pelster et al. [13-15, 76]. The constitutions considered here are not all the possibilities which exist, as there would be too many to investigate [13].

The most plausible molecular structures in Table 4-1 above are determined by chemical intuition, which are consistently mentioned by Knight et al. [18, 19] and Pelster [13-15]. Ascending from Si1 to Si8 and Si3cyc to Si8cyc respectively, the constitutions of most possible occurring species are taken into account. Hence, these values are to be treated with care. It is important to emphasize here that only the trends of the calculations have been analysed mainly for the respective reactions energies and have good agreement with these respective sources as will be discussed further.

Table 4-2 – The standard enthalpy, free energy and entropy of reaction for the cyclisation reaction

T=298.15K	C1-Si_{3cyc}	C1-Si_{4cyc}	C1-Si_{5cyc}	C1-Si_{6cyc}	C1-Si_{7cyc}	C1-Si_{8cyc}
Δh^{o}_{cyc} d_rh°/(kJ/mol)	50.26	20.08	163.45	142.93	168.44	175.67
Δg^{o}_{cyc} /(kJ/mol)	6.33	-16.95	126.79	47.52	89.65	-7.09
Δs^{o}_{cyc} /(kJ/mol K)	$1.47x10^{-1}$	$1.24x10^{-1}$	$1.23x10^{-1}$	$3.20x10^{-1}$	$2.64x10^{-1}$	$6.13x10^{-1}$

The enthalpies, free energies and entropies of the cyclisation reactions are shown in Table 4-2. With increasing temperature, the positive entropy of reaction leads to lower free energies. It can be concluded that the reaction is favoured by the second law of thermodynamics.

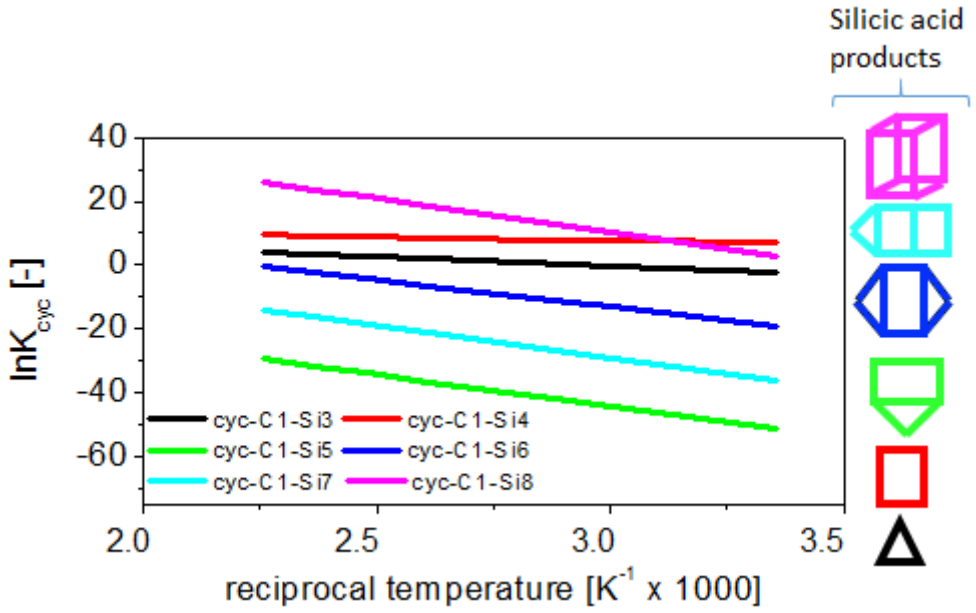

Figure 4-1 – The logarithmic equilibrium constants of cyclisation reactions.

The figure 4-1 depicts the equilibrium constants for cyclisation reactions (see section 3.2) of cyclotrislicic acid (Si3cyc) to octahydroxyoctasilsequioxane (Si8cyc) calculated with the B3LYP method. The formation energies are lower than reported Hartree-Fock-Self Consistent Field energies by Hill and Sauer and DFT energies calculated by Pereira for cyclic tri-,tetra-, penta-, hexa-, and octasilicic acids [60, 112], which may be due to the varying method or smaller basis set used.

The equilibrium constants in this investigation are calculated from the van't Hoff equation (equation 3-21). Under the consideration of standard reaction energies and entropies, the van't Hoff equation is directly related to the second law of thermodynamics (see Appendix 7.8.1):

$$\ln K_p = \frac{\Delta s^o_{reaction}}{R} - \frac{\Delta h^o_{reaction}}{RT}$$ Equation 4-1

From the equation above, the reaction is favoured at higher temperatures due to the positive standard enthalpy of reaction (negative slope). However, the equilibrium constants for C1-Si_{5cyc}, C1-$_{Si6cyc}$ and C1-$_{Si7cyc}$ are in the negative region. This leads to the lower concentrations of the respective cyclic silicic acid species. This may be due to the bond strains (Si-O-Si) experienced by the cyclic structure, mentioned by Pereira [112, 113]. Therefore the existence or concentration of these cyclic species is low in the gas phase generally, consistent with the explanations of McIntosh [74].

Nevertheless, the equilibrium constants are in the positive region for C1-$_{Si4cyc}$ and C1-$_{Si8cyc}$. C1-Si_{3cyc} has a transition from the negative region to the positive region at higher temperatures due to the positive enthalpy (negative slope). C1-$_{Si3cyc}$, C1-$_{Si4cyc}$ and C1-$_{Si8cyc}$ lead to higher concentrations in the gas phase, as Pereira consistently mentioned the near cyclic form of linear trimers and tetramers [112], leading to a favoured cyclisation of cyclotrisilicic acid (C1-$_{Si3cyc}$) and cyclotetrasilicic acid (C1-$_{Si4cyc}$).

This is valid for octasilicic acid as the 4-trihydroxysilyl groups favourably form the cage structure. The cyclisation of the branched-cyclic heptasilicic, hexasilicic and pentasilicic acid is slightly more difficult. This is due to the absence of one, two and 3 trihydroxysilyl groups to form the cyclic structure. Hence, the branched-cyclic structure undergoes strain at the Si-O-Si bonds to form the cyclic structure. This is mainly proven by the negative equilibrium constants of C1-$_{Si5cyc}$, C1-$_{Si6cyc}$ and C1-$_{Si7cyc}$.

The following can be deduced from the cyclisation reactions:

- Si_{3cyc}, Si_{4cyc} and Si_{8cyc} are dominant in gas phase.
- Si_{5cyc}, Si_{6cyc} and Si_{7cyc} are not dominant in gas phase due to Si-O-Si bond strain of the fused-cyclic structure of these species.
- Dominancy generally increases at higher temperatures due to positive entropic effects as one silicic acid species yields another silicic acid species with an excess of water (1 reactant yields multiple products) and the positive enthalpy (negative slope of the van't Hoff equation (equation 3-21)).

Table 4-3 – The standard enthalpy, free energy and entropy of reaction for the condensation reaction

T=298.15K	K1-$_{Si2}$	K1-$_{Si3}$	K1-$_{Si4}$	K2-$_{Si5}$	K2-$_{Si6}$	K2-$_{Si7}$	K2-$_{Si8}$
Δh^{o}_{mixed} /(kJ/mol)	-14.72	-23.58	-12.84	-11.74	-57.45	-38.64	-37.50
Δg^{o}_{mixed} /(kJ/mol)	-12.59	-14.50	-9.42	-36.90	-44.99	-34.20	-27.56
Δs^{o}_{mixed} /(kJ/mol K)	-7.13×10^{-3}	-3.05×10^{-2}	-1.15×10^{-2}	8.44×10^{-2}	-4.18×10^{-2}	-1.49×10^{-2}	-3.33×10^{-2}

The enthalpies, free energies and entropies of the condensation reactions are shown in Table 4-3. The standard entropy of reaction is negative for all condensation reactions with the exception of pentasilicic acid. This leads to higher free energies with increasing temperature, except for pentasilicic acid due to its positive entropy. This is due to the removal of two water molecules instead of a single water molecule as for other condensation reactions.

However, all condensation reactions are exothermic and lead to the conclusion that the reactions are rather favourable. Hence, it can be concluded that the second law of thermodynamics favours all condensation reactions.

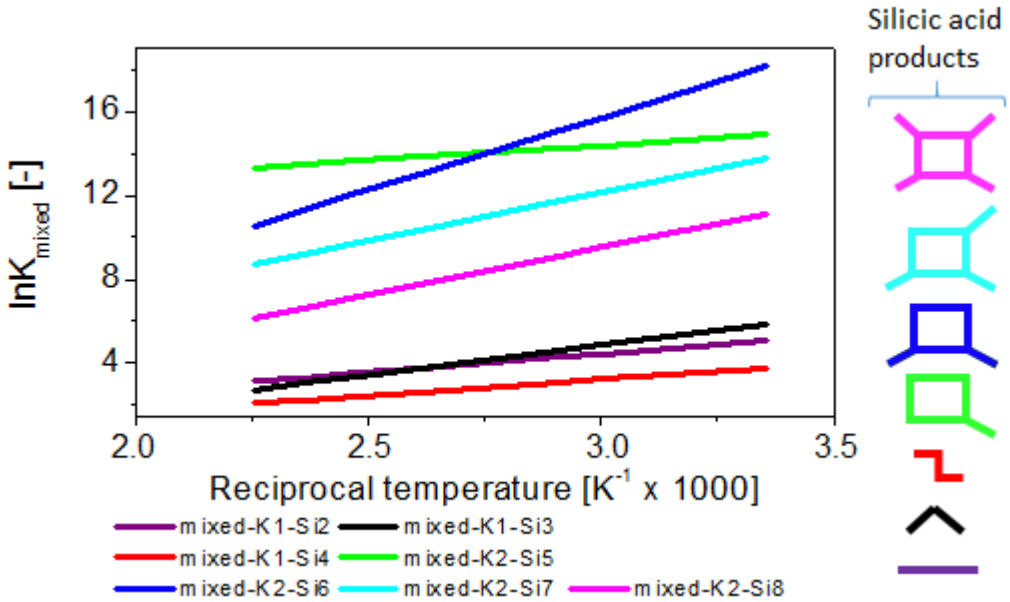

Figure 4-2 – The logarithmic equilibrium constants of condensation reactions.

The figure 4-2 shows the temperature dependence of the equilibrium constants for polymerisation of linear and branched-cyclic silicic acid species (K1-$_{Si2}$ to K1-$_{Si4}$ and K2-$_{Si5}$ to K2-$_{Si8}$). This investigation attained lower energies than provided by Newton and Gibbs for

monosilicic acid and disilicic acid [66] and Pereira for mono-, di-, tri-, and tetrasilicic acid with comparable bond angles and lengths [112, 113].

All species have attain lower formation energies compared to the HF-calculations of Newton et al. [66] with a STO-3G basis set and Pereira using the preceding density functional method [112, 113]. From the observation of the equilibrium constant, the magnitude of the condensation reactions decreases with increasing temperature due to the positive slope (negative standard enthalpy of reaction).

The logarithmic equilibrium constants are all in the positive region, which leads to a negative Gibbs free energy at the respective temperatures. The equilibrium constants for $K1\text{-}_{Si2}$, $K1\text{-}_{Si3}$, $K1\text{-}_{Si4}$ have similar ranges between 2 and 5. This leads to the conclusion that the linear condensation (K1) has a distinguishable equilibrium constant than branched condensation (K2). The addition of a monosilicic acid to linear dimer and trimer has similar equilibrium constants.
The branched condensation reaction $K2\text{-}_{Si5}$, $K2\text{-}_{Si6}$, $K2\text{-}_{Si7}$ and $K2\text{-}_{Si8}$ have equilibrium constants favourable towards the formation of products. $K2\text{-}_{Si5}$, $K2\text{-}_{Si6}$, $K2\text{-}_{Si7}$ and $K2\text{-}_{Si8}$ have equilibrium constants ranging between 5 and 18 in the temperature range depicted. These values for $K2\text{-}_{Si5}$, $K2\text{-}_{Si6}$, $K2\text{-}_{Si7}$ and $K2\text{-}_{Si8}$ leads to higher product concentrations compared to $K1\text{-}_{Si2}$, $K1\text{-}_{Si3}$ and $K1\text{-}_{Si4}$.

The following can be deduced from the condensation reactions:

- All reactions are dominant in the gas phase (due to strong intramolecular effects)
- Dominancy decreases at higher temperatures due to resulting positive slope from the negative enthalpies.
- Reaction energies and entropies depend strongly on the geometry of the silicic acid species.

4.1.2 Quantum chemical values for dissociation constant calculations with solvent effects

There are some intermediate reactions, which involve the dissociation of silicic acid into its anionic form. Intermediate reactions are not considered here as only thermodynamically

favoured reactions are taken into account. Nevertheless, it is worth to note some valuable information on the dissociation of the silicic acid species. It facilitates the reaction towards the formation of the silicic acid product of concern, as reported by Trinh et al. [82]. Dissociation reactions (D1 and D2) are reformulated for the inclusion of hydroxonium ions as it describes the true reaction mechanism in the solution better and no electronic structure exist for an H^+ ion by definition.

Hydrogen ions may facilitate the ring closure of mixed (linear and branched-cyclic) species by means of dissociating water to hydrogen ions and hydroxyl ions. The hydrogen ions may facilitate the OH group of the trihydroxysilyl group to bond with another OH group of a neighbouring Si-Atom as described by Trinh et al. [82]. This supports the reduction of the mixed species and increase of cyclic species (see figure 3-6) with temperature.

However, this can be at least equally facilitated by lower polymeric silicic acid species (mostly monosilicic acid) as the dissociation constant of silicic acid is reported to be higher than of water ([37]-p.123). This may be possible as the condensation of disilicic to octasilicic acid is positive for mixed species in this investigation. As the reaction involves monosilicic acid to higher order mixed species, this should involve the dissociation of monosilicic acid to an intermediate $H_3SiO_4^-$ anion.

This would mean a dissociated monosilicic-ion reacts with a mixed silicic acid species. They form either another mixed or cyclic silicic acid species (see figure 3-6) with an additional Si-atom as reported by Garofalini and McIntosh [58, 74]. This can be taken to be a significant intermediate reaction mechanism of the condensation reaction, as water is removed from the condensation reaction of mixed species, however not in equilibrium. It can also cause a cyclisation reaction.

On the other hand, intramolecular reactions are more likely to occur than intermolecular reactions. Hence, it would be of great interest to couple these dissociation reactions of silicic acid in the reaction model as well. The description of the role of dissociated silicic acid species and H^+ is given in figure 4-3.

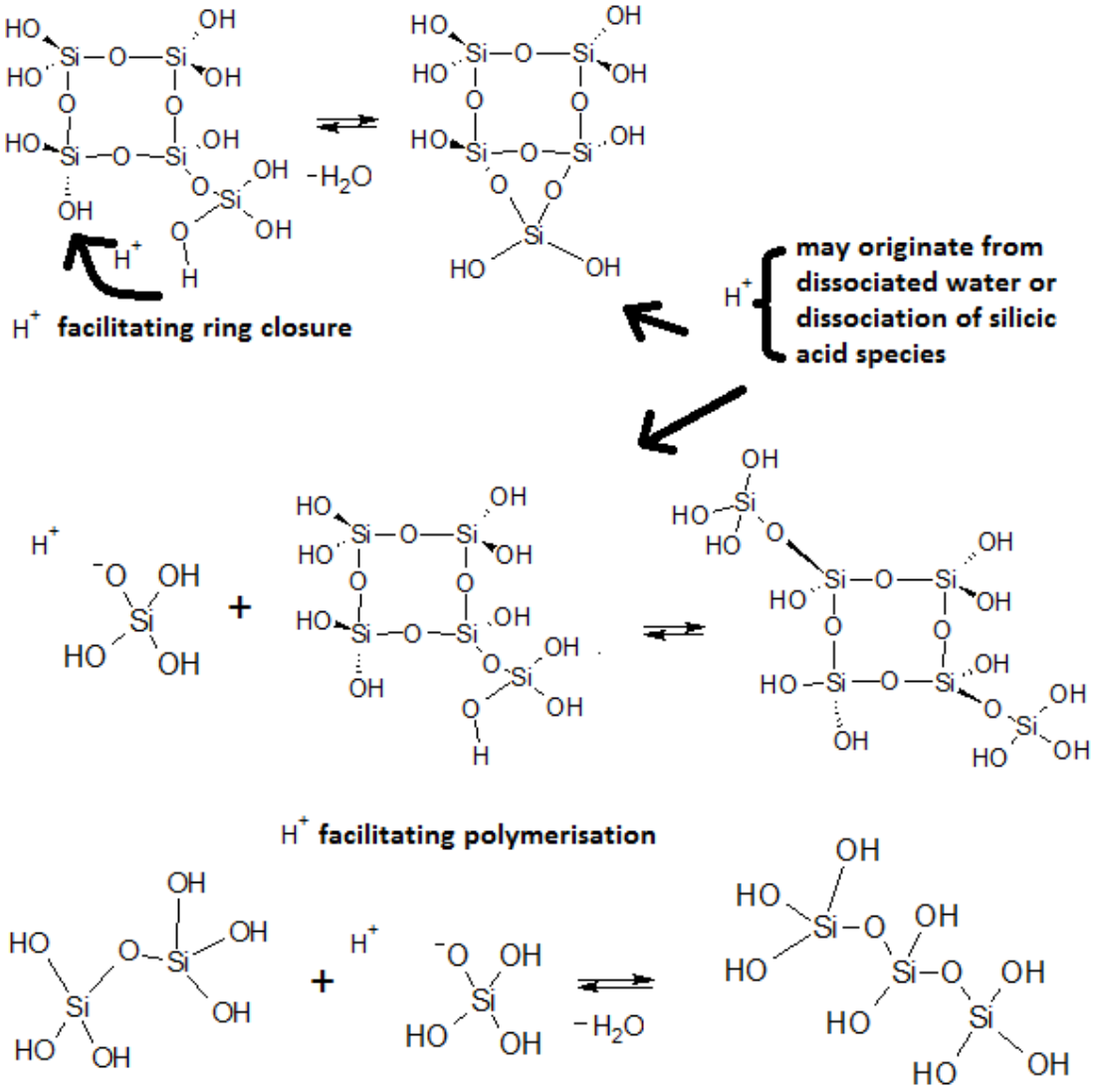

Figure 4-3 – A possible intermediate reaction mechanism for the condensation and cyclisation reactions.

The values are however too low compared to the reported experimental values by Busey and Mesmer [42]. They cannot be used as values in the reaction model. The starting values are taken from literature. The values are further improved towards convergence of the equilibrium reaction model.

Table 4-4 – The standard enthalpy, free energy and entropy of reaction for the dissociation reactions for cyclic (simple-and fused-cyclic –see page 22) species with the consideration of solvent effects

T=298.15K	D2-Si3cyc	D2-Si4cyc	D2-Si5cyc	D2-Si6cyc	D2-Si7cyc	D2-Si8cyc
Δh^{o}_{diss} /(kJ/mol)	223.91	210.06	210.19	200.90	208.69	97.55
Δg^{o}_{diss} /(kJ/mol)	221.03	216.74	212.37	201.02	211.11	108.40
Δs^{o}_{diss} /(kJ/mol K)	9.64x 10^{-3}	-2.24x^{-2}	-7.29x10^{-3}	-3.87x10^{-4}	-8.12x-10^{-3}	-3.64x10^{-2}

Table 4-4 shows standard enthalpies, Gibbs free energies and entropies for the dissociation reaction for all cyclic (simple and fused - see page 22 of this work) silicic acid species. The entropies depicted in the table for all species are negative except for D2-$_{Si3cyc}$. Apart from this exception mentioned, the dissociation of cyclic species leads to the increase of the Gibbs free energy of reaction with temperature. D2-$_{Si3cyc}$ leads to a decrease in Gibbs free energy, as the entropy is positive.

There is a convention of a reduction in free energy for dissociation reactions, starting from one reactant to give two products. Its entropy should be positive and this leads in a decrease in the free energy. It is to be emphasised here that the consideration of H_2O and H_3O^+ is taken into account.

The dissociation reaction here results in two products from two reactants. Hence, the conventional observation of positive entropies for dissociation reactions is occasionally not observed. This may be due to the different levels of free energy and enthalpy of formation for the neutral and anionic cyclic (simple and fused – see page 22) silicic acid species, compared to that of H_2O and H_3O^+.

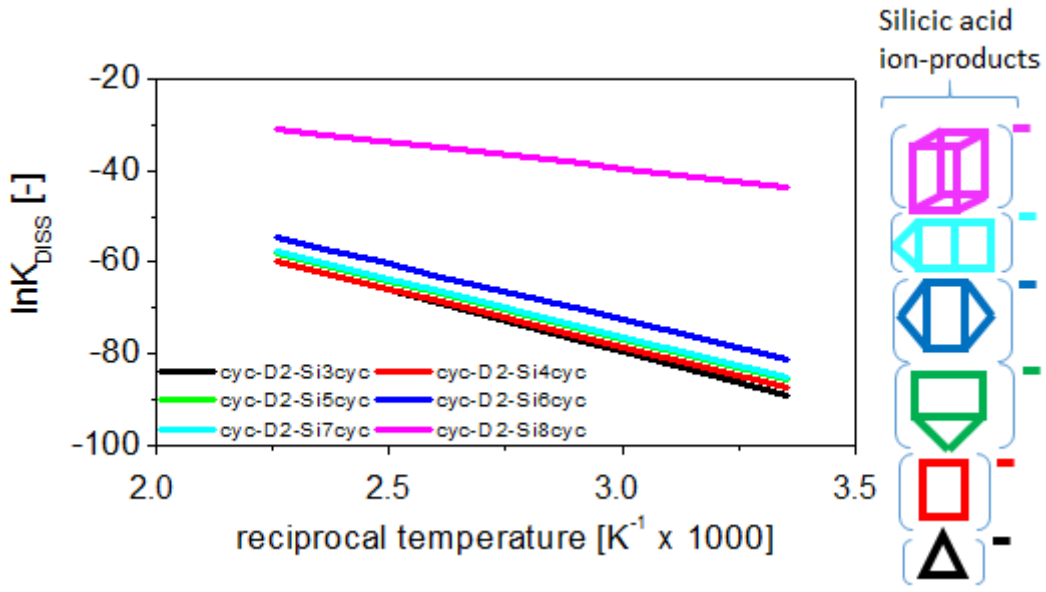

Figure 4-4 – The figure above presents the logarithmic dissociation values for cyclic species determined with the B3LYP method with solvent effects (PCM).

The figure 4-4 shows the equilibrium constants for dissociation reactions of cyclic species with the consideration of solvent effects by the PCM. All standard enthalpies of reaction are positive, leading to a negative slope and to the increase in the equilibrium constant with temperature. However, equilibrium constants for all cyclic dissociation reaction are extremely endothermic at all temperatures considered. They are too low to have any significant concentration shift to the product side (anionic silicic acid species).

Table 4-5 – The standard enthalpy, free energy and entropy of reaction for the dissociation reactions for mixed (linear and branched-cyclic) species with the consideration of solvent effects

T=298.15K	D1-$_{Si1}$	D1-$_{Si2}$	D1-$_{Si3}$	D1-$_{Si4}$	D1-$_{Si5}$	D1-$_{Si6}$	D1-$_{Si7}$	D1-$_{Si8}$
Δh^{o}_{diss} $d_rh°$/(kJ/mol)	247.96	229.33	183.69	176.13	210.11	45.33	189.22	172.69
Δg^{o}_{diss} /(kJ/mol)	245.69	226.85	184.03	194.61	205.61	47.96	181.97	163.57
Δs^{o}_{diss} /(kJ/mol K)	$7.61x10^{-3}$	$8.33Ex10^{-3}$	$-1.13x10^{-3}$	$-6.20x10^{-2}$	$1.51x10^{-2}$	$-8.82Ex10^{-3}$	$2.43x10^{-2}$	$3.06x10^{-2}$

Table 4-5 show the enthalpy, free energy and entropy for dissociation reaction of mixed silicic acid species. The intersections of the entropy depicted in the table are negative for D1-$_{Si3}$ (linear), D1-$_{Si4}$ (linear), and D1-$_{Si6}$ (branched-cyclic).

Apart from these exceptions mentioned, the dissociation of other dissociation reaction of mixed species leads to the decrease of the Gibbs free energy of reactions. D1-$_{Si1}$ (linear), D1-$_{Si2}$ (linear) and D1-$_{Si5}$ (branched-cyclic), D1-$_{Si7}$ (branched-cyclic) and D1-$_{Si8}$ (branched-cyclic) lead to a decrease in the Gibbs free energies, as the entropies are positive.

The dissociation reaction with positive entropy involves a proton and anionic species as two products form from one reactant, hence decreasing the free energy. However, the dissociation reactions above consider of H_2O and H_3O^+ in the dissociation reaction. This leads to two products from two reactants, which may lead to negative entropies for dissociation reactions. This may occur with the different levels of free energy and enthalpy of formation for the neutral and anionic mixed silicic acid species, compared to that of H_2O and H_3O^+.

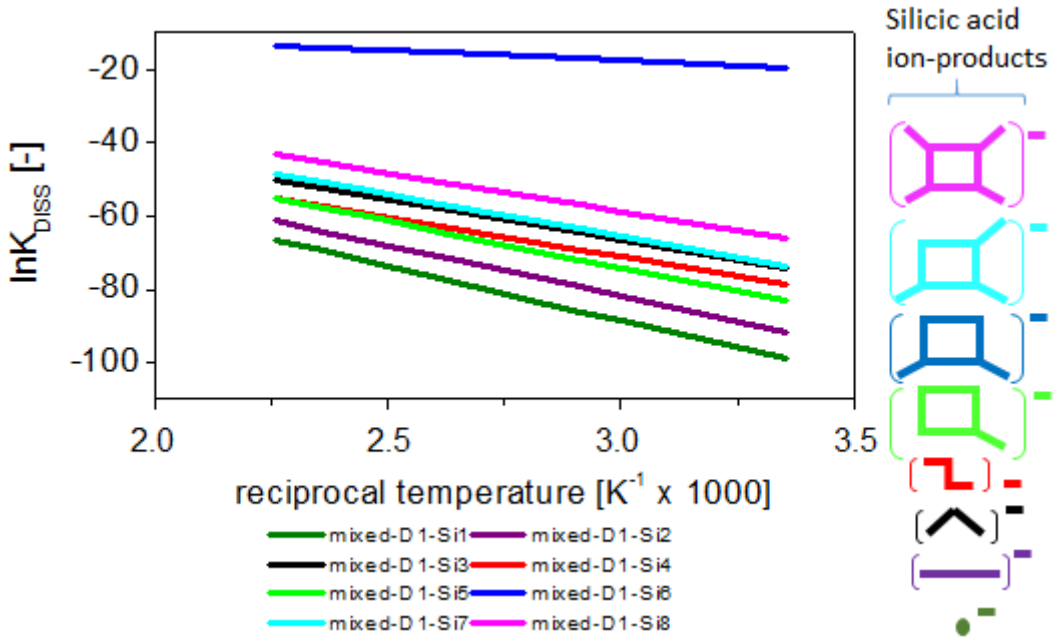

Figure 4-5 – The figure above presents the logarithmic dissociation values for mixed (linear and branched-cyclic) species with the B3LYP method with solvent effects (PCM).

The figure 4-5 shows the dissociation constants for mixed species. All standard enthalpies of reaction are positive, leading to a negative slope. The equilibrium constants hence increase with temperature. However, the equilibrium constants of all the mixed dissociation constants are significantly low, leading to a negligible presence in the solvent phase.

All dissociation reactions, independent of their values, show a significant increase in the dissociation constant with increasing temperature. This shows that the dissociation constant calculated increases with temperature. The results of the quantum chemical procedure provide hints on the solvent effects as well. The products are anionic silicic acid species provided in figure 3-6.

4.2 Experimental results

4.2.1 Liquid phase experiments

4.2.1.1 Solubility experiments

Solubility measurements from 25°C to 170°C for pH 12 and 13 was conducted in a custom designed electrically heated autoclave at elevated temperatures and a glass reactor with temperature regulation at 25°C at pH 7.

Experimental results provide the solubility of amorphous SiO_2 in water, which is taken directly taken as the equilibrium constant of silicic acid (see equation 3-24). The results in this work is not emphasised on the quantitative nature of the results but rather the qualitative method on the approach to elucidate the thermodynamic properties of silicic acid involved in the initial stages of the zeolite syntheses.

4.2.1.1.1 Setup of apparatus at 25°C

Measurement at 25°C and pH =7 (light bulb experiment).

The setup in the following figure 4-6 is made for the experiment at 25°c and pH=7. The other experiments at temperatures from 25°C to 170°C and higher pH (12 and 13) were done in an autoclave, which is shown in figure 4-7.

A glass reactor was filled with the solvent of water and the powdered silica from dried (105°C for 24 hrs and calcined 550°C for 24 hrs) LUDOX AS-40 was added and mixed for a period of 40 days to achieve equilibrium [54].

An X-Ray diffractogram of the sample was taken and the amorphous nature is proven (see Appendix 7.4-figure 7-7). It is concluded that LUDOX AS-40 exhibited amorphous silica characteristics as mentioned from the data sheet of LUDOX from Sigma Aldrich.

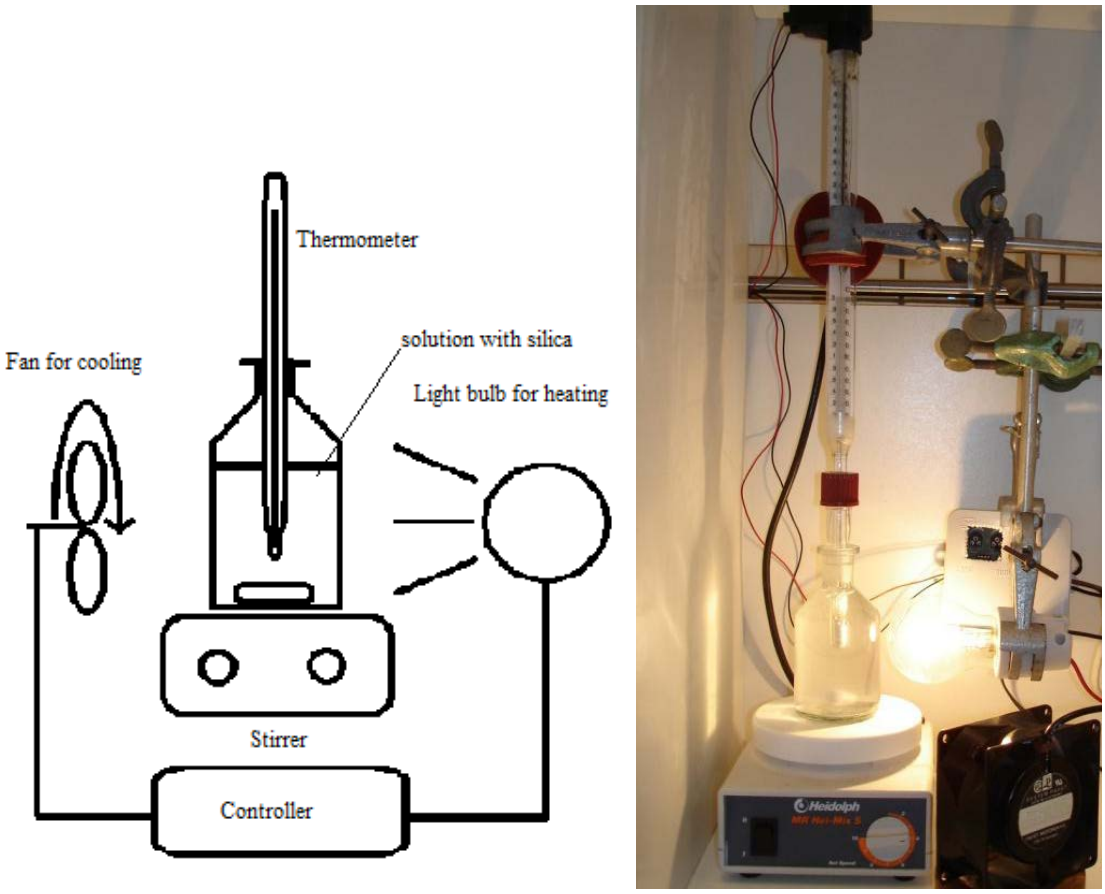

Figure 4-6 – The schematic drawing of the apparatus for the solubility measurement of amorphous silica at 25°C is shown.

4.2.1.1.2 Setup of apparatus for measurements from 60°C to 170°C

Measurement at temperatures from 60 to 170°C at pH=7 and 25°C to 170°C at pH =12 to 13.

A Teflon-coated stainless-steel autoclave is used for this purpose. The autoclave from Berghof® can withstand a pressure of 200 bars and 200°C (restricted due to Teflon coating melting point 220°C). Therefore, the experiments are conducted until 170°C. As the temperature increases from 60°C to 170°C, the time of experiment was reduced as equilibrium was achieved more rapidly. This statement also holds for the increase in pH and the time for equilibrium is shown in the table 4-6 below.

Table 4-6 – The time period taken to reach equilibrium at different temperature and pH-values for the solubility of silicic acid is shown in the table below.

Temperature(ϑ)/time	Time(days) for pH=7[54]	Time(days) for pH=11.5[47, 48, 54]	Time(days) for pH=12.5[47, 48, 54]
25°C	40	3	1
60°C	21	2	1
70°C	14	1	1
110°C	7	1	1
130°C	7	1	1
150°C	7	1	1
170°C	7	1	1

The reaction time allowed for dissolution of silica to silicic acid is shown in table 4-6. It was proven by Elmer et al. [48], that the concentrations achieved after a few days at temperatures higher than 60°C near the neutral pH achieved equilibrium conditions, deviating by 10-15%. However, Alexander showed that the concentration might further increase at a higher pH if left away for up to 6 months, given that the ionic strength of the solution is sufficiently high. The solutions in this work do not have high ionic strength as compared to the work of Alexander [47].

Figure 4-7 – The high pressure and temperature apparatus used for the solubility measurements for the liquid phase and detection of vapour phase silicic acid at 60-170°C and pH-values of 7, 12, and 13.

4.2.1.1.3 Results of solubility measurements

4.2.1.1.3.1 UV-Vis Results

UV-Vis measurements are done to validate the presence of silicic acid in the sample solution. Calibration measurements for neutral solutions are done for 100ppm, 250ppm, 500ppm, 1000ppm. Calibration measurements for pH=12 and pH=13 are done for higher concentrations (100ppm to 10000ppm).

Calibration solutions are prepared by dissolving 1g of amorphous silica in 1M of NaCl solution (solution A) weighing 1kg. This corresponds to 1000ppm of silicic acid and the addition of NaCl to the solution does not affect the intensity of the molybdate complex [37] – (p.44). Only the Si-atom fits in the octahedral formed cage of the $Mo_{12}O^{-}_{40}$ anion complex. Further calibration solutions are prepared by further diluting the solution A two-fold, four-fold and ten-fold with distilled water.

A 96% H_2SO_4 solution was diluted to a 4% solution (solution B-50mL). 5g of ammoniumheptamolybdate tetrahydrate ($(NH_4)_6Mo_7O_{24}*4H_2O$) is added to 40ml distilled water and 2.36g of 25% NH_4OH solution and diluted to 50mL (solution C). Distilled water, solution B, and solution C were mixed with a 5:2:1 ratio (solution D). 8 mL of the solution D is mixed with the 2mL calibration solution (solution A) or the sample solution SS containing silica (Solution E). Solution E is diluted 50-fold for neutral solution and 250-fold (Solution F) to reduce the colour intensity to obey Beer-Lambert's Law [97].

The solution F is measured with a SPEKOL 1000 spectrometer from Analytik Jena at 320 to 700nm. The value at 410nm is of great importance as the absorption value has a linear dependence on the concentration of silicic acid at this wavelength. Calibration measurements were done for every sample solution measured from 25°C to 170°C for pH 7, 12 and 13 (see example at 110°C at pH=12 in appendix 7.1).

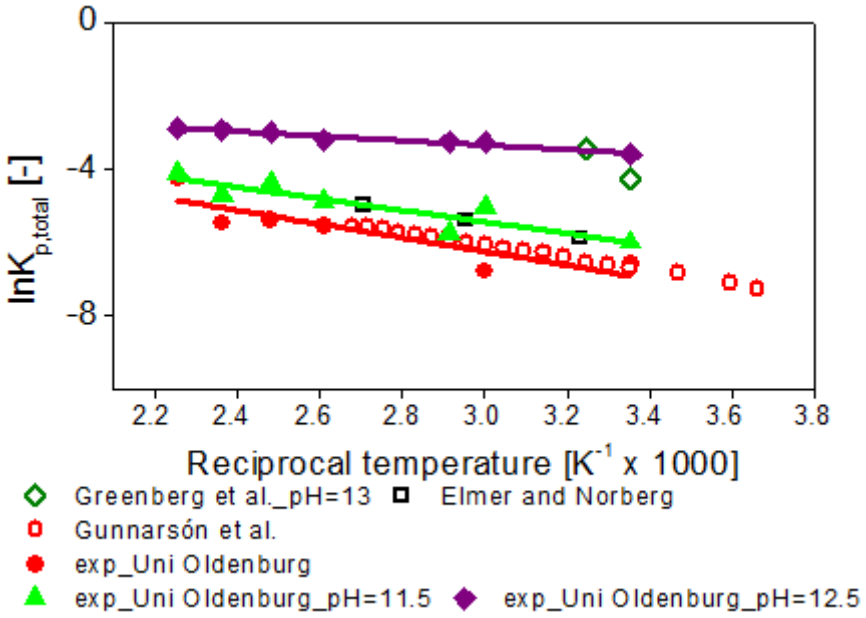

Figure 4-8 – The experimental results above is shown for UV-Vis measurements with comparison to literature data [22, 48, 53]. The equation of the linear curves in the diagram for all pH values are shown in the appendix 7.1 with the degree of fitting to the data points.

The figure 4-8 above shows the total equilibrium constant of dissolved silicic acid. It represents the total silicic acid species dissolved as the UV-Vis measurement solution was left to react for at least 30 minutes. According to Iler [37]-(p.96 and p.196), all silicic acid species react after 10-30 minutes of reaction time. From the diagram, the amount of dissolved silica increases with temperature and pH value.

4.2.1.1.3.2 ESI-MS (Electron Spray Ionisation- Mass Spectrometry) results

The ESI-MS measurement instrument is of the model ESI- Q-TOF Premier from the company Micromass Technologies. The ESI-MS measurements for negatively charges species were done to validate the existence of multiple silicic acid species for ab-initio calculations and further equilibria calculations.

1µL of the SS was diluted with 1.5mL of methanol. A 250µL Hamilton syringe was used to inject the prepared solution into the ionization chamber of the ESI-MS instrument at 120°C. The voltage between the terminals is set to 3kV and the potential at the cone tip is set to 24kV to facilitate the trajectory of ionic species towards the cone tip.

Many of the species identified by Pelster is also observed here [13]. We also observe other species, in which the molecular formulae are given by the mass spectrometry software MassLynx V4.0 developed by the same company. Unfortunately, it is not feasible to apply all species into our calculation, as there are too many. An assumption is deduced here in order to reduce the complexity of the investigation.

As the zeolite syntheses only deals with a group of primary building blocks as described by Pelster and Knight [13, 18, 19], those species which are of importance to the zeolite syntheses are considered for further analysis. The works of Pelster and Knight are taken here as a stepping stone to identify these respective species [13, 18, 19].

The work of Pelster identifies the mass-charge ratio and recommends some structures [13]. In this work, the structures consistent to both the works of Pelster and Knight (for identical mass-charge ratio) are chosen. The species identified are taken for calculation of reaction energies and entropies via quantum chemical methods as seen in section 4.1.

The energies of reaction will then provide the information of whether the reaction is favourable. For each sample two sets of measurements are run, in which the second measurement has a 5 minute time delay.

The first run shows obvious higher molar fractions for monosilicic acid for pH=7, 12 and 13. Prior to injection of the solution into the spraying chamber, the solution was diluted with methanol. This reduces the hydrolysis rate and increases the rate of condensation, consistent to figures 4-9, 4-10 and 4-11 of all pH and temperatures between the first and second runs.
In order to have low effect of the methanol addition to the sample solution, the first measurement is taken as the representative sample solution. The effect of esterification of silicic acid by methanol was assumed to be negligible. The equilibrium esterification requires some time period in order to have significant effect to the silicic acid equilibria ([37]-p.61).

Generally, the amount of monosilicic ($Si(OH)_4$) acid is abundant in all figures 4-9, 4-10 and 4-11 compared to other silicic acid species. This is consistently observed by Iler ([37]-p.124 and 126). Hence, the determination of $K_{p,total}$ with respect to all silicic acid species followed by taking an activity of $Si(OH)_4$ of unity.

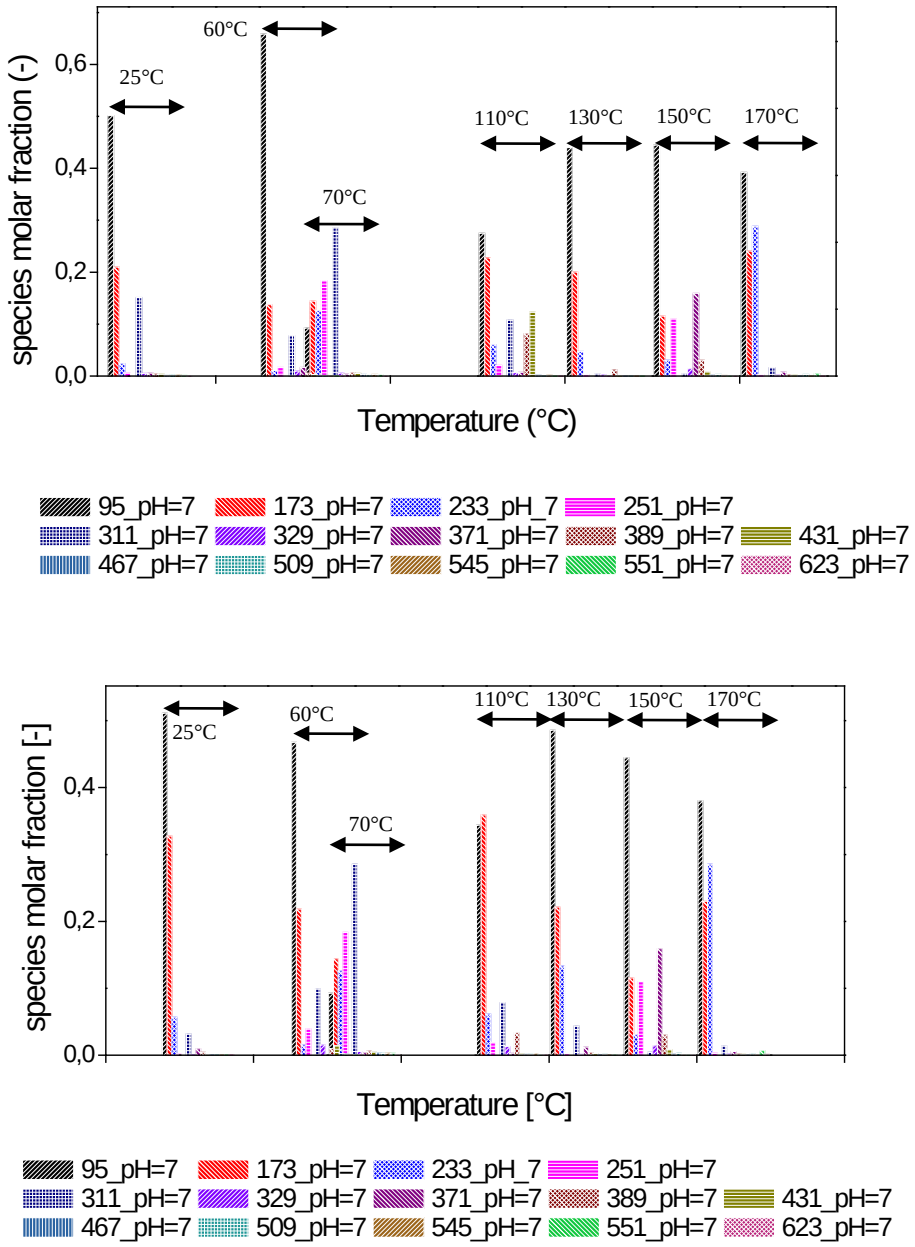

Figure 4-9 – The species molar fractions of the silicic acid species considered (molar mass given beside shade representation below) for the first (figure above) and second run (figure below) at pH=7

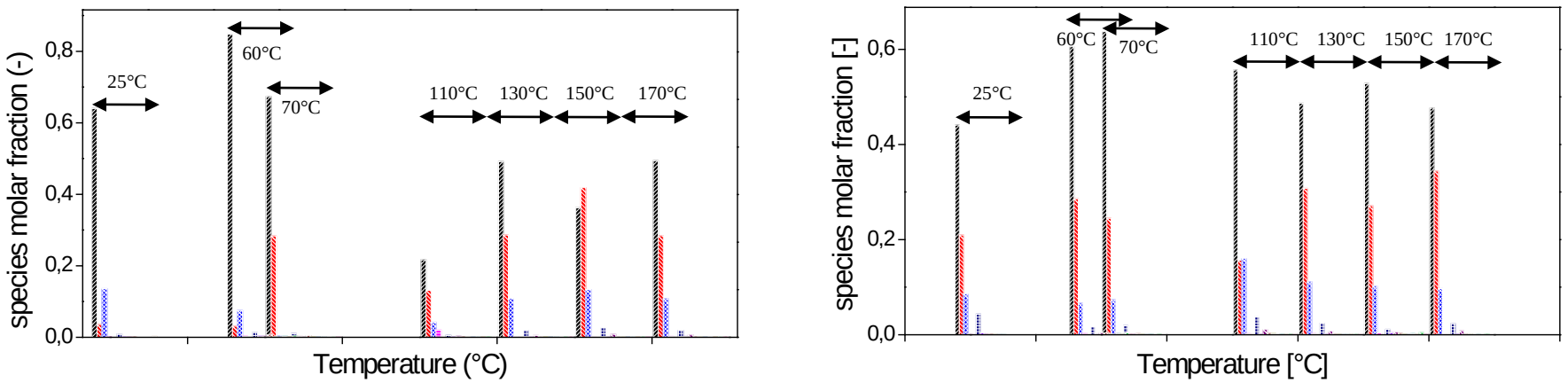

Figure 4-10 – The species molar fractions of the silicic acid species considered (molar mass given beside shade representation below) for the first and second runs at pH=12.

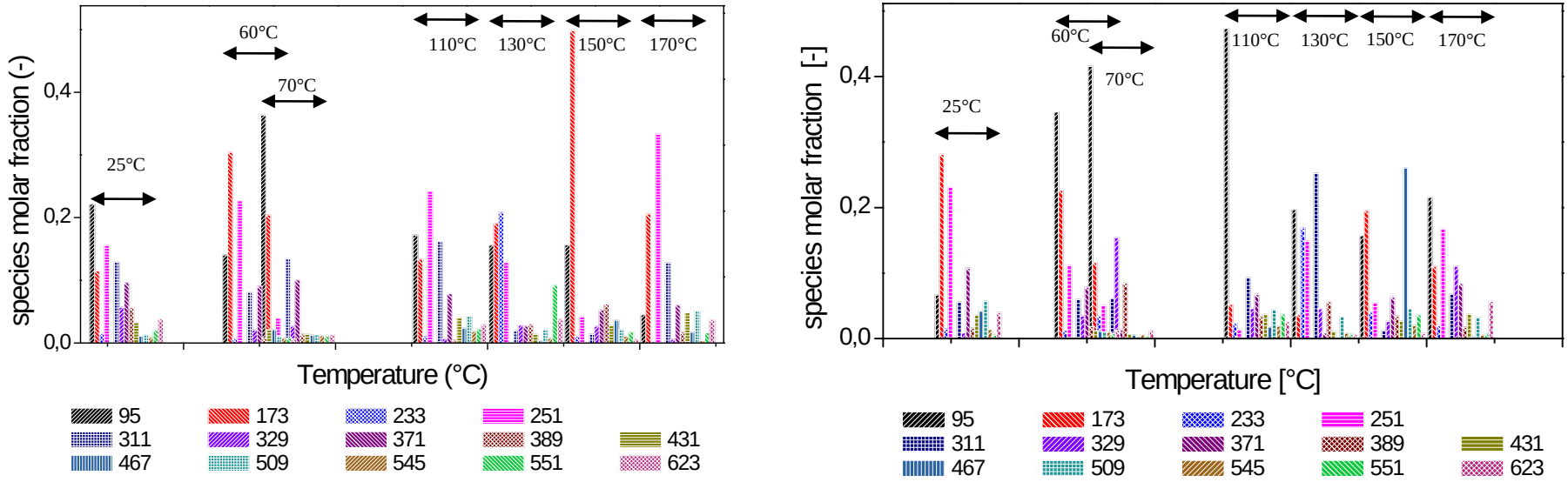

Figure 4-11 – The species molar fractions of the silicic acid species considered (molar mass given beside shade representation) for the first and second runs at pH=13.

The total equilibrium constant ($K_{p,total}$) can be calculated as follows from ESI-MS data:

$$K_{p,total} = \prod_{i}^{N} K_{p,i}$$ Equation 4-2

It is possible to determine the molar concentration from the ESI-MS spectra of the solutions in equilibrium at all temperatures and pH (hydrothermal conditions).

$$x_{counts,Si,i} = \frac{counts_{Si,i}}{Total\ counts}$$ Equation 4-3

$$x_{Si,i} = \frac{\frac{counts_{Si,i}}{N_{Avogadro}}}{\frac{\sum_{i=1}^{N} counts_i}{N_{Avogadro}}} = \frac{[n_{Si,i}]}{[n_T]}$$ Equation 4-4

The molar fractions are related to the equilibrium constant via equation 3-18. The activities are equal to the molar concentrations (activity coefficient of unity) and are related to the total concentration. The assumption made here is that the magnitude of dissociation for all species is equal.

It is reasonable to assume this at such low dissociation constants ([37]-p.123) and due to the unavailability of dissociation constants of higher species (e.g. octasilicic acid). Results of quantum chemical investigations made in this work also show low dissociation constants. Hence, the dissociation is assumed to be in similar magnitude for all species.

The equilibrium constants are plotted and given to fit according to an exponential function, as it is the optimal fitting curve for solubility equilibrium constants, considering the trend given by the van't Hoff equation. The assumptions made for the thermodynamic evaluation of ESI-MS results are:

- The description of analyte-solvent interaction in the chamber according to the Charge Residue Model and Ion Evaporation Model is valid, hence no fragmentation occur

- The counts are related to the molar fraction of the respective species upon consideration of the Avogadro Number
- The voltage applied (3kV between poles and 24kV at the tip of the detector) is under the limit of fragmentation
- The activity of the respective species is exactly the concentration of the species, assuming an activity coefficient of unity
- The ionic species equally dissociates from its respective neutral species, assuming the energy for dissociation for all species is equal (see quantum chemical calculations showing similar energies of dissociation with solvent effects).

The natural logarithmic equilibrium constants of equation 4-2 with the dependence of the reciprocal temperature are given in figure 4-12.

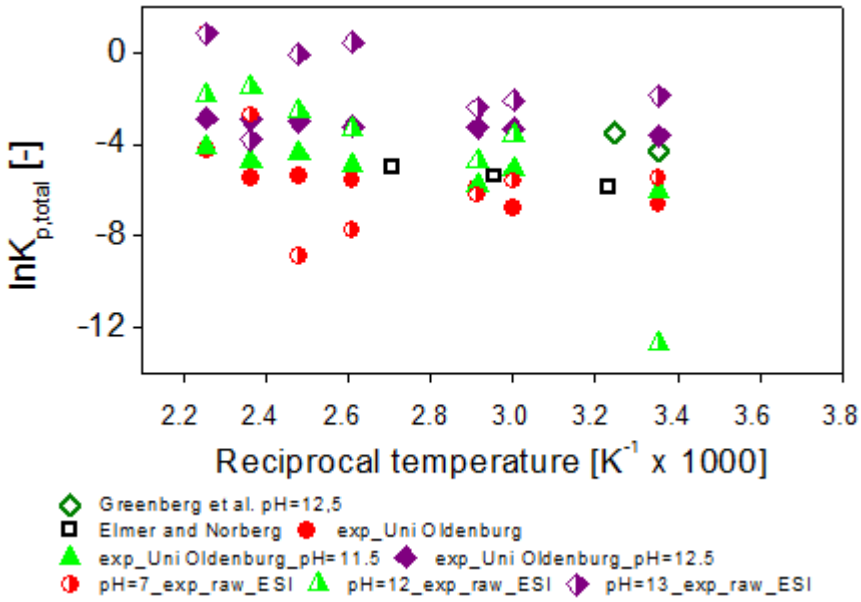

Figure 4-12 -– The comparison of the logarithmic total equilibrium constants from UV-Vis (filled symbols) and ESI-MS measurements (half-filled symbols).

The figure 4-12 above show some deviation of the equilibrium constants derived from ESI-MS measurements with respect to UV-Vis results. Especially, the ESI-MS values for all pH values are higher than that measured by the UV-Vis method. This may be due to the incomplete reaction of all silicic acid species in the UV-Vis measurement. This may be a cause although Iler [37]-(p.96 and p.196) mentioned that a period of 30 minutes is sufficient for reaction of all silicic acid species with ammonium heptamolybdate. Furthermore, the ESI-MS values for pH=7 have large deviations. Probable causes are:

- The ex-situ measurement of the solubility experiment
- Inconsideration of neutral species in the ESI-MS chamber, as they are not charged
- Further causes maybe fragmentation of the silicic acid species, although this is unlikely [114] and
- The esterification of the respective silicic acid species.

The potential between the two poles are also of great importance as the attraction at a constant potential give different detection intensities with respect to the different masses of the charged ions.

However, this is compensated by an additional potential at the tip of the receiving end, to ensure full arrival of the charged ions. However, the figure above shows that the equilibrium constants from the ESI-MS measurements do not coincide with consistent literature UV-Vis measurements.

For further analysis of this disagreement, individual species have to be taken into account and a model consistent to literary information, both experimental and theory based, has to be developed. This is done to achieve results consistent to literature data known to date. It is also done to compare its deviation with measured values in this work based on the determination of equilibrium values.

$$\ln K^{o}_{reaction} = -\frac{\Delta g^{o}}{RT} \qquad \text{Equation 4-5}$$

$$\ln K_{reaction} = \ln K^{o}_{reaction} - \frac{\Delta h^{o}}{R}\left(\frac{1}{T} - \frac{1}{T^{o}}\right) \qquad \text{Equation 4-6}$$

$$\ln K_{reaction} = -\frac{\Delta g^{o}}{RT} - \frac{\Delta h^{o}}{R}\left(\frac{1}{T} - \frac{1}{T^{o}}\right) \qquad \text{Equation 4-7}$$

The equilibrium constant found are according the condensation and cyclisation reactions.

$$FIT_i = \bar{a} \times exp\ \frac{\bar{b}}{T} \qquad \text{Equation 4-8}$$

The fit of all species considered are graphically shown as follows and the values of the fitting equation 4-8 are shown in the Appendix 7.5:

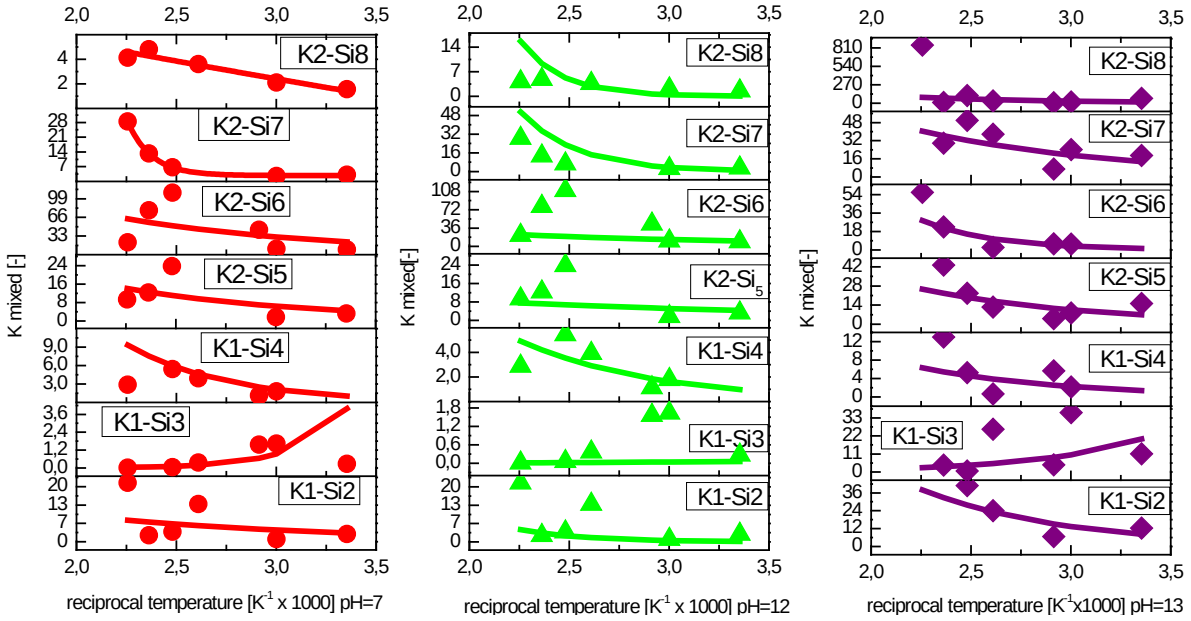

Figure 4-13 – Fitting data prior to the subject of the equilibrium model of figure 3-5 for mixed species.

From figure 4-13, the individual equilibrium constants for mixed species are depicted. The values have a contrary temperature dependency as observed from quantum chemical calculations (see figure 4-2). The equilibrium constants increase with higher temperature for ESI-MS measurements, whereas it decreases for quantum chemical measurements. The only consistency is seen for the reaction to trisilicic acid K1-$_{Si3}$. The cause for these contradictions is unclear. However, the quantum chemically calculated equilibrium values are positive and the equilibrium is on the product side and this is also observed in figure 4-13 above.

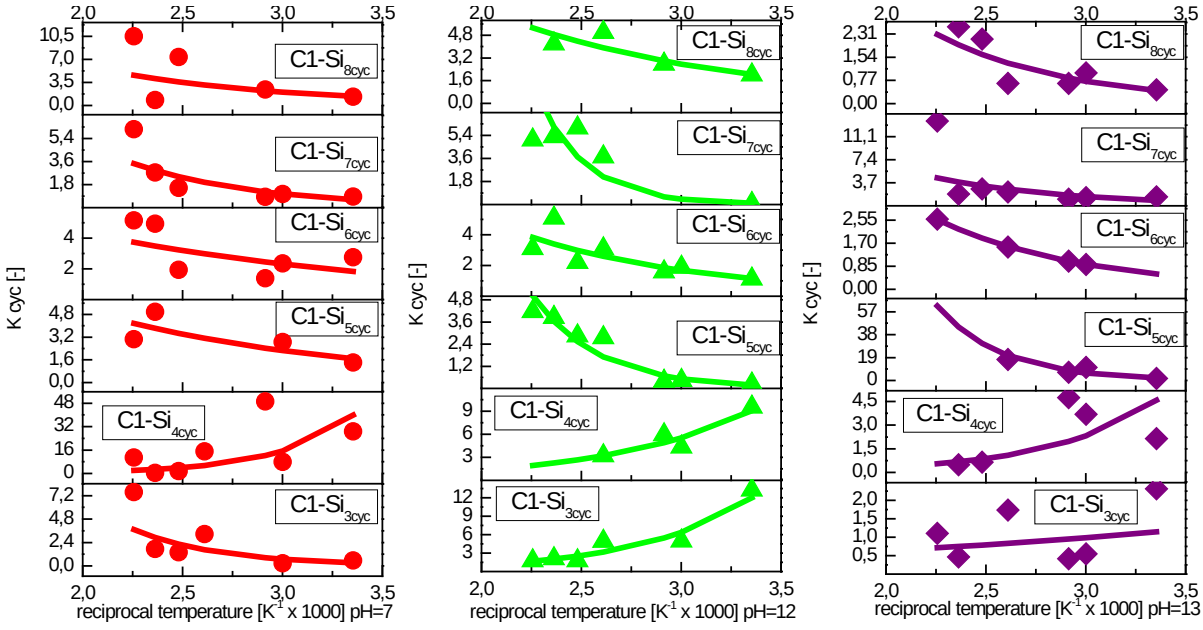

Figure 4-14 – Fitting data prior to the subject of the equilibrium model of figure 3-5 for cyclic species.

In figure 4-14, the equilibrium constants for all cyclic (simple and fused-see page 22 of this work) species are shown. The equilibrium constants increase with higher temperature except for C1-$_{Si3cyc}$ and C1-$_{Si4cyc}$. These two reaction mechanisms contradict with quantum chemical calculations (see figure 4-1). This may be due to occurrence of a different reaction mechanism. However, in this investigation, the fitting data is still taken for equilibrium calculations as the experimental results describe the actual system.

Nevertheless, there are some deviations occurring in the measured data as well. The equilibrium constants for the cyclic (simple and fused-see page 22) reaction all lie in the positive region. This is not the case for C1-$_{Si5cyc}$, C1-$_{Si6cyc}$ and C1-$_{Si7cyc}$ in quantum chemical calculations (see figure 4-1). This may be due to other reaction mechanisms occurring for cyclopentasilicic, cyclohexasilicic and cycloheptasilicic acid. Some equilibrium constant are extremely large, such as the K_{cyc}-value of C1-$_{Si5cyc}$ at pH=13. This may be due to erroneous measurements.

The fitting however has good agreement to the experimental values for all species and pH values. There would be no physical significance attached to the fitting, if they are not coupled in equilibrium. In order to check the fitting data for consistency, the fitting parameters (corresponding to the equilibrium constants) are implemented to the equilibrium model in figure 3-5 by the relaxation method. Figure 3-5 includes the considerations of all literature data and quantum chemical considerations of equilibrium reactions investigated in this work (see section 4.1).

This fitted data are inserted in the model in order to fit the equilibrium constant to the best possible combination, which is consistent to literature and quantum chemical data. The parameter $\bar{a}$ of the fit equilibrium constants is changed qualitatively with comparison to quantum chemical results and literature data to run the simulation without contradicting to the setup of the equilibrium reaction model (see Appendix 7.5).

It must be emphasized here again that the fitting parameter $\bar{a}$ has been changed here according to literature and quantum chemical explanations. A more systematic way would be to change the equilibrium constant for each reaction upon detection of divergence of the simulation model. However, this would only cause the model to converge to a local minimum of the many minima available.

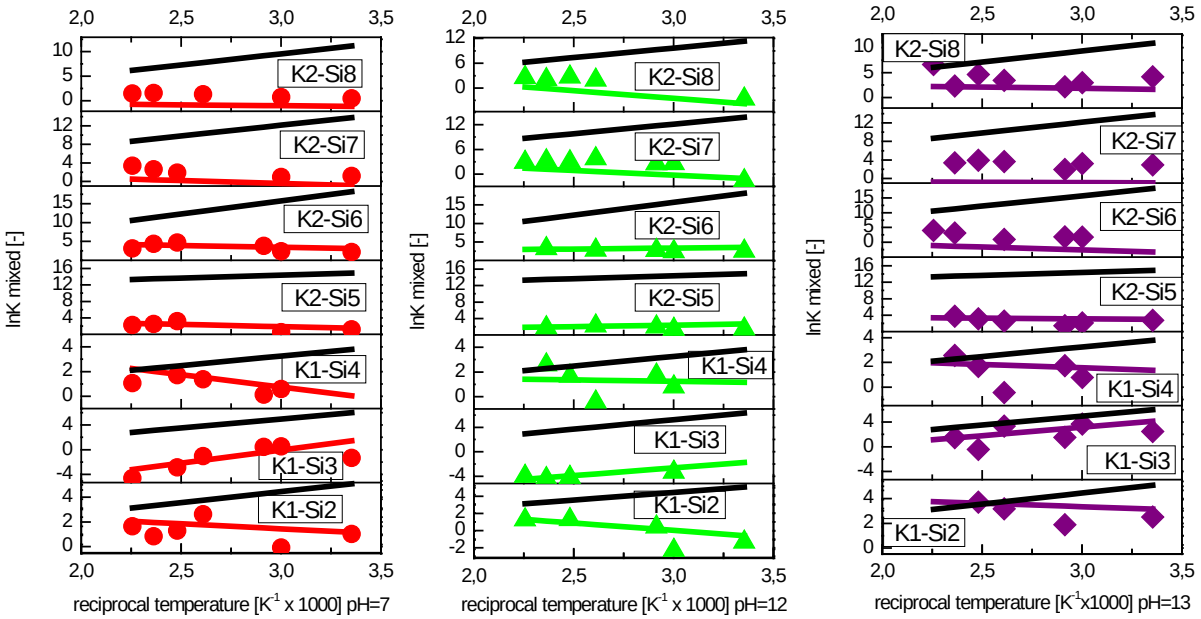

Figure 4-15 – Fitting data after equilibrium calculation from the model of figure 3-5 for mixed (linear and branched-cyclic) species.

pH=7-model ; pH=12-model ; pH=13-model ; quantum chemistry (B3LYP)

pH=7-ESI-MS ; pH=12-ESI-MS ; pH=13-ESI-MS.

From figure 4-15, the logarithmic equilibrium constants for mixed species retrieved from experiments (symbols), equilibrium calculations (solid coloured lines) and quantum chemical calculations (black line) are depicted.

Most logarithmic equilibrium constants, which were retrieved from equilibrium measurements, have good agreement with experimental data. Some exceptions are for K2-$_{Si6}$ for pH 13, and K2-$_{Si7}$ and K2-$_{Si8}$ at pH=7 and 12.

However, there exist some deviation of experimental and quantum chemical data for all species. Furthermore, the calculated and experimental data have contrary temperature dependencies compared to quantum chemical calculations, as observed in 4-13. The only exception is for P1-Si_3. More investigation is required to access the inconsistencies.

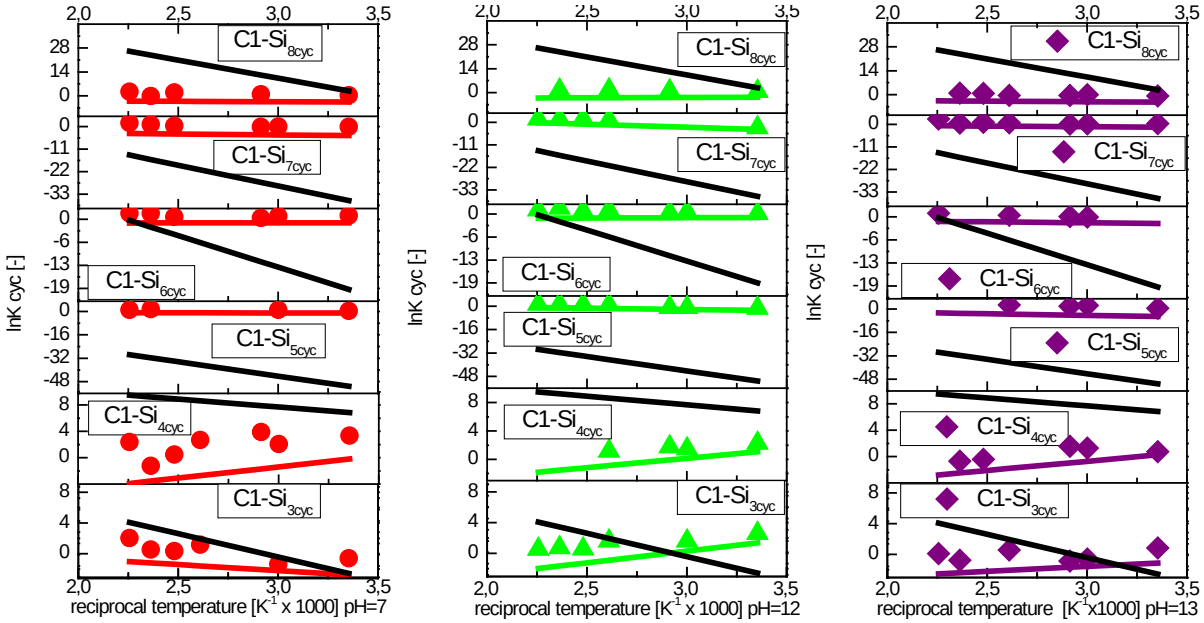

Figure 4-16 – Fitting data after equilibrium calculation from the model of figure 3-5 for cyclic species.

pH=7-model ; pH=12-model ; pH=13-model ; quantum chemistry (B3LYP)

pH=7-ESI-MS; pH=12-ESI-MS; pH=13-ESI-MS.

In figure 4-16, the logarithmic equilibrium constants for all cyclic species (simple and fused- see page 22 of this work) retrieved from experiments (symbols), equilibrium calculations (solid coloured lines) and quantum chemical calculations (black line) are depicted.

Some deviations between the experimental data and the data retrieved from equilibrium calculation exist due to improvement of the parameter $\bar{a}$. This is done to ensure convergence of the equilibrium model. Highest deviations are observed for C1-Si_{3cyc} and C1-Si_{4cyc} for all pH values. The values of the equilibrium calculations are lower than experimental data. Slight reduction of the logarithmic equilibrium constants are observed for C1-Si_{6cyc}, C1-Si_{7cyc} and C1-Si_{8cyc} for all pH values. A further reduction of the parameter $\bar{a}$ was necessary for C1-Si_{5cyc} for pH=13. These reductions are necessary to avoid divergence of the equilibrium model depicted in figure 3-5. Although convergence is achieved, this achievement may only lead to a solution, which is a local minimum.

Large deviations are observed between the experimental data and quantum chemically retrieved values of the logarithmic equilibrium constant. For C1-Si_{3cyc} and C1-Si_{4cyc}, even the slope of the quantum chemical values is in contradiction with the experimental values for pH=12 and 13. More investigation is required to access the inconsistencies.

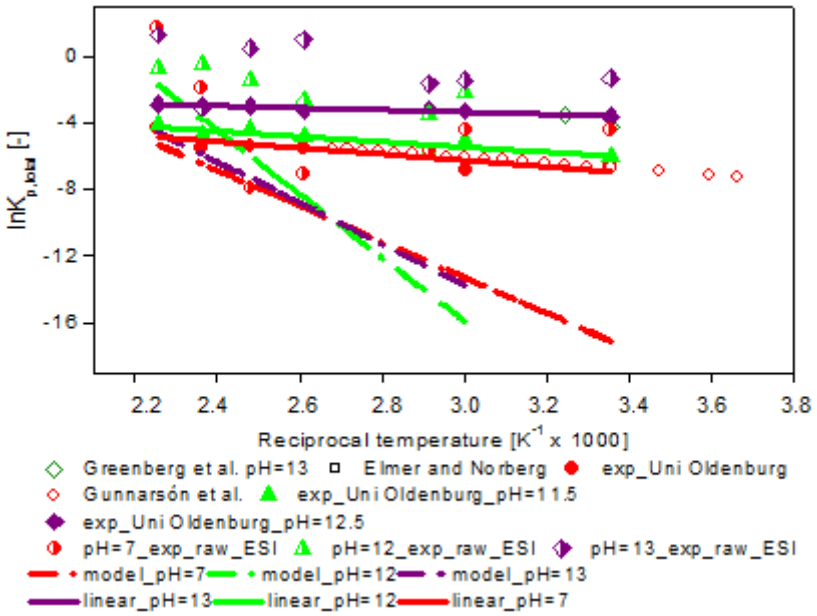

Figure 4-17 – All logarithmic equilibrium constants for UV-Vis measurements, ESI-MS measurements and calculated values

Figure 4-17 shows the equilibrium constants after subjected to the equilibrium reaction model. The values of the equilibrium constant dropped significantly (dashed lines). This is mainly due to the reduction of the equilibrium constant of the cyclic species.

The equilibrium constant for the cyclic species was too high to run the equilibrium model appropriately and hence was reduced. The reduction caused marked reduction in the total equilibrium constant. This shows that cyclisation processes are generally not favoured as mentioned by means of theoretical calculations by McIntosh [74, 75].

4.2.1.2 Results from electrochemical measurements – potentiometry

4.2.1.2.1 Setup of experimental apparatus

Potentiometric cell [**PC**]

Electrolyte Solution [**ES**] – 1x 10^{-3}M KNO_3 was dissolved in distilled water. This solution serves as an electrolyte for the cell in all compartments ([**AT]-anodic terminal**, [**CT]-cathodic terminal**, liquid junction [**LJ**]) to avoid concentration gradients.

A nitrate salt was chosen to mobilise the silicic acid species in the solution but only a low concentration was added in order to avoid an equilibrium shift of the solution ([73]-p.57-59).

Electrolytes have no significant effect on the equilibrium concentration of silicic acid ([37]-p.44).

- Sample solution [**SS**] – Amorphous silica (heated at 105°C for 24 hrs, calcined at 550°C for 24 hrs and stored in a desiccator filled with molecular sieves) is located in a separate reactor. The electrolyte solution is pumped from the **PC** to the reactor in order to slowly initiate the silica dissolution. Measurement is started immediately upon H_2-injection into the **PC**.

- Working electrode solution [**WS**] – The **ES** is also circulated from the **PC** from one of the terminals to a separate reactor to achieve same conditions at both terminals (**AT** and **CT**).

- Liquid junction [**LJ**] – Both electrode terminals are separated by a liquid junction [**LJ**] filled with **ES** and non-selective porous Teflon frits from *Berghof*®.

- Pumps – Vibration-free micro gear pumps from *Diener*® are used to circulate the solution from each terminal to the reactor.

- Stirrer – The reactor with the sample solution is stirred with a magnetically coupled precision stirrer from *Buchiglasüster*® rotating at 70 revolutions per minute (rpm).

- Platinum electrodes – Platinum electrodes with 99.999% purity from *Goodfellow*® were used with dimensions of 1mm in diameter and 150mm in length.

Heating – The reactor with **WS** and the **PC** are electrically heated. K-type thermocouples were used for both compartments connected to an in-house controller for temperature measurement and regulation. The reactor with the **SS** is oil-heated with a temperature regulating LAUDA thermostat circulating through the outer jacket of the reactor with an integrated pump. Temperature variations in all compartments were at a maximum of ±0.5K at all temperatures. All threads for screw fittings were taped with Teflon tapes to prevent leakages and short circuits. The design of the cell is shown in the following figure 4-18 and a simplified setup of the apparatus is shown in the figure 4-19.

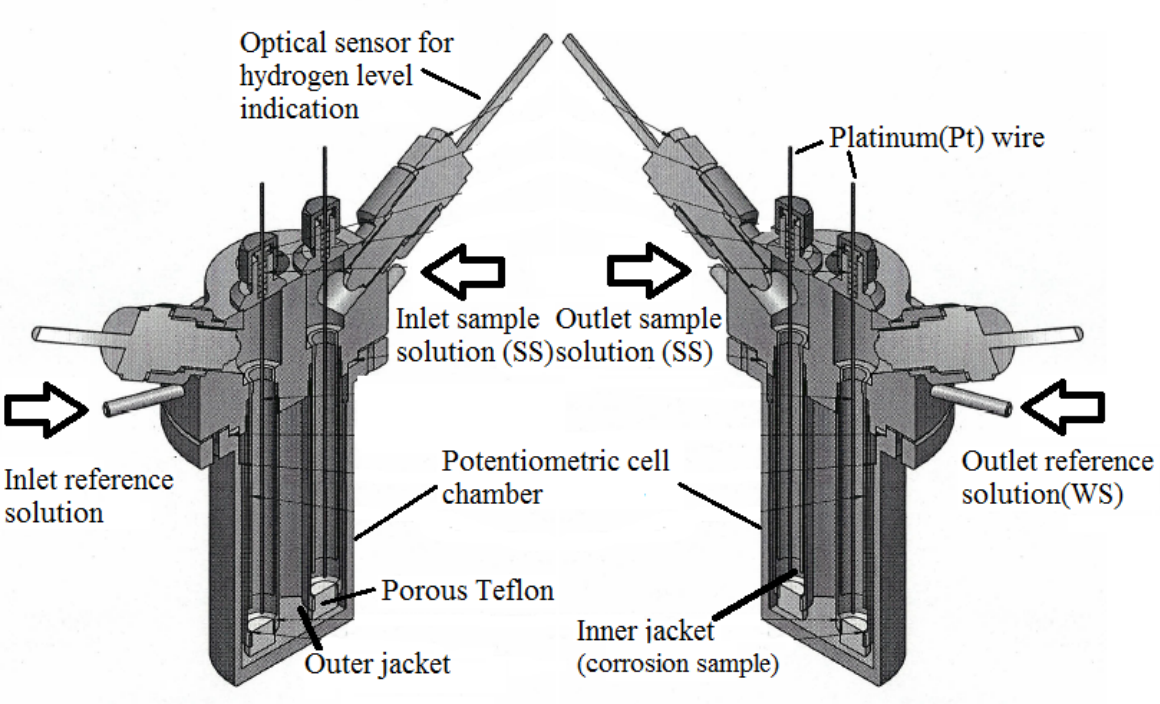

Figure 4-18 – The design of the high temperature electrochemical cell.

The figure 4-18 shows design of the flow-through electrochemical cell. The cell contains two half-cells separated by non-selective porous Teflon frits. The half-cell is separated by the potentiometric cell chamber with electrolyte solution, serving as a liquid junction **[LJ]**. Each half-cell consists of an inner and outer-jacket. Depending on the half-cell of concern, sample **[SS]** or reference solution **[WS]** flows through the outer-jacket into the inner-jacket to ensure total contact with the Pt-wire. The solution exits the half-cell of concern into a separate reactor, where sample and reference solution are stored. The solution circulates from the reactor to the cell with a micro gear pump.

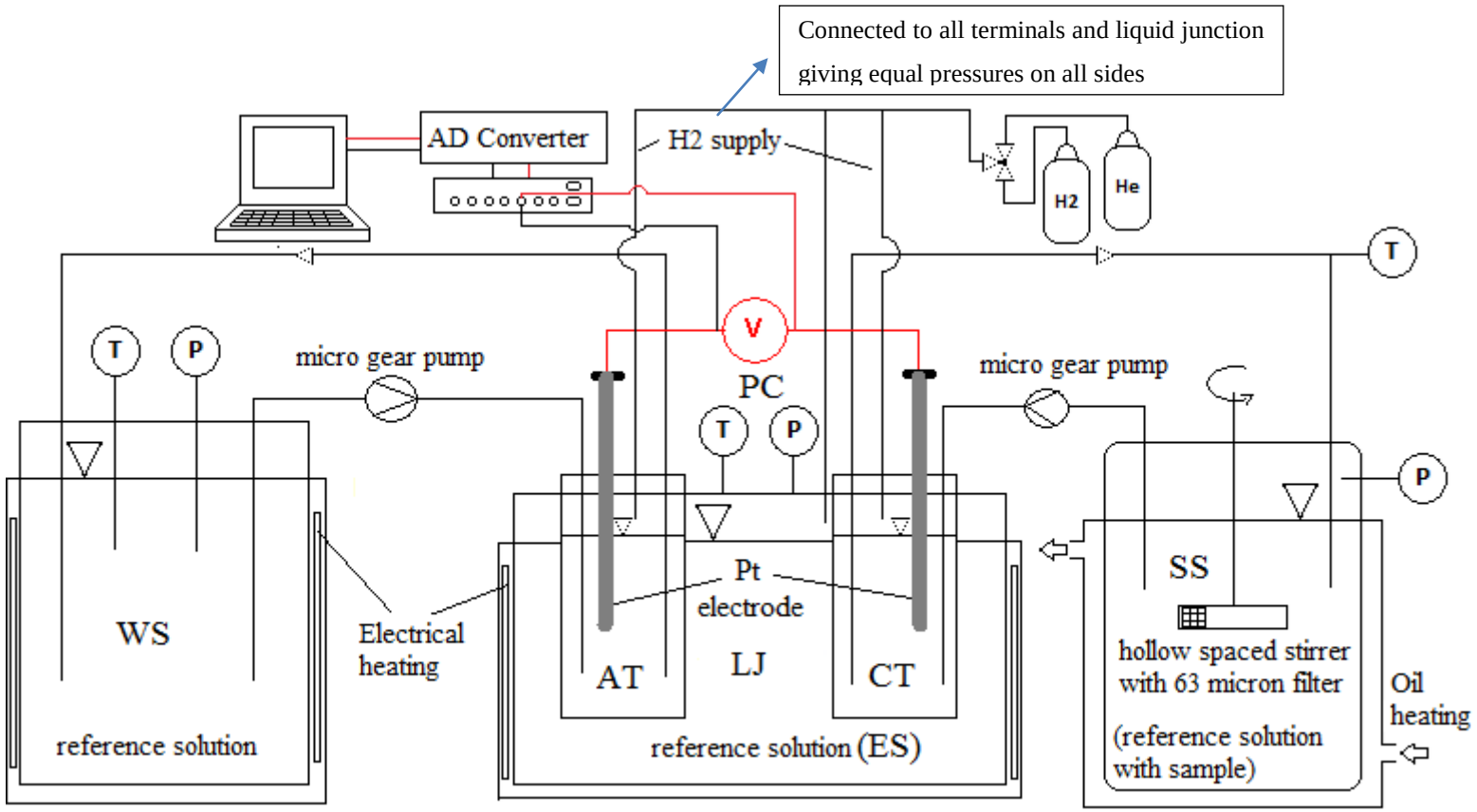

Figure 4-19 – The simplified schematic diagram of the apparatus used for the determination of the silicic acid dissociation constant.

4.2.1.2.2 The streaming potential

The streaming potential has to be taken into account, due to the claim of Lvov et al. that it effects the total potential [96]. The streaming potential was determined by just running the measurement without silica precursors from zero flow rate (0) condition to half of the maximum capacity (0.5) of the vibration free pumps.

The streaming potentials at higher temperatures are of great significance, as a vapour-liquid mixture phase exists along the electrodes. This can be observed clearly with the abrupt decrease in the voltage above 100°C (see figure 4-20).

This may correspond to the existence of vapour phase, where it has a much lower conductivity. In order to measure the liquid phase, the existence of a liquid layer on the electrode has to be guaranteed at all times. The circulation of the liquid is hence required to deliver the existing liquid phase of the reactor containing sample solution [SS] to the electrochemical cell. It also must be kept stirring to reduce liquid junction potentials at all times. Any form of concentration diffusion, is tested through the potential measurement, with a constant flow rate and without silica source at different alkalinity.

4.2.1.2.3 Calibration measurements

The measurements are done with the absence of silica at constant temperature and different volume flows and respective velocities (0.0 m^3/s at 0% of max.rpm [0], $1.93x10^{-5}$ m^3/s at 25% of max.rpm [0.25], $3.86x10^{-5}$ m^3/s at 50% of max.rpm [0.5]). At a new temperature, a new fresh solution from the reactor is filled upon temperature reduction to room temperature and set to a new temperature. A new batch of H_2 gas is supplied into all compartments (**PC, AT, CT, LJ**).

H_2 gas is chosen to have a good adsorption property on the platinum surface and the dissociated H^+ reacts readily with deprotonated silicic acid anions. Hence, the dissociation constant of silicic acid is determined from the amount of hydrogen ions at the platinum electrode related to the dissociated silicic acid. Measurements are done for temperatures ranging from 25°C to 170°C.

4.2.1.2.4 Measurements with silica source (dried at 105°C (24h) and calcined at 550°C (24h) LUDOX AS-40)

The silica source is added into the hollow-spaced stirrer with a mesh width of 63microns. This ensures that particles are large in surface area so that particle size does not hinder the kinetics of the dissolution reaction ([37]-p.49). Furthermore, the gear type pumps are then certainly not eroded due to the large particle sizes.

Before setting the temperature, the H_2 gas is supplied to all compartments (**PC, LJ, AT, CT**). The pumps are started on both terminals simultaneously for circulation to reduce streaming potentials. Heating is controlled to avoid pressure differences on both terminals and avoid short-circuits between the liquid junction.

Design considerations of the custom made electrochemical (potentiometric) cell and that of Busey and Mesmer [42] and Yang [80] and Lvov et al.[96, 115, 116] is shown in table 4-7.

Table 4-7 – The comparison between different flow through electrochemical cell designs and the cell from this work (last column) is shown in the table below.

Design parameters	Busey and Mesmer(1977) [42]	Yang *et al.* (2003) [80]	Lvov *et al.* (1997) [96]	Uni Oldenburg (2014)
High pressure/temperature	✔	✔	✔	✔
Flow-through	x(static cell)	x(static cell)	✔	✔
Measurement of silicic acid	✔	✔	x	✔
No Sample Dosage required	x	x	✔	✔
No Dosage required for pH regulation (addition of HCl or NaOH) – correction of drift potential	x	x	✔	✔
Separate buffer reactors for storage of sample solution	✔	✔	✔	✔
Separate buffer reactors for storage of reference solution	x	x	✔	✔
Deposits of iron oxide	x	x	x	✔

A flow-through cell is needed to improve the mixing effect and hence flow or stirring conditions are introduced. There should be enough silicic acid ions at the phase boundary for a limited time to ensure reaction with H^+, which undergoes charge transfer at the Pt-surface. It is also to prove that Busey and Mesmer's value are consistent even at flow conditions [42].

The cell according to Busey and Mesmer has a magnetic stirrer which induces forced convective effects [42]. It is not known whether the convective flux from stirring effects was taken into account. According to Lvov [96], treatment of the forced convective flux to refine the potential (ΔE) of the electrochemical cell is essential. It is nevertheless necessary to make calibration measurements, which may remove all deviations in the absence of silicic acid species.

It can be calculated via relations from chemical engineering, in which the over-potential can be removed to get a refined potential (ΔE). The resulting limiting current established at different flow rates can be compared with the limiting current relation of Nernst and Meriam [95]. The limiting current relation to the diffusion coefficient and the boundary layer thickness is obtained by means of dimensionless numbers such as the Reynolds, Schmidt, Péclet and Sherwood numbers [117-119].

However, no significant difference in potential (ΔE) was observed with variation of the volume flow (figure 4-20-next page). Under close observation, corrosion and iron oxide (rust) was found in the half-cell compartments (**[AT]** and **[CT]**).

4.2.1.2.5 Results of potentiometry

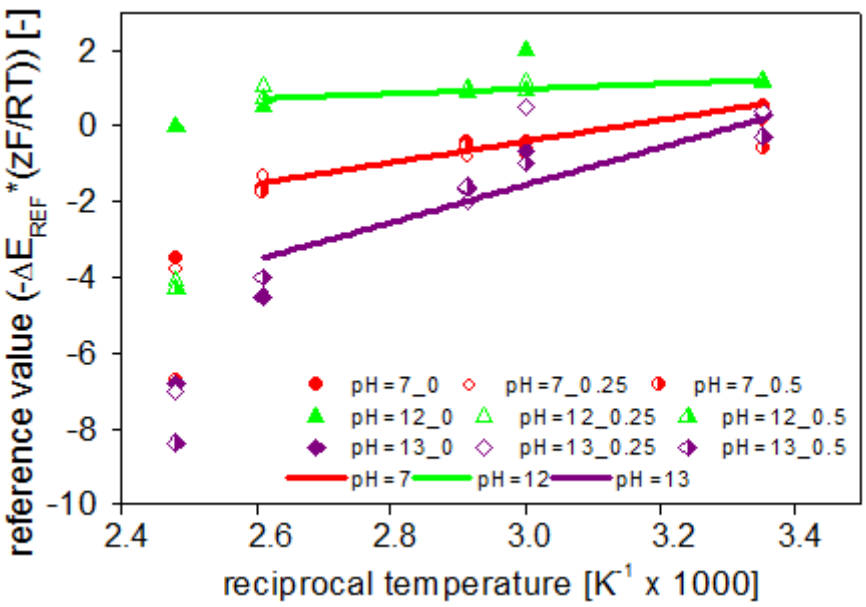

Figure 4-20 – The potential of the electrochemical cell at different pH-values represented by different colours and varying velocities (0, 0.25 and 0.5) of pumping solutions on both half-cells (represented by different symbols).

From figure 4-20, the dissociation constant are depicted with respect to different temperatures and pH-values (pH=7, 12 and 13) at varying flow velocities. This is determined from equation 3-70 (the subscripts of equation 4-9 and 4-10 are clarified in page 37). There are two possibilities for the description of the dissociation constant. It can be reference values in the presence (Fe, 1/Fe, 2) or in the absence (1/2) of corrosion of half-cell 1 related to half-cell 2:

$$\Delta E_{C,REF} = -\left[\frac{RT}{zF}\ln\left(\frac{\left[H^+\right]_{Fe,1}}{\left[H^+\right]_{Fe,2}}\right)\right]_C$$

$$\Delta E_{C,REF} = \left[\frac{RT}{zF}\ln\left(\frac{\left[H^+\right]_1^2}{\left[H^+\right]_2^2}\right)\right]_C$$

$$\Delta E_{REF} \times \frac{-zF}{RT} = \ln\left[H^+\right]_{Fe,1/Fe,2} \qquad \text{Equation 4-9}$$

$$\Delta E_{REF} \times \frac{-zF}{RT} = \ln\left[H^+\right]_{1/2}^2 \qquad \text{Equation 4-10}$$

The natural logarithm of the equation is divided by 2.303 to retrieve the base 10 logarithm. According to equation 4-10, the square ratio of proton concentration ranges from zero to -1 for pH=7 and zero to -2 for pH=13. This would mean that the proton concentration ratio varies from 0 to $0.32x10^{-1}$ for pH=7 and zero to 10^{-1} for pH=13. The proton concentration should not vary in such high magnitudes for a normal hydrogen electrode. Another phenomenon has to occur for such large proton concentration differences to occur.

In the presence of corrosion, equation 4-9 is used. The equation directly relates the proton concentration in both cells and not its squared ratio as in equation 4-10. In this case, the proton concentration ratio varies from zero to -1 for pH=7 and zero to -2 for pH=13. This would mean that the proton concentration difference in both half-cells vary from zero to 10^{-1} for pH=7 and zero to 10^{-2} for pH=13.

The corrosion tends to create a passive layer on the stainless steel surface. In such a case, hydrogen cannot react on the surface of the stainless steel. Hence, the detection of proton concentration is reduced. Therefore, the reduction in proton concentration is an indication of passive layer formation. According to the Pourbaix diagram, the passive layer is formed above pH=7, which is the pH of half-cell 2. Hence if the proton concentration ratio is lower than zero, iron oxide formation is indicated. The best example is shown for pH=13 at the highest temperature of 130°C (reciprocal temperature 2.5).

The base 10 logarithm proton concentration ratio is -2, which means the proton concentration between the half-cell 1 (pH=13) is two orders of magnitude lower than of half-cell 2 (pH=7). Hence, the lower concentration of H^+ in half-cell 1 indicates the existence of corrosion and the deposition of the iron oxide layer at this condition (see Pourbaix Diagram in Appendix 7.2.2 above pH=7).

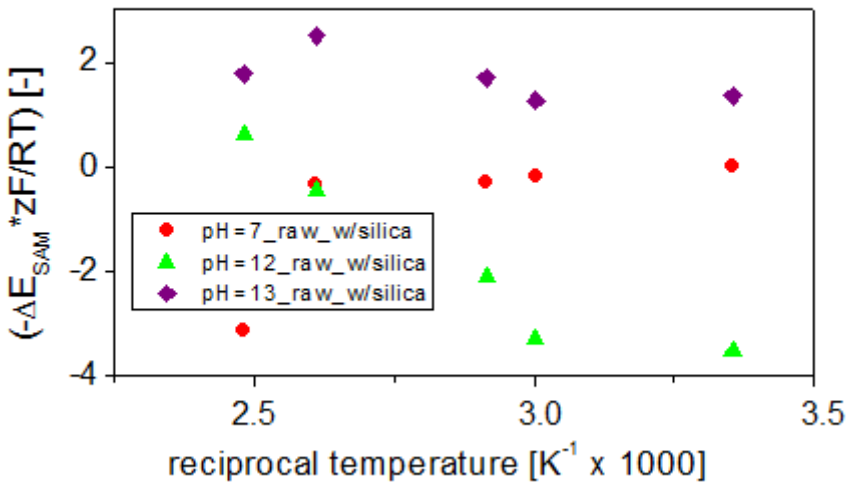

Figure 4-21 – The actual measurement of the potential with dissolved silica in the sample solutions at different pH values is presented.

Figure 4-21 shows the dissociation equilibria of the sample solution with silica determined in identical fashion from equation 3-70 (subscripts of equation 4-11 and 4-12 are clarified in page 37). The sample potential may be in the presence (Fe, 1, $Si(OH)_4$/Fe,2) or absence (1, $Si(OH)_4$/2) of corrosion in half-cell 1 related to half-cell 2:

$$\Delta E_{SAM} \times \frac{-zF}{RT} = \ln\left[H^+\right]_{Fe,1,Si(OH)_4/Fe,2} \qquad \text{Equation 4-11}$$

$$\Delta E_{SAM} \times \frac{-zF}{RT} = \ln\left[H^+\right]^2_{1,Si(OH)_4/2} \qquad \text{Equation 4-12}$$

The natural logarithm of the equation is divided by 2.303 to retrieve the base 10 logarithm.
It can be seen from figure 4-21 that the raw data for pH=12 does not correspond to the trend at pH=7 and pH=13. This value is hence not taken into account. However a linear dependency between pH=7 and pH=13 with respect to the temperature according to the Nernst relationship (equation 3-26) ([97]-p.219) is taken to show the apparent value of pH=12.

The analysis is done analogous to the previous figure 4-20. Equation 4-12 is firstly considered for figure 4-21. The values of the squared proton concentration ratio is about zero to -1 for pH=7 from lower to higher temperatures. This would mean that there is nearly no difference in proton concentration between half-cell 1 and 2. This may correspond to a normal hydrogen

electrode. However, at pH=13 the squared proton concentration ratio varies from 0.5 to 1 at lower to higher temperatures.

This would mean that the proton concentration in half-cell 1 is about 1.75 to 3 times higher than in half-cell 2. This cannot be the case if the proton concentration in half-cell 2 is unity, which corresponds to a normal hydrogen electrode.

Hence, the proton concentration in half-cell 2 has to be lower. It should be at least 1.75 to 3 times lower than unity, in order to have feasible proton concentration in half-cell 2. In the case of pH =13 at 130°C (reciprocal temperature 2.5). The proton concentration in half-cell 2 could be at the other extreme 10^{-7}, being the pH of the solution in half-cell 2. The formation of the passive layer is initialised at this pH (see Pourbaix Diagram Appendix 7.2.2). Hence, the proton concentration is about 3×10^{-7} in half-cell 1. This nearly leads to the dissociation constant of silica reported by Busey et al of about 10^{-10} at the given pH and temperature.

However, such a value can only be detected in the presence of corrosion in half-cell 2. The consideration if equation 4-11 is hence necessary. The values are now simply the proton concentration ratio of half-cell 1 and half-cell 2. This is about zero to -1 for pH=7 from lower to higher temperatures and 0.5 to 1 for pH=13 from lower to higher temperatures.

If the values of pH=13 are considered, the corrosion is facilitated without the formation of a passive layer at half-cell 1, as the proton concentration is higher than of half-cell 2. It is about 3×10^{-7} at lower temperatures and 1×10^{-6} at higher temperatures. The values at all temperatures for pH=13 would correspond to the dissociation value of Busey et al. However, this gives further indication of the propagation of corrosion in half-cell 1 in the presence of silica (see Pourbaix Diagram Appendix 7.2.2 below pH=7).

If figure 4-20 and 4-21 are compared for their proton concentration ratios, the proton concentration in the presence of dissolved silica is higher. This means that the corrosion is facilitated in the presence of silica. This is due to the interaction of silica with iron oxide and iron hydroxides in the aqueous phase on the stainless steel surface and preventing the development of a passive layer.

Proof for this statement is given by subsequent SEM, EDX; Raman and IR-measurements. SEM and EDX measurement show inhomogeneous iron oxide and silicate deposition. Raman measurements show very low intensities of iron oxide layer in the presence of dissolved silica and IR-measurements show Fe-O-Si-linkages.

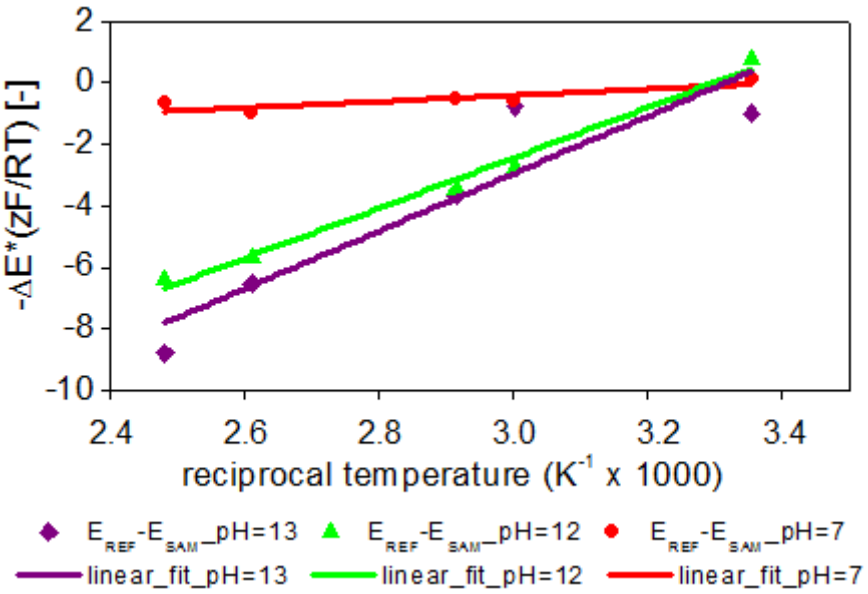

Figure 4-22 – The equilibrium constant after subtraction of the calibration potential for different pH values is shown. The values for pH = 12 is determined via a linear dependency of the potential between pH = 7 and 13.

The figure 4-22 shows the difference in the dissociation constant between figure 4-20 and 4-21. It is the difference of the reference and sample potential in the presence and absence of corrosion shown in figures 4-20 and 4-21. It is simply the ratio of proton concentration in half-cell 1 with and without the silica in the presence (Fe, 1/ Fe, 1, $Si(OH)_4$) and absence (1/ 1, $Si(OH)_4$) of corrosion (subscripts of equation 4-13 and 4-14 are clarified in page 37):

$$\Delta E \times \frac{-zF}{RT} = \ln\left[H^+\right]_{Fe,1/Fe,1,Si(OH)_4} \qquad \text{Equation 4-13}$$

$$\Delta E \times \frac{-zF}{RT} = \ln\left[H^+\right]^2_{1/1,Si(OH)_4} \qquad \text{Equation 4-14}$$

The natural logarithm of the equation is divided by 2.303 to retrieve the base 10 logarithm.
It can be seen from pH = 7 and 13 that the linear Nernst relationship is fulfilled at all temperatures, even after surpassing the vapour pressure of the solution. As the measurements

for pH=12 was erroneous, the linear relation of the pH-value according to the Nernst equation was taken between pH = 7 and 13 to yield proper values for pH=12. However, the experimental values of pH = 12 are not used for further calculations.

The proton concentration in half-cell 2 is probably the same in the absence and presence of silica. The corrosion reaction occurring in both cells has been partially established. Nevertheless, it is appropriate to discuss the complete possibilities here as well.

If equation 4-14 is considered, not much difference in squared proton concentration ratio is observed for pH=7 at all temperatures, varying by -0.5 at 130°C (reciprocal temperature 2.5). This means that the proton concentration is 70% lower without the presence of silica, indicating the reduction of proton concentration and the existence of corrosion with passive layer formation. At pH=13, the proton concentration ratio ranges from zero to -4 from lower to higher temperatures The concentration of the proton is 10^{-2} lower without the presence of silica. Hence, it is also a proof that corrosion in the presence of silica is higher.

If equation 4-13 is taken into account, the proton concentration ratio at pH=7 is 0 to -0.5 from lower to higher temperatures, indicating the lower proton concentration in the absence of silica. At pH=13, the proton concentration ratio ranges from zero to -8, also indicating low proton concentration in the absence of silica. The concentration is 8 orders of magnitude lower at pH=13 and 130°C in the absence of silica (reciprocal temperature 2.5).

4.2.1.3 Proof of corrosion effects

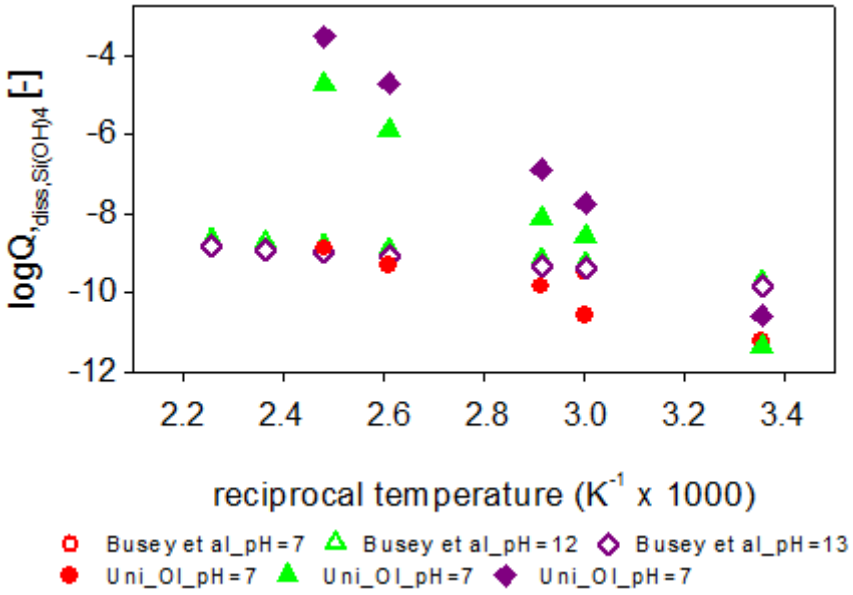

Figure 4-23 – The literature results for the dissociation constant of Busey and Mesmer [42].

It can be deduced from figure 4-23 that the potential measured from electrochemical measurement in this work is not in agreement to the values given by Busey and Mesmer [42]. This is due to the deposition of iron oxide as hematite (Fe_2O_3) in the reactor, especially in the **PC**. It has been reported that iron changes the interaction of dissolved silica significantly and hence interacts with corrosion products [104, 105, 120-125].

In order to model the equilibrium corrosion effect with silica, the Bockris model is taken into account ([95]-p.260). The model is shown in figure 4-24(c), where the equilibrium potentials of iron and hydrogen are shown on the y-axis. The potential of iron is lower than of hydrogen. This forces the iron to act as an anode and be oxidized and hydrogen ion is reduced, until a passive layer is formed on the stainless steel surface.

However, hydrogen was continuously available through an automated magnetic valve in the experiment. This means that the availability of the constant partial pressure of hydrogen facilitated the redox reaction continuously. Corrosion occurring in the reactor is shown in figure 4-25 figuratively (see page 87 of this work).

a)

b) 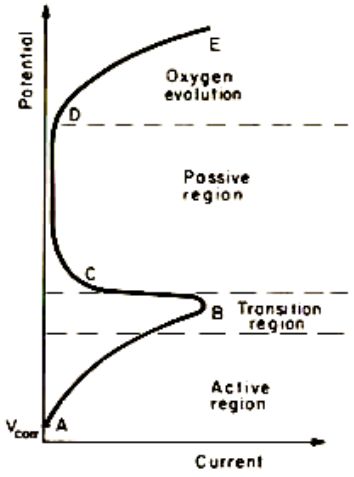

Fig. 9.16. Passivation.

c) 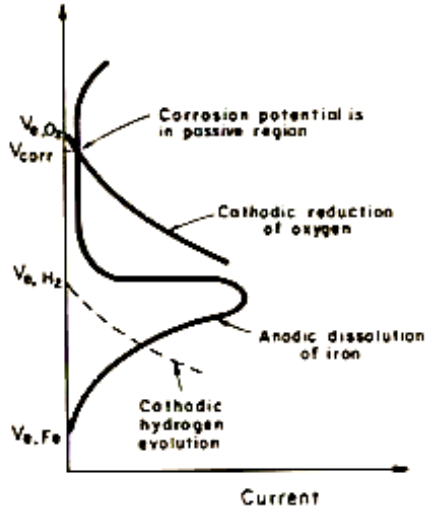

d) 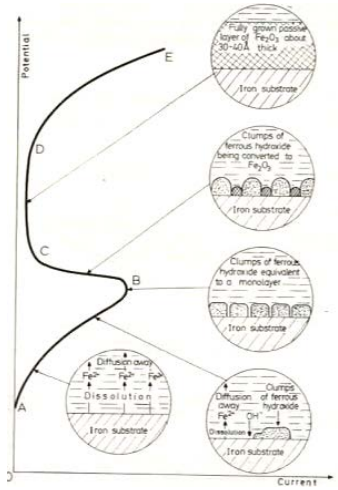

Figure 4-24 – Proof of stainless steel corrosion of the reactor due to injection of H_2 from the conducted experiment in this investigation(a) and the formation of ionic iron species, iron hydroxide and iron oxides from Bockris(b, c, d) ([95]-p.260).

The corrosion constant, $Q_{DISS,CORR}$ is given by equation 3-68:

$$Q_{DISS,CORR} = \frac{[H_2]_{1/2}}{[H^+]^2_{Fe,1/2}} \times \frac{[Fe^{2+}]_{1/2}}{[Fe_{(s)}]_{1/2}} \times \frac{[Fe(OH)_{3(s)}]_{1/2}[H^+]^3_{Fe,1/2}}{[Fe^{2+}]_{1/2}[H_2O]^3_{1/2}}$$

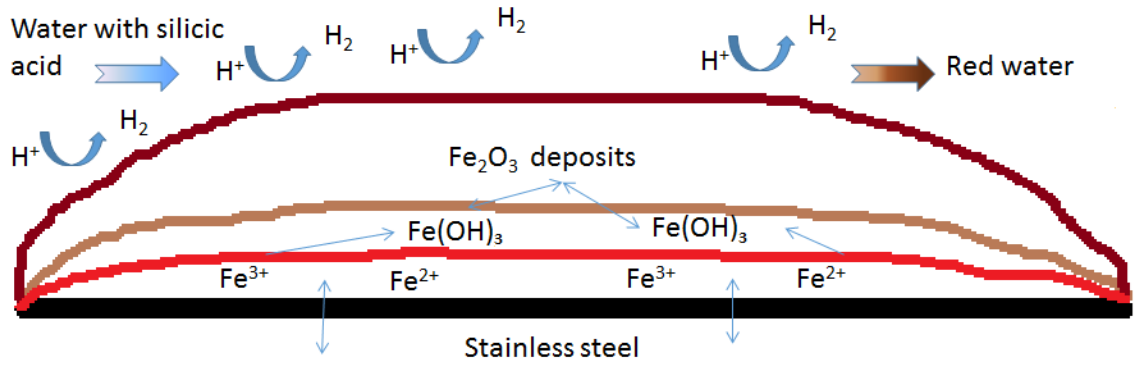

Figure 4-25 – The schematic representation of the formation of iron oxide deposits as mentioned by Bockris ([95]-p.260).

4.2.1.3.1 The electrochemical potential measurement (ECP) of iron corrosion by means of linear sweep measurements

In order to perform a corrosion model calculation and measurements in a high temperature electrochemical cell between the reaction for corrosion phenomena, hydrogen dissociation and silicic acid dissociation, first the existence of corrosion must be proven in a simple setup. For this, electrochemical linear sweep measurements are done in an electrochemical glass cell from MetroOHM with a MOD.7050 potentiostat from AMEL Instruments.

The temperature was controlled through an outer jacket with a thermostat. Linear sweep measurements are favored as the reversible corrosion potential is measured without the presence of a passive layer on bare stainless steel. Cyclic voltammetry measurements would measure the potential after the formation of a passive layer upon returning from the anodic to the cathodic region. This should be avoided especially for the determination of thermodynamic properties ([98]-p.82).

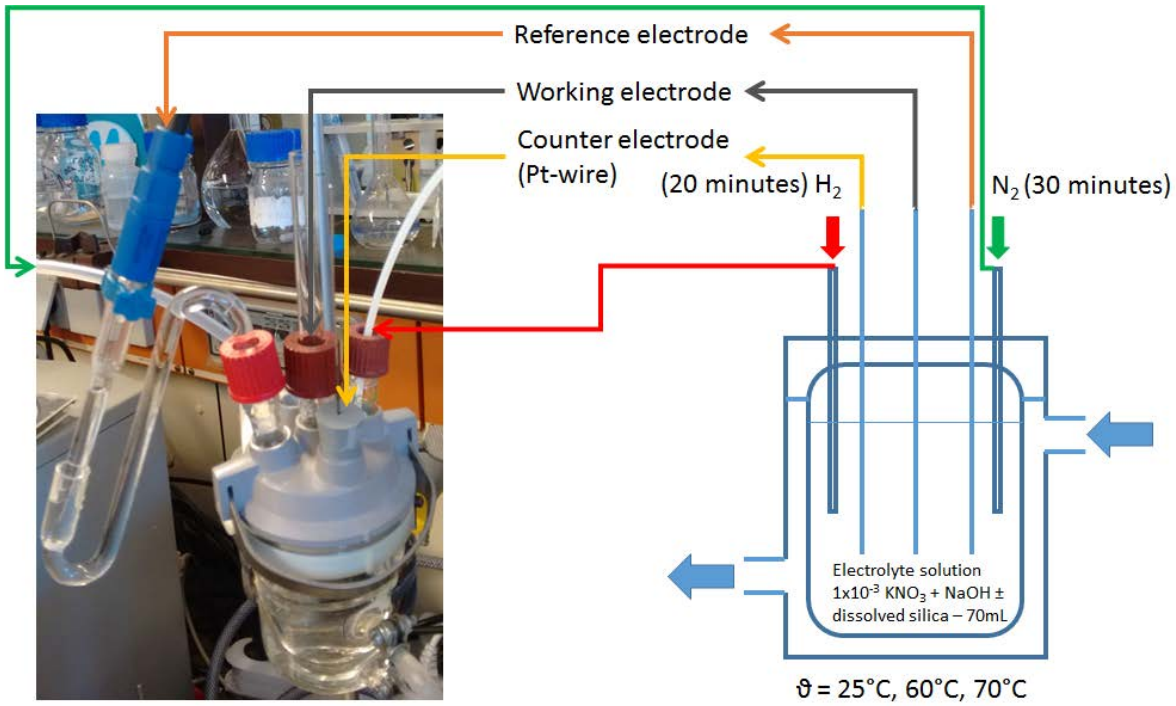

Figure 4-26 – The electrochemical glass cell for the validation of the equilibrium conditions.

A Pt-wire was used as the counter electrode, a 2cm by 0.2cm stainless steel probe as the working electrode and the reference electrode used is a Ag/AgCl electrode. A solution [**ES**] of 1x 10^{-3} moles/L of KNO_3 with 0, 0.052 and 0.52 moles of NaOH to give a pH of 7, 12 and 13 was used as the electrolyte. The solution was filled in an electrochemical glass cell (see figure 4-26) and purged with N_2 for 30 minutes. Hydrogen is injected to the system for 20 minutes while measuring the Open Circuit Potential (OCP) value. Then the linear sweep measurement is done between the values of -0.8V to 0.5V with a scan rate of 5mV/s. This then gives the Tafel plots.

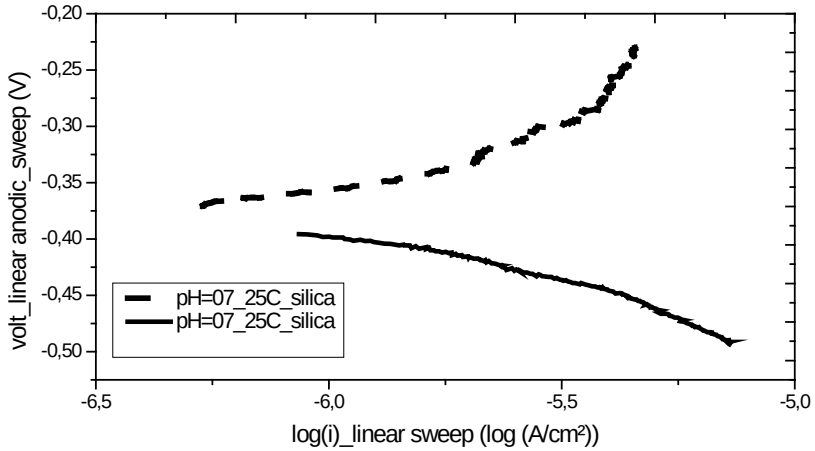

Figure 4-27-Tafel extrapolation of anodic and cathodic curves to determine the equilibrium potential.

From the figure 4-27 a linear trend is taken from the anodic line and cathodic line. The points of intersection of these two lines represent the equilibrium potential of the respective working electrode in the solution of concern. Further values are shown in the appendix 7.2.1.

The Tafel extrapolation was done for all pH values from 25°C, 60°C and 70°C respectively to prove the corrosive conditions existing in the high temperature electrochemical cell (see appendix 7.2.1). This is done for the identical electrolyte solution [**ES**] in the high temperature electrochemical cell (1x 10^{-3} KNO_3 solution at pH=7, 12 and 13), with and without the presence of silica.

The presence of the electrolyte does not affect the equilibrium concentration and dissociation constant of dissolved silica ([37]-p.44).The difference of the ΔE_{corr} from Tafel plots between the values measured, with and without silica corresponds to the trends of measured values in the high temperature flow-through electrochemical cell as well.

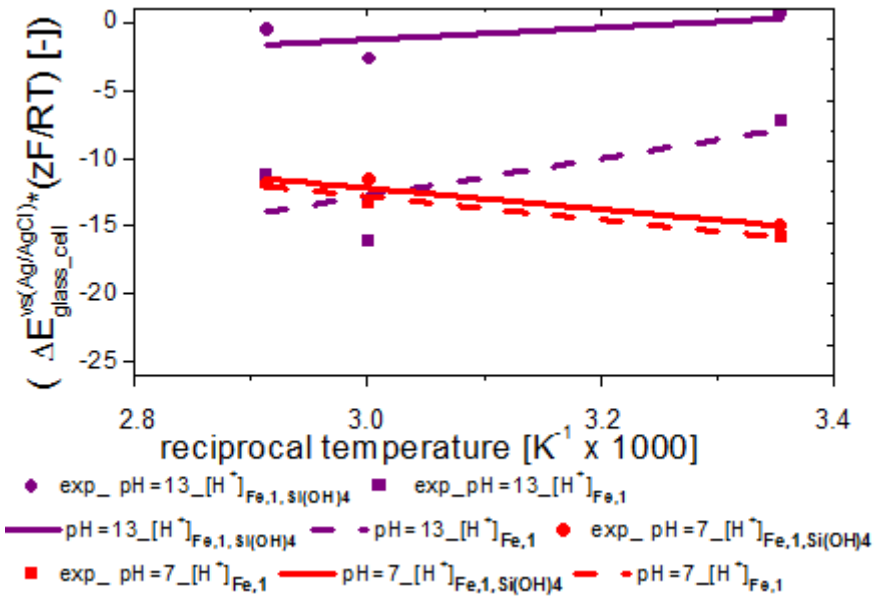

Figure 4-28-The equilibrium corrosion potential in the presence and absence of dissolved silica at ϑ=25°C to 70°C at pH=7 as well as pH=13

The figure 4-28 above shows the corrosion potentials of stainless steel at different pH and temperatures. As can be seen, the corrosion in the presence and absence of silica is nearly the same at pH = 7 and increases slightly with temperature. However, the corrosion in the absence of silica at pH = 13 is rather low and even decreases with temperature towards values of pH = 7.

This complies to the laws of thermodynamics as the slope of the ratio RT/zF in the Pourbaix diagram increases with temperature and the potential decreases with pH. Hence the passivation is favoured with increasing temperature. However, in the presence of silica, nearly no passivation occurs due to the inhomogeneous nature of the passive layer. There is possibly an interaction of the iron hydroxide ($Fe(OH)_3$) with dissociated silicic acid.

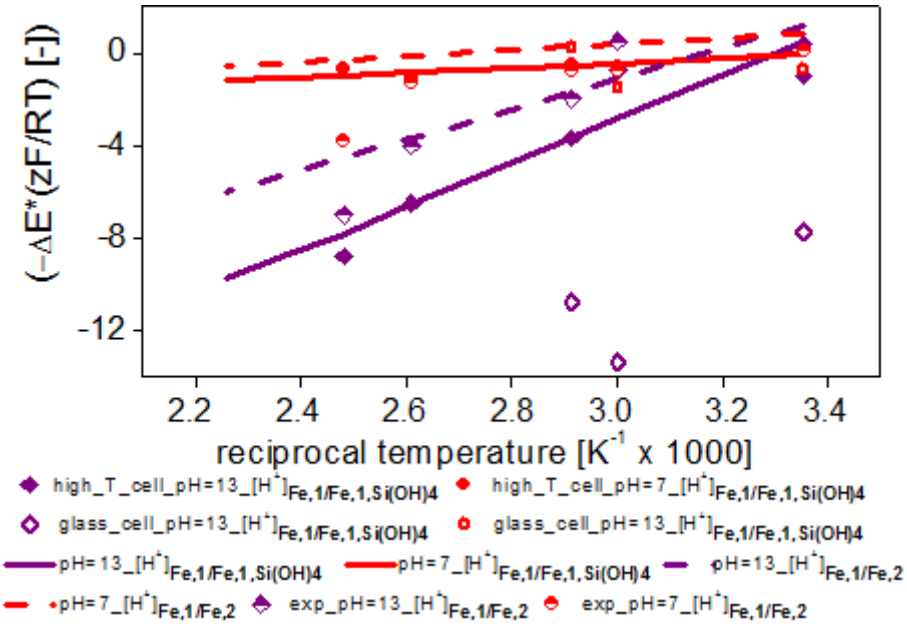

Figure 4-29 - The experimental equilibrium potentials from the high temperature electrochemical cell (filled and half-filled symbols) and the electrochemical glass cell (hollow symbols) at temperatures from 25°C to 70°C(hollow symbols) and 25°C to 130°C (solid symbols).

It can be seen that from the figure 4-29, the corrosion is rather inhibited in the high temperature cell for pH=7 and 13 without the presence of silica. Hence, a general inhibition trend due to deposition of iron oxide layers on stainless steel surfaces can be concluded without the presence of silica. This is observed also further for the value of the electrochemical glass cell at pH=13 (hollow purple symbol).

4.2.1.3.2 SEM and EDX-measurements

EDX-measurements provide the general prove of Fe_2O_3 for the calcined sample and goethite (FeOOH) for the uncalcined sample and silica deposition. EDX measurements together with SEM photos of the iron oxide formation were done in order to coarsely observe evidence of silica deposition under simultaneous iron oxide deposition. A sample of the porous Teflon frit

from the high temperature electrochemical cell is taken. It is thinly cut and placed on a SEM sample holder (photos of sample with sample holder in appendix 7.6). Silver paste was applied to the edges of the sample to acquire conductance. No silver paste was added for the uncalcined sample of the electrochemical glass cell. The stainless steel sample already has high conductivity and can be observed directly. The EDX sampling was done with a Hitachi S3200-N SEM device with images processed and scanned by the Digital Processing and Scanning System 5 respectively. EDX measurements were done with the INCAx-act device from the company Oxford with its respective software for image processing. A α-Cu beam was used for the sampling. From the EDX Data, intensity of silica on the iron oxide deposition location is identified. Results are shown in figure 4-30.

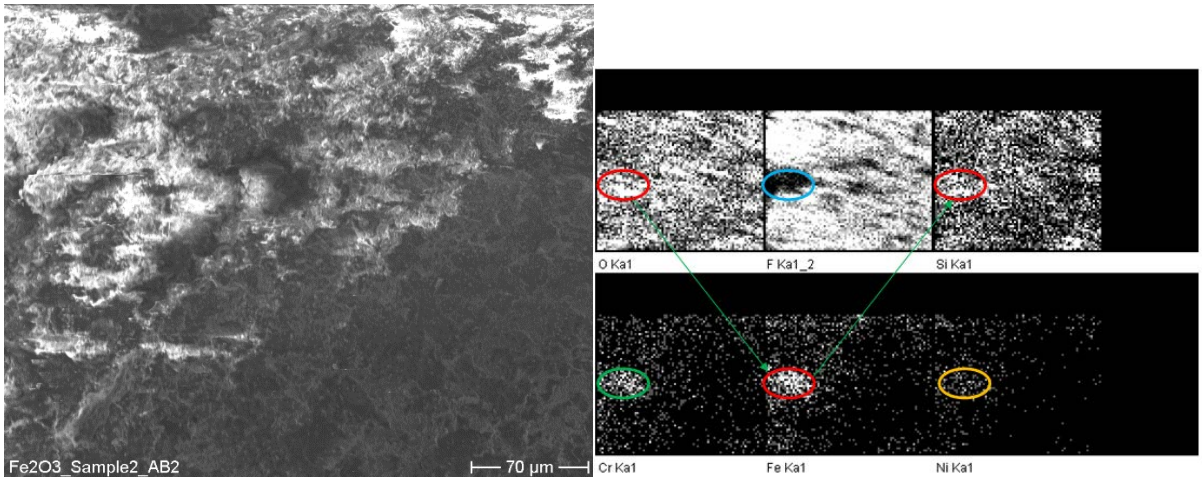

a)SEM and EDX images of Teflon surface with SiO_2/$Fe2O_3$ deposition.

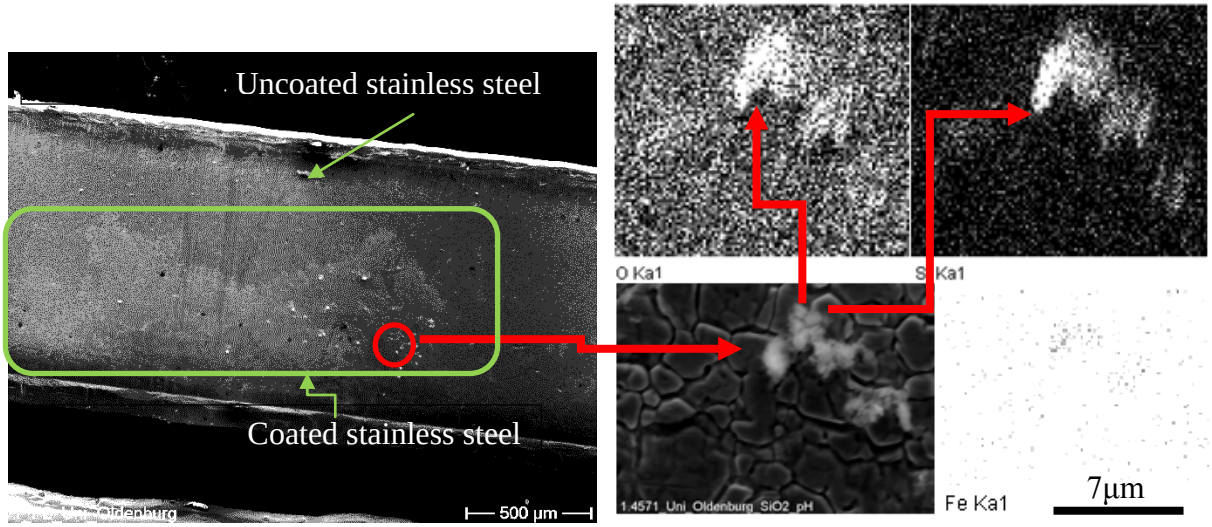

b)SEM and enlarged EDX images of uncalcined inhomogeneous SiO_2 layer on the stainless steel surface.

Figure 4-30 – EDX pictures of the elements present in the solid deposition.

4.2.1.3.3 IR measurements.

Rust deposits on the stainless steel surface of the high temperature electrochemical cell were washed with distilled water several times and the products collected. The products were dried first at 105°C for 24 hrs to remove excessive water and further calcined at 250°C for 24 hrs to remove the rest of the water trapped. Samples were measured at lower and higher calcination temperatures of 105°C and 250°C. Higher temperatures are not recommended as this will cause a phase change from hematite to maghemite [125].

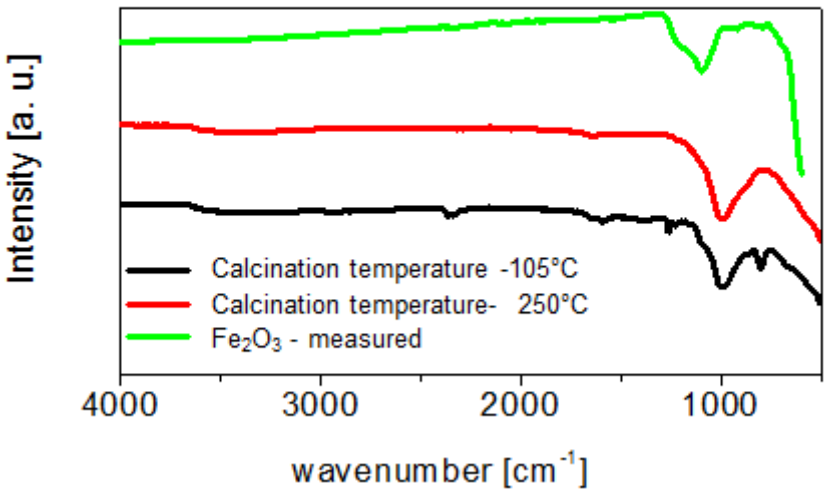

Figure 4-31 – IR-Spectra of the iron oxide deposits from the high temperature electrochemical cell in its calcined(red) and uncalcined(black) form.

Prove of Si-O-H and Fe-O-Si bands are available in literature and its vibration magnitudes are distinguishable by the shifting between the extremes of the Si-O-H band and the Si-O band. This work is able to prove the existence of Fe-O-Si bonds with respect to previously published data by Swedlund [122], Russell [124] and Li [125]. The existence of the Si-O-H bonds is given by the Si-O-H band at 1080 cm^{-1}. The band at 940 - 990cm^{-1} is the Si-O vibration as reported by Naren et al. [120], with a significant amount of Si-O-Fe linkages binding monodendately or bidendately to Fe on the stainless steel surface. The red and black spectra (low and high calcination temperatures) in figure 4-31 show a significant band at 990cm^{-1}. This proves the existence of Si-O-Fe-linkages on the surface. Proof of the iron oxide band is given below 800cm^{-1} in figure 4-31.

If higher silicate amounts are being bonded to ferrihydrite, the band shifts further to the lower frequency band. Bands for the presence of water are observed at 3430cm^{-1} and 1630cm^{-1} for the calcined sample at 105°C. The IR-measurements was done by a Golden gate bridge ATR method with a Bruker Tensor Spectrometer 27 from 300 cm^{-1} to 4000 cm^{-1}.

4.2.1.3.4 Raman measurements

The apparatus for Raman measurements is a Sentera Raman measurement device from Bruker. Raman spectrums are taken from the samples to identify the form of present iron oxide as hematite or goethite in the aqueous solution [126].

The intensity of the radiation is limited to 10mW with a laser frequency of 785nm and at rather short integration times of 4 minutes set by the software OPUS V6.5. It is to prevent the formation of other oxide polymorphs such as maghemite for the calcined sample.

For the calcined sample, samples from the high temperature electrochemical cell were taken. A blind sample of a microscope glass slate was measured for calibration and subsequently the measurement of the glass and the iron oxide deposit was done. The deposit was pressed to achieve a flat surface in order to improve the focus depicted on the microscope and the CCD camera, which was cooled at -90°C. The focus was adjusted each time to get the best resolution.

Another sample experiment was done on the surface of the uncalcined stainless steel sample affected by corrosion in the electrochemical glass cell. 5mW but longer integration times (6 minutes) with a laser frequency of 488nm was used for the sample from the electrochemical glass cell. A lower laser frequency was used to keep the penetration depth lower as the experiments for the electrochemical glass cell was done for a short period (1 hour per experiment).

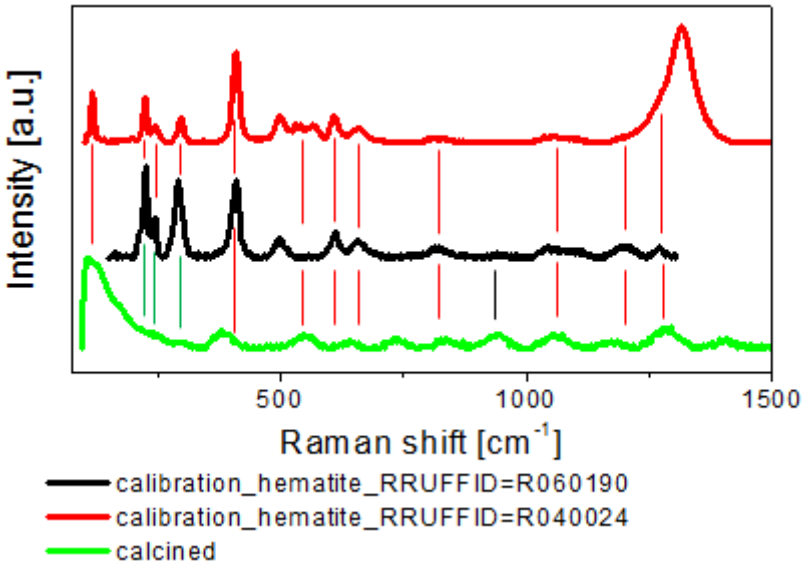

Figure 4-32 – The Raman spectra of the calcined sample (green) with two reference samples (black and red) is shown in the figure above.

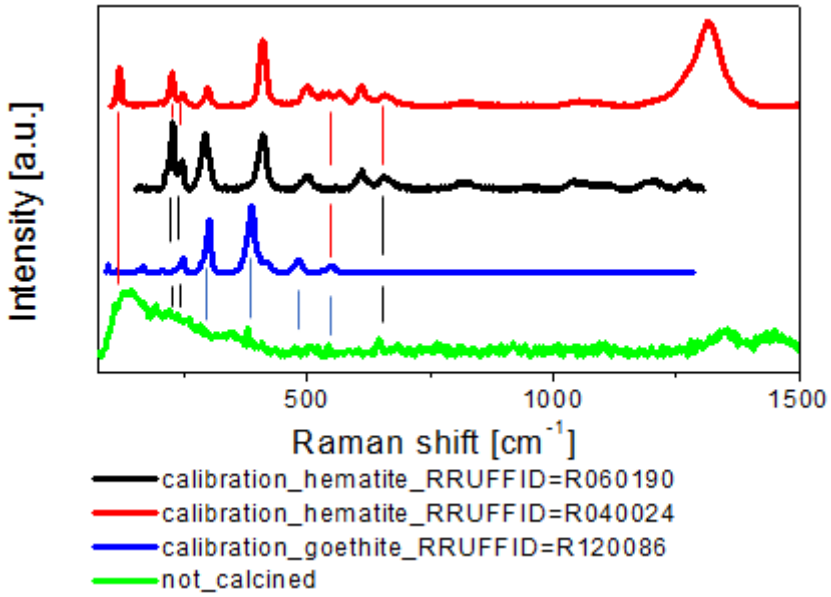

Figure 4-33 – Raman shifts of the uncalcined sample(green) and the reference for goethite(blue)[127] and two different pristine iron oxides (black and red).

In the high temperature electrochemical cell, the washed out and further calcined powder shows signs of a mixed pristine Fe_2O_3 oxide [128]. Raman shifts for the calcined sample shown in figure 4-32 are at 120, 226, 250, ~400, 540, 610, 650, 740, 822, 1175 cm^{-1}, 1250 cm^{-1} for the hematite type 1 and 2.

Additionally a shift at 950cm^{-1} for hematite type 2 is observed. This proves the existence of the mixed hematite phase. The deposition of the uncalcined sample from the electrochemical glass cell is shown in figure 4-33. Prove of goethite is observed at Raman shifts of 247, 300, 400cm^{-1} and Fe_2O_3 in a mixed form with peaks from 120 to 300cm^{-1}. The goethite and hematite peaks above 650cm^{-1} is too low to be observed, however the 400cm^{-1} peak gives a good proof for the existence of goethite.

This is why the peak is not sharp as the superposition of all the mentioned peaks gives the sharp edge at 120cm^{-1} and linear reduction up to 400cm^{-1}. The peaks for iron oxide are very low in the presence of silica. Hence it proves the previous conclusion made that the corrosion is further facilitated in the presence of silica. This is due to inhomogeneous coverage of iron oxide layers on the stainless steel surface.

4.2.1.4 Reaction equilibria

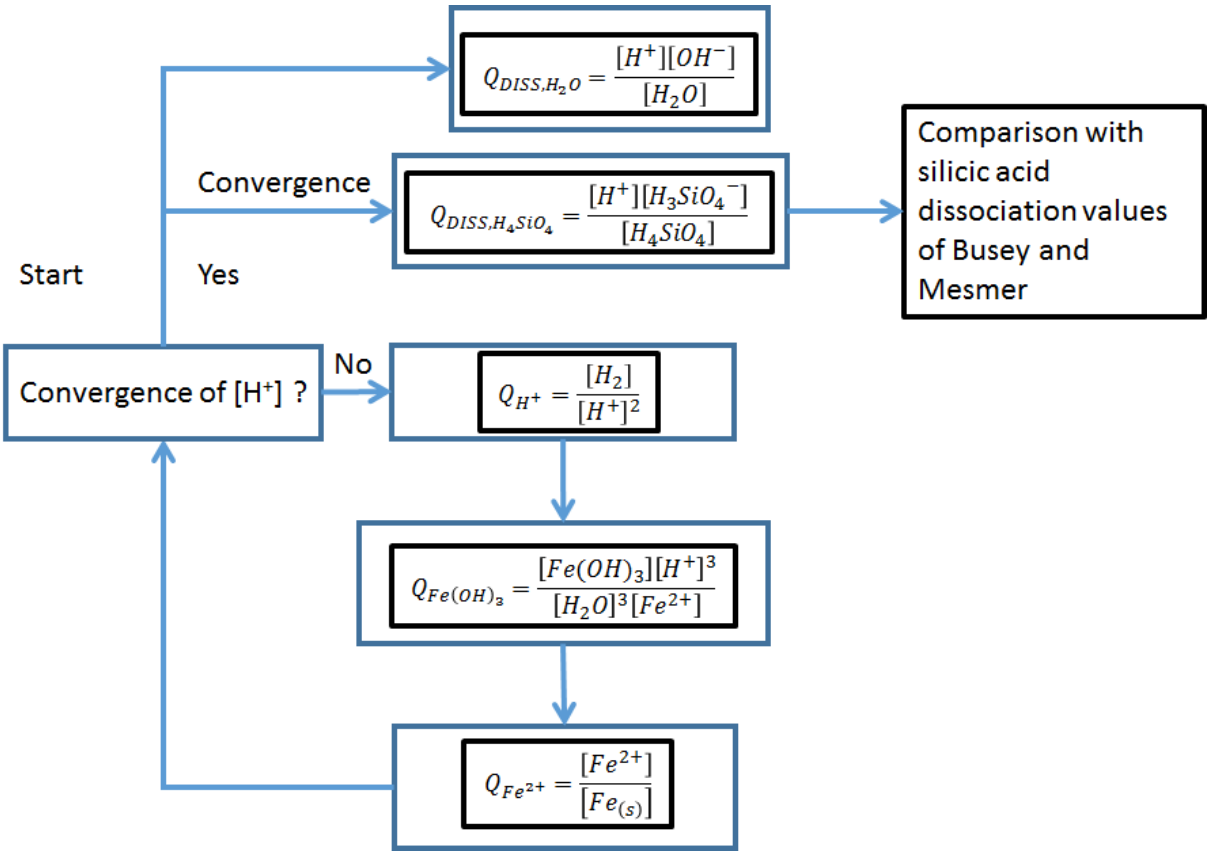

Figure 4-34 - The schematic flow diagram is shown above for the determination of the corrosion reaction to correspond to actual hydrogen ion concentration in the solution.

An attempt is made to model the corrosion reaction existing in the high temperature electrochemical cell shown in figure 4-34 according to the model of Bockris. The following reactions are considered:

$$2H^+ \rightleftarrows H_2 + 2e^- \qquad \text{R1}$$

$$H_2O \rightleftarrows H^+ + OH^- \qquad \text{R2}$$

$$H_4SiO_4 \rightleftarrows H^+ + H_3SiO_4^- \qquad \text{R3}$$

$$Fe_{(s)} \rightleftarrows Fe^{2+} + 2e^- \qquad \text{RC2}$$

$$Fe^{2+} + 3H_2O \rightleftarrows Fe(OH)_3 + 3H^+ + e^- \qquad \text{RC3}$$

$Q_{DISS,CORR,EXP}$ is taken from experimental values of the high temperature electrochemical cell by equation 3-70. Initial guesses of the concentration of protons from the injected hydrogen and pH value of the solution of concern is respectively made. Further calculation procedures are shown in Appendix 7.2.2. The initial guesses enter the iteration program to calculate $Q_{DISS,CORR}$. A target function for $Q_{DISS,CORR}$ is formulated for this purpose:

$$TF_{DISS,CORR} = \frac{\left(Q_{DISS,CORR;EXP} - Q_{DISS,CORR}\right)^2}{Q_{DISS,CORR;EXP}} = 0 \qquad \text{Equation 4-15}$$

The target function is minimized to exact equivalence of the experimental dissociation constants given by the Nernst relation by varying the hydrogen ion concentration according to the Newton method:

$$\frac{\partial TF_{DISS,CORR}}{\partial n_{H^+}} = -2\left(\frac{Q_{DISS,CORR;EXP} - Q_{DISS,CORR}}{Q_{DISS,CORR;EXP}}\right)\left[\frac{\left(1+4\Delta n_{H^+}\right)\left(n_{SUM}\right)}{\left(n_{H_2O}\right)^3} + \frac{5\left(n_{H_2}\, n_{H^+}\right)}{\left(n_{H_2O}\right)^3} + \frac{(-1)(-3)\left(n_{H_2}\, n_{H^+}\right)\left(n_{SUM}\right)}{\left(n_{H_2O}\right)^4}\right]$$

Equation 4-16

$$n_{H^+,iter+1} = n_{H^+,iter} - \left(\frac{TF_{DISS,CORR}}{\partial TF_{DISS,CORR} / \partial n_{H^+}}\right) \qquad \text{Equation 4-17}$$

Furthermore, upon determination of n_{H+}, the OH^- concentration can be determined as well. The dissociation constant of water ranges from 10^{-14} to 10^{-13} [129]. The values are shown in the Appendix 7.2.2. The values are calculated for two values of proton concentration in half – cell 2, as only ratios are calculated here. The proton concentration at half-cell 2 has two extremes, which is the pH value of half-cell 2 (10^{-7}) and unity. The iteration stops upon convergence of n_{H+} between two iterations.

$$\left\| x_{H^+,n+1} - x_{H^+,n} \right\| \leq \varepsilon \qquad \text{Equation 4-18}$$

$$\varepsilon = 1 \times 10^{-6} \qquad \text{Equation 4-19}$$

The results are compared with the results of Q_{H4SiO4} of Busey [42], to observe the reduction in the dissociation constant. The calculated values of $Q_{DISS,CORR}$ are depicted in figure 4-35. As can be observed, good convergence and agreement to experimental value (high temperature cell) is achieved.

The apparent pH value of half-cell 1 varies slightly due to the lower proton concentration in half-cell 1. This affects the dissociation constant of silicic acid in this investigation compared to that reported by Busey and Mesmer [42] due to corrosion effects.

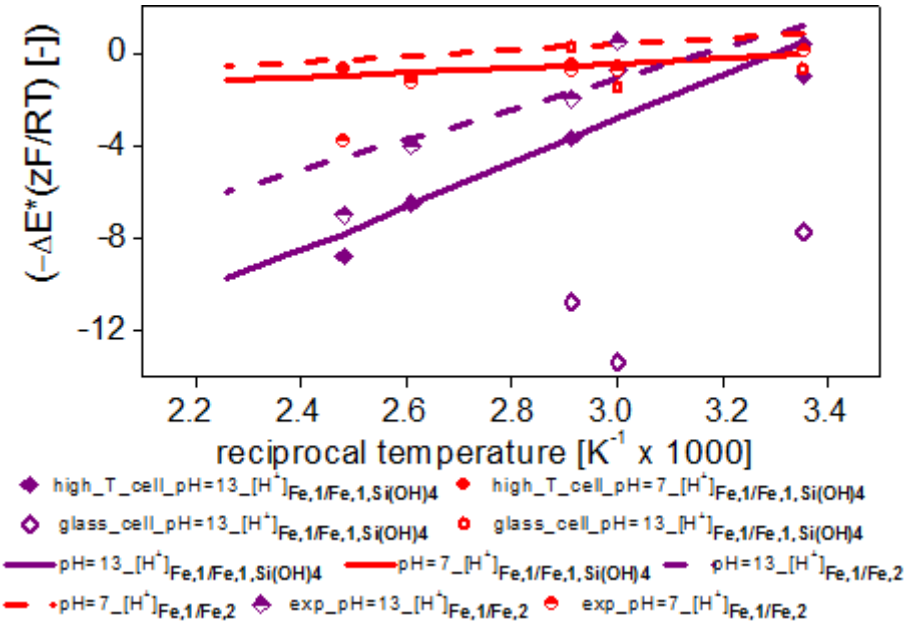

Figure 4-35 – The results of corrosion constants resulting from the reaction equilibria and their comparison with experimental results are shown above.

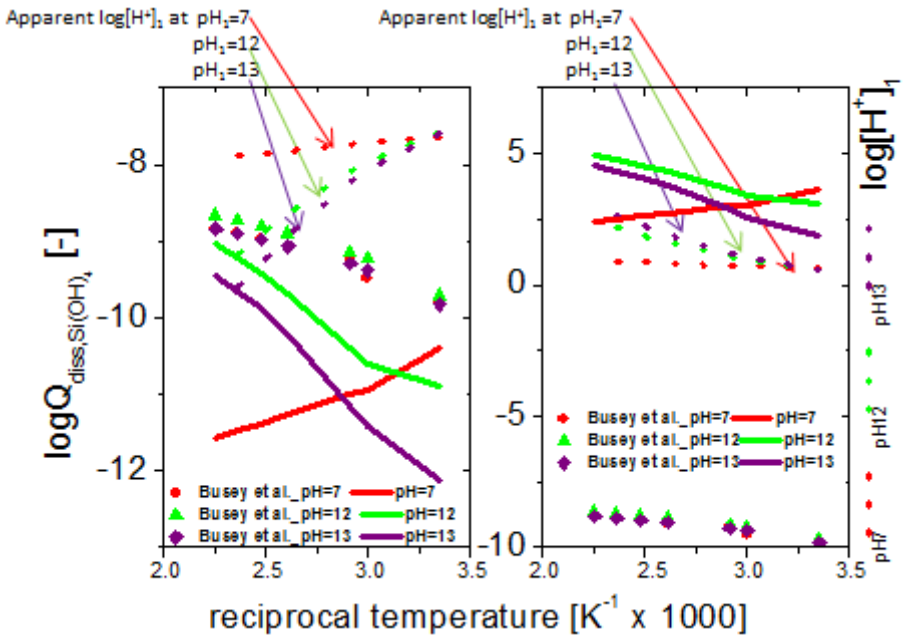

Figure 4-36 – The comparison of the calculated dissociation constants of silicic acid with literature data from Busey and Mesmer [42] and the calculated values from this work.

Figure 4-36 shows the dissociation constant of dissolved silica ($Si(OH)_4$) by Busey et al. [42] (filled points). The dotted line is the apparent pH of the half-cell 1 calculated from the corrosion model from equation 4-9 without the presence of silica. It is determined by multiplying the ratio by the proton concentration in the half-cell 2 ($H^+_{Fe,2}$). It has the limit of either 10^{-7} or unity. The solid lines represent the apparent silicic acid dissociation in the high temperature cell.

As the proton concentration of $H^+_{Fe,1}$ is available from equation 4-9, the proton concentration $H^+_{Fe,1,silica}$ is calculated from equation 4-13. As silicic acid is a weak acid, the concentration of dissociated silicic acid is equal the proton concentration $H^+_{Fe,1,silica}$ (See equation 3-66). The dissociation constant is hence determined from equation 3-65 by relating the squared value of $H^+_{Fe,1,silica}$ with the silicic acid concentration from UV-Vis measurements in figure 4-8.

From the left figure, it can be observed that all the dissociation constants of silicic acid in this work are lower than the reported values of Busey et al. [42]. The dissociation constants for pH = 12 and 13 show an increasing trend with increasing temperature. This trend complies with the trend reported by Busey et al [42]. However, the trend at pH=7 shows a decrease in the silicic acid dissociation with increasing temperature.

This is because the values of equation 4-9 for the ratio of the proton concentration in the half-cell 1 are decreasing, as for pH=12 and 13. However, the reducing proton concentration with

increasing temperature of equation 4-9 is not compensated by the ratio of equation 4-13 as for pH=12 and 13. This is due to its nearly constant ratio of proton concentrations of equation 4-13. Hence, the corrosion in the half-cell 1 at pH=7 decreases with increasing temperature. The increasing concentration of $Si(OH)_4$ at higher temperatures decreases the dissociation constants at pH=7 further.

From the right figure, at a $H^+_{Fe,2}$ concentration of unity, all silicic acid dissociation constants are significantly greater than the values reported by Busey et al. The dissociation constants even surpass the value of unity. As the proton concentration can achieve only a maximum value of unity, it is concluded that the proton concentration at $H^+_{Fe,2}$ is certainly lower than unity.

The trends of the dissociation constants are identical as only the value of the proton concentration in half-cell 2 is varied between 10^{-7} and unity. Therefore, it is concluded that the left figure has more significance to the silicic acid dissociation than the right figure of 4-36.

4.2.2 Results from vapour phase experiments

The vapour phase silicic acid concentration has significant importance as described generally by Jacobson and Opila [106, 107] and more specifically for zeolite syntheses by Althoff et al. [34]. This work tries to prove the existence of silicic acid in the vapour phase. No reaction mechanism in the vapour phase can be specified with the method chosen. The vapour liquid equilibrium relation will be established later in section 4.2.2.1.3.

4.2.2.1 Vapour phase equilibrium measurements of total silicic acid species

4.2.2.1.1 Setup of Quartz Crystal Microbalance

The quartz crystal microbalance is an in-house custom-made QCM. The circuit-design is taken from the manual of Linear Technologies for a quartz crystal resonance frequency of 10MHz to 25MHz. The microprocessor used for this purpose is of the type LT 1016. The circuit design is shown in Figure 4-37. The circuit is connected to an ARDUINO circuit to

convert the data into a readable form and transfer the data into a desktop computer. A Fortran 95 code is written to translate the frequency data with respect to time in a text file.

Prior to all measurements with amorphous silica, calibration measurements were done for all solutions concerned at pH-values of 7, 12 and 13 without the silica source. After calibration measurements, the respective experiments are conducted again with silica source. The average difference in frequency is taken and calculated for the mass difference with the Sauerbrey equation [109]. The mass difference is then subjected to the volume of the reactor to yield the concentration of silica in the vapour phase with respect to the constant volume of the reactor.

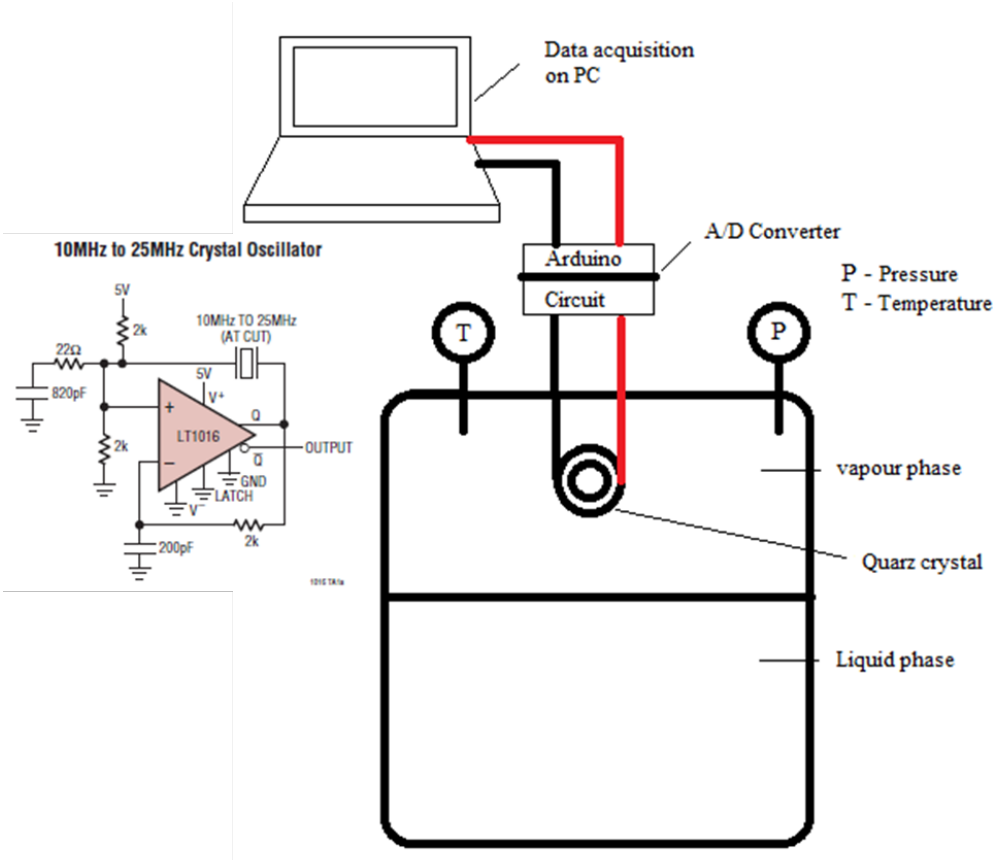

Figure 4-37 – A schematic diagram of the QCM employed for the vapour phase measurement with the integrated circuit to induce the resonance frequency.

4.2.2.1.2 Experimental Results of Quartz Crystal Microbalance

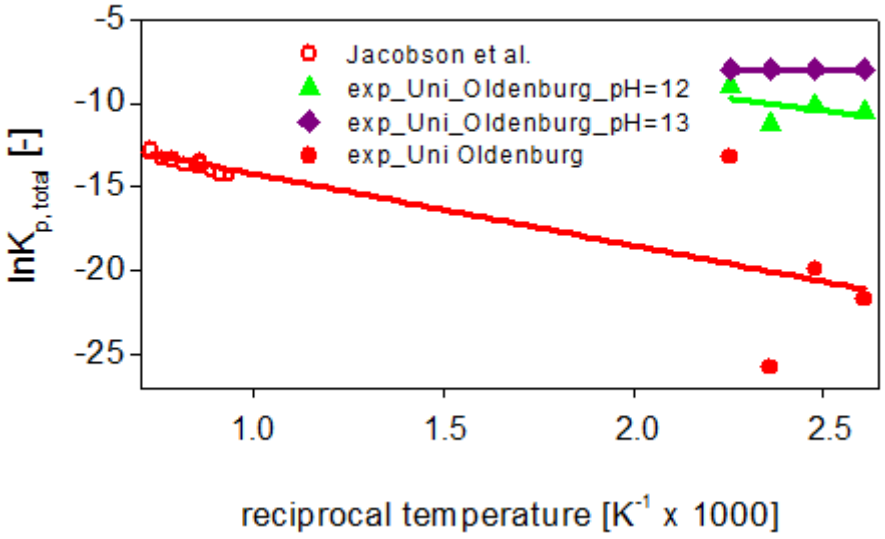

Figure 4-38 – Experimental logarithmic equilibrium constants data from the QCM method for the vapour phase is depicted.

The experimental work done is related to the calculated values with the Sauerbrey equation [109]. Equilibrium values of total silicic acid concentrations were calculated. Results are shown in figure 4-38. The measurements show large deviations in the vapour phase at pH=7. The results seem to be good at higher pH-values. The values at pH 7 were extremely difficult to measure. Therefore a linear relationship was deduced from the explanations of Busey et al. [42], Jacobson [106] and Bandura [129] to yield the values at pH=7.

However, they could be qualitatively modelled according to reasonable boundary conditions with Vapour Liquid Equilibrium calculation (see next section). The equation 3-24 is used to determine the total logarithmic equilibrium constant for the vapour phase, as done in the liquid phase.

4.2.2.1.3 VLE Results

The agreement of the vapour phase experiment is evaluated by an established multiphase equilibrium calculation method, in which the initial liquid phase concentration is specified and the concentration of both phases is calculated with the boundary condition that the tangent slopes of the Gibbs free energy of both phases are identical (see equation 3-3).

One starts at an arbitrary concentration given in a middle point as shown in figure 3-3. The calculation starts by assuming a high vapour concentration of the solvent and the liquid concentration are known from liquid phase investigations in section 4.2.1.1.3.1. The first derivatives of both the phases are evaluated. If these are not equal, the concentration is changed with a Newton-Raphson method with respect to the change of the concentration to the tangent slope. The iteration is terminated once the tangent slope of both phases is equal.

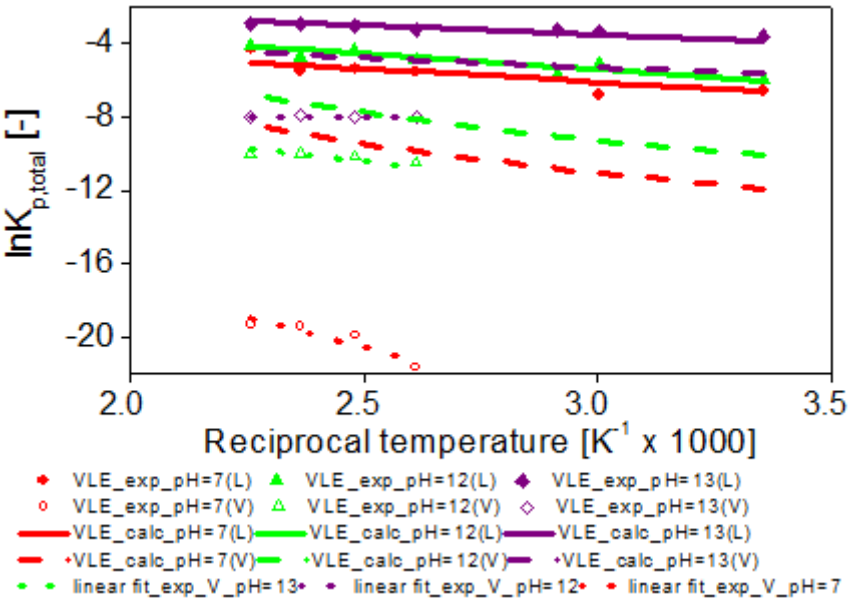

Figure 4-39 – The comparison of experimental and calculation logarithmic equilibrium constants for the liquid and vapour phases is shown in the figure above.

The results of the Rachford-Rice calculation in Figure 4-39 shows that the calculated values do not correspond to the measured values in the vapour phase. This may be due to the absence of the activity coefficient in the vapour phase.

5 Conclusion and Outlook

The objective of this work was to evaluate the feasibility of methods for elucidation of the thermodynamic silicic acid reaction pathways for the initialisation of zeolite syntheses by theoretical and experimental means. This was done by evaluating the results of the respective methods. The most important reactants in hydrothermal zeolite syntheses were taken for the evaluation, which is amorphous silica ($SiO_{2(am)}$) and water. It is reacted to its dissolved form (silicic acid).

In the liquid phase, solubility investigations for silicic acid species were done at pH-values of 7, 12 and 13 and temperatures from 25°C to 170°C. The solubility, respectively concentrations of silicic acid even at lower pH-values (pH< 12) were measured reasonably.

The total concentration of all silicic acid species was determined by the UV- Vis method, whereas the determination of the individual silicic acid species was done via Electron Spray Ionisation Mass Spectrometry (ESI-MS). The ESI-MS measurements give the molar intensity (in fractions) and the equilibrium constants of the respective silicic acid species. It is observed that the consistency between the ESI-MS and UV-Vis methods for the total equilibrium constants was marginally achieved. A possible reason for this may be the insufficient reaction time of the UV-Vis method or the measurement conditions of the ESI-MS method.

Therefore, computer-supported thermodynamic equilibrium calculations were used to give a qualitative reason for the discrepancy. This is based on an equilibrium reaction model, in which the pathways are derived mainly from data in this investigation and explanations from literature. The reaction model consists of condensation, cyclisation and dissociation reactions, which are coupled to each other and calculated simultaneously.

The results from the equilibrium measurements show significant reduction in the total equilibrium constant. This is due to the coupling of a large number of reactions to the model. If too much silicic acid (high equilibrium constant) is converted by subsequent reactions, the reduction in the reactants increases the equilibrium constants in other reactions and brings the system to divergence and possibly to a non-equilibrium state.

Further investigation especially for the cyclisation reaction is necessary. It is of great use to apply the Monte-Carlo simulation method for multiple reaction models and observe the tendency of each reaction model or a combination of reaction models coming into agreement with experimental values. These values of individual silicic acid species are compared further with quantum chemical results.

The tendencies of quantum chemical results are consistent to data provided in the literature. Some insights provided by quantum chemical calculations served well to design the reaction model. The cyclic species have lower concentrations compared to the mixed species in

general. However, the quantum chemical results show a reduction of the mixed species and increase in cyclic species with higher temperature.

The potentiometric measurement serves to determine the dissociation constant of silicic acid with the help of the Nernst equation. A flow-through electrochemical cell was designed and built, which could withstand pressures of up to 25 bars and temperatures of up to 200°C.

Unfortunately, the dissociation constant of silicic acid at hydrothermal conditions could not be measured due to corrosion at both half-cells, which are made of stainless steel. Literature data were taken for comparison of calculated results instead. Another electrochemical cell made of Hastelloy should be built for better measurement of the potential of silicic acid dissociation.

High temperature corrosion and corrosion inhibition for aqueous solutions from pH= 7 to 13 was measured by electrochemical potential measurements. It was done in the same custom-designed high temperature flow-through electrochemical cell. Electrochemical measurement of stainless steel in solutions of concern with respective pH values were done in an electrochemical glass cell up to 70°C to prove corrosive conditions. SEM images and EDX measurements were done to generally prove the inhomogeneous iron oxide deposition in the presence of silica in the solution. Further prove of low iron oxide formation is proven by Raman measurements and the band at 990cm^{-1} by means of IR spectroscopy, measures mono- and bidentate Si-O-Fe- linkages.

The values of the corrosion model calculation achieved good agreement upon comparison with the experimental results to 130°C. This is observed both in the electrochemical glass cell and in the high temperature cell. This shows that the model used in this work describes the corrosion phenomena well. The results show the silicic acid dissociation resulting from the corrosion effects. The results show a marked dependency in the dissociation of silicic acid for all pH values and temperatures by different proton concentrations.

This hence proves the reduction in the corrosion of stainless steel due to the reduction in concentration of hydrogen ions in the absence of silica. This leads in reduction of Fe^{2+}. Furthermore, the dissociated silicic acid is responsible for interaction on the stainless steel surface and formation of a partial silicate layer. This results in the reduction of the

dissociation constant of silicic acid and facilitates corrosion. This occurs although the concentration of silicic acid in its neutral form ($Si(OH)_4$) is higher at increased pH and temperatures. This is proven by calculations of the corrosion model as well as by Raman, IR and EDX measurements.

The presence of silicic acid species in the vapour phase was measured with some discrepancy (pH< 10) at different pH-values (pH= 7, 12, and 13) and temperatures of 110°C, 130°C, 150°C and 170°C with the quartz crystal microbalance (QCM) method. For this purpose, a good measuring conception is needed in order to measure silicic acid concentrations with the QCM method even though values at higher pH-values seem to be reasonable. A more equipped instrument should be built with new autoclaves with more sensitive real-time frequency sensors to get specific information of the silicic acid species involved.

These results are also compared with theory-based values. The thermodynamic multiphase calculation method of Rachford and Rice gave concentrations respectively equilibrium constants for the vapour phase. The calculated equilibrium constants for the vapour phase do not correspond to experimental values. These values are subject to further investigation as well and should be further compared with quantum chemical calculations. Furthermore, the reaction mechanism in the vapour phase may vary from the mechanism provided in the liquid phase.

The compensation of the deviation between experimental and theoretical investigation should follow in coming investigations. Improved reactor design is necessary to achieve ideal measurement conditions. In-situ, as well as, automated analytic measurements needs to be integrated into the reactor design to minimize measurement errors. Some recommendations are given in this work.

The deviation of the theoretical calculations should follow with introduction of activity coefficients, however with proper reasoning such as the introduction of a stronger solvent effect by means of the Deby-Hückel theory and the polymerisation activity with respect to the Flory-Huggins Theory. This work has maintained its aim to evaluate the feasibility of different theoretical and experimental methods. Hence, attempts to improve the methods are not taken.

The objective of this work was to evaluate the feasibility of methods used for elucidation of the thermodynamic reaction pathways for the initialisation of zeolite syntheses. The feasibility of the method is applicable to provide information on measurement efficiency, and gives useful trends towards the elucidation of silicic acid reaction pathways for the initialisation of zeolite syntheses.

Zusammenfassung der Arbeit

Experimentelle und theorie-basierte Untersuchungen zur Kieselsäurebildung unter hydrothermalen Bedingungen – ein Methodenvergleich

Das Ziel dieser Arbeit ist es, die möglichen Reaktionen von SiO_2- bzw. Kieselsäure-Spezies unter hydrothermalen Bedingungen aufzuklären. Dies soll zum allgemeinen Verständnis der hydrothermalen Zeolithsynthesen beitragen. Das Fokussieren auf die für die synthetische Herstellung von Zeolithen verwendeten Si-Quellen war aus experimentellen und zeitlichen Gründen notwendig.

In der flüssigen Phase werden Untersuchungen zur Löslichkeit der Si-Quellen in Wasser bei pH-Werten von 7, 12 und 13 und Temperaturen von 25 ° C bis 170 ° C durchgeführt. Die Löslichkeiten bzw. die recht geringen Konzentrationen an SiO_2-Spezies konnten auch bei niedrigeren pH-Werten (pH <12) zuverlässig bestimmt werden. Die Konzentration aller Kieselsäurearten wurde als Summe mit Hilfe des UV-Vis-Verfahrens bestimmt, während die Bestimmungen der einzelnen Kieselsäure-Spezies über ESI-MS ermittelt wurden. Es wird beobachtet, dass die ermittelten Gleichgewichtskonstanten bei Verwendung der ESI-MS-Methode im Vergleich zum UV-Vis-Verfahren nicht befriedigend übereinstimmten. Gründe dafür sollten experimentelle Unzulänglichkeiten sein, auf die in den entsprechenden kapiteln der Arbeit spekulativ eingegangen wurde. So wurden computergestützte thermodynamische Gleichgewichtsberechnungen verwendet, um eine qualitative Begründung für die Diskrepanz geben zu können. Dies basiert auf einem Reaktionsmodell, in dem die Reaktionswege hauptsächlich aus den Daten in dieser Untersuchung und unter Einbeziehung von Literaturangaben abgeleitet werden. Das Reaktionsmodell besteht aus Polymerisation (Kondensation), Cyclisierung und Spaltungsreaktionen, die miteinander gekoppelt und simultan berechnet worden sind.

Die Ergebnisse aus den Gleichgewichtsmessungen zeigen eine signifikante Reduktion der Gesamtgleich-gewichtskonstanten. Für weitergehende Untersuchungen (insbesondere für die

Cyclisierungsreaktion) ist die Anwendung der Monte-Carlo-Simulation von großem Nutzen, so dass eine tendentielle Konsistenz mit den experimentellen Werten erreicht wurde.
Diese Werte die einzelnen Kieselsäure-Spezies wurden darüber hinaus mit quantenchemischen Ergebnissen verglichen. Die Ergebnisse der quantenchemischen Berechnungen zeigen eine Reduktion gemischter Strukturen im Vergleich zur Ausbildung cyclischer Strukturen mit Erhöhung der Temperatur. Allerdings liegt immer noch eine geringere Konzentration der cyclischen Spezies im Vergleich zur gemischten Spezies vor. Auch hier konnte ein Einklang mit Literaturdaten und einige der Erkenntnisse erzielt werden. So dienten auch die quantenchemischen Rechnungen der Validierung des Reaktionsmodells.

Die potentiometrische Messung dient dazu, die Dissoziationskonstante mit Hilfe der Nernst-Gleichung zu bestimmen. Ein Durchflusselektrochemische Zelle wurde entworfen und gebaut, die Drücke bis zu 25 bar und Temperaturen von bis zu 200 ° C standhalten konnte. Leider konnten die Dissoziationskonstante von Kieselsäure bei hydrothermalen Bedingungen infolge von Korrosion an den beiden Halbzellen, die aus rostfreiem Stahl hergestellt sind, nicht gemessen werden. Deshalb wurden zum Vergleich mit den berechneten Werten Literaturdaten übernommen. Eine weitere elektrochemische Zelle aus Hastelloy sollte für eine bessere Messung des Potentials von Kieselsäure Dissoziation eingebaut werden.

Hochtemperatur-Korrosion und Korrosionshemmung für wässrige Lösungen wurden für pH-Werte zwischen 7 und 13 durch elektrochemische Potential-Messungen bestimmt. Für die elektrochemischen Messungen in Lösungen mit entsprechenden pH-Werten wurde vergleichend eine elektrochemische Glaszelle, die Untersuchungen bis zu 70 ° C zu lies, durchgeführt, um so den Einfluss durch korrosive Bedingungen nachzuweisen. REM-Aufnahmen und EDX-Messung wurden durchgeführt, um Änderungen auf den Edelstahloberflächen zu visualisieren und Ablagerungen zu analysieren. Die entstandenen Eisenoxidbildungen wurden durch Raman-Messungen und Analyse der Bande bei 990cm^{-1} mittels IR-Spektroskopie (Nachweis ein- und zweizähligen Si-O-Fe-Bindungen) nachgewiesen.

Die Werte der Korrosionsmodellrechnung erzielt gute Übereinstimmung bei einem Vergleich mit den experimentellen Ergebnissen zu 130 ° C. Dies wurde sowohl bei der elektrochemischen Glaszelle und bei Verwendung der Hochtemperaturzelle (Edelstahl) beobachtet. Dies zeigt, dass das in dieser Arbeit verwendet Modell die

Korrosionserscheinungen gut beschreibt. Die Ergebnisse ergeben eine Abhängigkeit der Kieselsäure-Dissoziation und die Korrosions-effekten vom pH-Wert und der Temperatur. Dies belegt die Verringerung der Korrosion von Edelstahl aufgrund der Verringerung der Konzentration der Protonen in Abwesenheit von Kieselsäure. Weiterhin führt die Wechselwirkung der dissoziierten Kieselsäure mit der Oberfläche des Edelstahls ausschließlich zur Bildung silikatischer Abscheidungen, wie die EDX-Messungen belegen. Dies führt zu einer Verringerung der Dissoziationskonstante der Kieselsäure und erleichtert die Korrosion. Die Ergebnisse werden durch Berechnung des Korrosions- Modells sowie Raman- und IR-Messungen bestätigt.

Die Anwesenheit von Kieselsäure-Spezies in der Dampfphase wurde bei verschiedenen pH-Werten (pH = 7, 12 und 13) und Temperaturen von 110 ° C, 130 ° C, 150 ° und 170 ° C mit dem Quarzkristall-Mikrowaage (QCM) gemessen. Hier zeigten die Messungen bei pH = 7 große Diskrepanzen. Ursache dafür sollten die zu geringen Sensitivitäten der Messapparatur sein. Verwendet wurde das thermodynamische Berechnungsverfahrens Rachford und Rice für mehrphasige Systeme, aus dem Konzentrationen bzw. Gleichgewichtskonstanten für die Dampfphase zu ermitteln sind. Ein Vergleich mit quantenchemisch berechneten Daten sowie Schlussfolgerungen bezüglich eines (im Vergleich zur Flüssigphasenreaktion) geänderten Reaktionsmechanismus konnten nicht konkretisiert werden.

Abweichungen zwischen den experimentellen und theoretischen Arbeiten sind hauptsächlich daraus entstanden, dass verschiedene idealisierte Annahmen getroffen wurden (Vernachlässigung der Kinetik, ideale Messbedingungen, ideale Mischverhalten). Die Abweichung zwischen experimentell ermittelten Daten und theoretischen Berechnungen sollte mit der Berücksichtigung eines stärkeren Lösungsmitteleffekt durch die Debye-Hückel-Theorie und Korrekturen der Aktivitäten in Bezug auf die Flory Huggins-Theorie verringert werden. Dies war bei der Komplexität der Aufgabenstellung in der für diese Arbeit zur Verfügung stehenden Zeit nicht möglich. Dennoch gelang es experimentelle Messungen und thermodynamisch-basierten sowie quantenchemischen Berechnungsmethoden gegenüber-zustellen. Insbesondere wurden bei den experimentellen Methoden neuartige Apparaturen konzipiert und deren Funktionalität erprobt sowie Vorschläge zur Weiteiterentwicklung und Verbesserung deren Funktionsweise unterbreitet.

6 References

1. K. Byrappa, Y.M., *Handbook of Hydrothermal Technology*. 1 ed. 2001, Park Ridge, New Jersey, USA: Noyes Publications, William Andrew Publishing LLC. 891 pages.
2. F. Bergius, *Beiträge zur Theorie der Kohleentstehung.* Die Naturwissenschaften, 1928. **1**(16): p. 1-11.
3. X.J. Cui, M. Antonietti, and S.H. Yu, *Structural effects of iron oxide nanoparticles and iron ions on the hydrothermal carbonization of starch and rice carbohydrates.* Small, 2006. **2**(6): p. 756-759.
4. J. Ohlert, *Dissertation*, in *Technical Chemistry*. 2015, University of Oldenburg: Oldenburg.
5. M. Röhrdanz, T. Rebling, J. Ohlert, J. Jasper, T. Greve, R. Buchwald, P. von Freiling, M. Wark, *Hydrothermal carbonization - Influence of process parameters on pedological hydrochar properties.* Journal of Plant Nutrition and Soil Science, 2015 (submitted).
6. C.S. Cundy and P.A. Cox, *The hydrothermal synthesis of zeolites: Precursors, intermediates and reaction mechanism.* Microporous and Mesoporous Materials, 2005. **82**(1-2): p. 1-78.
7. M. Okrusch, Matthes.S., *Mineralogie: Eine Einführung in die spezielle Mineralogie, Petrologie und Lagerstättenkunde* 8ed. 2010, Springer-Lehrbuch.
8. C. Baerlocher, W. M. Meier, D. Olson , *Atlas of zeolite framework types*. 5th rev. ed. 2001, Amsterdam ; New York: Elsevier. vi.
9. W.M. Meier, D. Olson, and International Zeolite Association. Structure Commission., *Atlas of zeolite structure types*. 2nd rev. ed. 1987, London ; Boston: Published on behalf of the Structure Commission of the International Zeolite Association, by Butterworths.
10. J. Čejka, *Introduction to zeolite science and practice*. 3rd rev. ed. Studies in surface science and catalysis. 2007, Amsterdam ; Boston: Elsevier. viii.
11. S. Mintova, N.H. Olson, and T. Bein, *Electron microscopy reveals the nucleation mechanism of zeolite Y from precursor colloids.* Angewandte Chemie-International Edition, 1999. **38**(21): p. 3201-3204.
12. S. Mintova, N. H. Olson, V. Valtchev, T. Bein, *Mechanism of zeolite a nanocrystal growth from colloids at room temperature.* Science, 1999. **283**(5404): p. 958-960.
13. S. A. Pelster, *Untersuchung der Festkörperbildung von Silicaten mittels Massenspektrometrie.* Dissertation, 2007, RU Bochum.
14. S. A. Pelster, W. Schrader, and F. Schuth, *Monitoring temporal evolution of silicate species during hydrolysis and condensation of silicates using mass spectrometry.* Journal of the American Chemical Society, 2006. **128**(13): p. 4310-4317.
15. S. A. Pelster, F. Schuth, and W.G. Schrader, *Detailed study on the use of electrospray mass spectrometry to investigate speciation in concentrated silicate solutions.* Analytical Chemistry, 2007. **79**(15): p. 6005-6012.
16. S. D. Kinrade, C. T. G. Knight, D. L. Pole, R. T. Syvitski, *Silicon-29 NMR studies of tetraalkylammonium silicate solutions. 2. Polymerization kinetics.* Inorganic Chemistry, 1998. **37**(17): p. 4278-4283.
17. S. D. Kinrade, C. T. G. Knight, D. L. R. T. Pole, Syvitski, *Silicon-29 NMR studies of tetraalkylammonium silicate solutions. 1. Equilibria, Si-29 chemical shifts, and Si-29 relaxation.* Inorganic Chemistry, 1998. **37**(17): p. 4272-4277.
18. C. T. Knight, , R.J. Balec, and S.D. Kinrade, *The structure of silicate anions in aqueous alkaline solutions.* Angew Chem Int Ed Engl, 2007. **46**(43): p. 8148-8152.

19. C. T. Knight, R.J. Balec, and S.D. Kinrade, *Aqueous alkali-metal silicate anions containing fully condensed four-coordinate sites.* Angew Chem Int Ed Engl, 2012. **51**(39): p. 9900-9903.
20. J. Sefcik and W.A. Goddard, *Thermochemistry of silicic acid deprotonation: Comparison of gas-phase and solvated DFT calculations to experiment.* Geochimica Et Cosmochimica Acta, 2001. **65**(24): p. 4435-4443.
21. J. Sefcik and A.V. McCormick, *Thermochemistry of aqueous silicate solution precursors to ceramics.* Aiche Journal, 1997. **43**(11): p. 2773-2784.
22. I. Gunnarsson and S. Arnorsson, *Amorphous silica solubility and the thermodynamic properties of H_4SiO_4 degrees in the range of 0 to 350°C at P_{sat}.* Geochimica Et Cosmochimica Acta, 2000. **64**(13): p. 2295-2307.
23. C. T. A. Chen and W.L. Marshall, *Amorphous Silica Solubilities .4. Behavior in Pure Water and Aqueous Sodium-Chloride, Sodium-Sulfate, Magnesium-Chloride, and Magnesium-Sulfate Solutions up to 350°C.* Geochimica Et Cosmochimica Acta, 1982. **46**(2): p. 279-287.
24. W. L. Marshall, *Amorphous Silica Solubilities .3. Activity-Coefficient Relations and Predictions of Solubility Behavior in Salt-Solutions, 0-350°C.* Geochimica Et Cosmochimica Acta, 1980. **44**(7): p. 925-931.
25. W. L. Marshall and J.M. Warakomski, *Amorphous Silica Solubilities .2. Effect of Aqueous Salt-Solutions at 25°C.* Geochimica Et Cosmochimica Acta, 1980. **44**(7): p. 915-&.
26. W. L. Marshall, *Amorphous Silica Solubilities .1. Behavior in Aqueous Sodium-Nitrate Solutions - 25-300°C, 0-6 Molal.* Geochimica Et Cosmochimica Acta, 1980. **44**(7): p. 907-913.
27. W.L. Marshall and C.T.A. Chen, *Amorphous Silica Solubilities .6. Postulated Sulfate-Silicic Acid-Solution Complex.* Geochimica Et Cosmochimica Acta, 1982. **46**(3): p. 367-370.
28. W. L. Marshall and C.T.A. Chen, *Amorphous Silica Solubilities .5. Predictions of Solubility Behavior in Aqueous Mixed Electrolyte-Solutions to 300°C.* Geochimica Et Cosmochimica Acta, 1982. **46**(2): p. 289-291.
29. R. O. Fournier and W.L. Marshall, *Calculation of Amorphous Silica Solubilities at 25°C to 300°C and Apparent Cation Hydration Numbers in Aqueous Salt-Solutions Using the Concept of Effective Density of Water.* Geochimica Et Cosmochimica Acta, 1983. **47**(3): p. 587-596.
30. J. Weitkamp, *Zeolites and catalysis.* Solid State Ionics, 2000. **131**(1-2): p. 175-188.
31. R. J. Argauer, G.R. Landolt, *Crystalline zeolite ZSM-5 and method of preparing the same*, U.P. Office, Editor. 1972: USA.
32. M. E. Davis and R.F. Lobo, *Zeolite and Molecular-Sieve Synthesis.* Chemistry of Materials, 1992. **4**(4): p. 756-768.
33. C. N. Satterfield, *Heterogeneous Catalysis in Industrial Practice*. 2 ed. 1991: McGraw-Hill.
34. R. Althoff, K. Unger, and F. Schuth, *Is the Formation of a Zeolite from a Dry Powder Via a Gas-Phase Transport Process Possible.* Microporous Materials, 1994. **2**(6): p. 557-562.
35. D. Rosenkranz, *Organisches Forschungspraktikum-Löslichkeitsuntersuchung von Siliziumdioxid in Wasser*, A. Brehm, Tamahrajah, Jaybalan, Editor. 2013, Carl-von-Ossietzky University of Oldenburg. p. 54.
36. J. Tamahrajah, *Forschungspraktikum: Quantenchemie - Bestimmung der Geometrien und freien Reaktionsenthalpien verschiedener Kieselsäurespezies in Wasser*, K. T., Editor. 2013, Carl-von-Ossietzky University of Oldenburg. p. 40.

37. R.K. Iler, *The chemistry of silica : solubility, polymerization, colloid and surface properties, and biochemistry*. 1979, New York: Wiley. xxiv.
38. J. Gmehling, B. Kolbe, Kleiber M., Rarey J., *Chemical Thermodynamics for Process Simulation.*, 2012, Wiley-VCH.
39. M. L. Michelsen, J.M. Mollerup, *Thermodynamic Models: Fundamentals and Computational Aspects*. 2004: Tie-Line Publications.
40. H. H. Rachford and J.D. Rice, *Procedure for Use of Electronic Digital Computers in Calculating Flash Vaporization Hydrocarbon Equilibrium.* Transactions of the American Institute of Mining and Metallurgical Engineers, 1952. **195**: p. 327-328.
41. S. Sjöberg, A. Nordin, N. Ingri, *Equilibrium and structural studies of silicon(IV) and aluminium(III) in aqueous solution. II. Formation constants for the monosilicate ions $SiO(OH)_3^-$ and $SiO_2(OH)_2^{2-}$. A precision study at 25°C in a simplified seawater medium.* Marine Chemistry, 1981. **10**(6): p. 521-532.
42. R. H. Busey and R.E. Mesmer, *Ionization Equilibria of Silicic-Acid and Polysilicate Formation in Aqueous Sodium-Chloride Solutions to 300°C.* Inorganic Chemistry, 1977. **16**(10): p. 2444-2450.
43. S. Sjöberg, Y. Hägglund, A. Nordin, N. Ingri, *Equilibrium and structural studies of Silicon(IV) and Aluminium(III) in aqueous solution. V. Acidity constants of silicic acid and the ionic product of water in the medium range 0.05–2.0 M Na(CI) at 25°C.* Marine Chemistry, 1983. **13**(1): p. 35-44.
44. S. Sjöberg, N. Ingri, A.-M. Nenner, L.-O. Öhman, *Equilibrium and structural studies of silicon(IV) and aluminium(III) in aqueous solution. 12. A potentiometric and 29Si-NMR study of silicon tropolonates.* Journal of Inorganic Biochemistry, 1985. **24**(4): p. 267-277.
45. K. R. Applin, *The Diffusion of Dissolved Silica in Dilute Aqueous-Solution.* Geochimica Et Cosmochimica Acta, 1987. **51**(8): p. 2147-2151.
46. G. B. Alexander, *The Effect of Particle Size on the Solubility of Amorphous Silica in Water.* Journal of Physical Chemistry, 1957. **61**(11): p. 1563-1564.
47. G. B. Alexander, W.M. Heston, and R.K. Iler, *The Solubility of Amorphous Silica in Water.* Journal of Physical Chemistry, 1954. **58**(6): p. 453-455.
48. T. H. Elmer and M.E. Nordberg, *Solubility of Silica in Nitric Acid Solutions.* Journal of the American Ceramic Society, 1958. **41**(12): p. 517-520.
49. D. A. Crerar and G.M. Anderson, *Solubility and Solvation Reactions of Quartz in Dilute Hydrothermal Solutions.* Chemical Geology, 1971. **8**(2): p. 107-&.
50. B. A. Fleming and D.A. Crerar, *Silicic-Acid Ionization and Calculation of Silica Solubility at Elevated-Temperature and pH - Application to Geothermal Fluid Processing and Reinjection.* Geothermics, 1982. **11**(1): p. 15-29.
51. S. A. Greenberg, T.N. Chang, and E. Anderson, *Investigation of Colloidal Hydrated Calcium Silicates .1. Solubility Products.* Journal of Physical Chemistry, 1960. **64**(9): p. 1151-1157.
52. S. A. Greenberg, *The Nature of the Silicate Species in Sodium Silicate Solutions.* Journal of the American Chemical Society, 1959. **80**(24): p. 6508-6511.
53. S. A. Greenberg and E.W. Price, *The Solubility of Silica in Solutions of Electrolytes.* Journal of Physical Chemistry, 1957. **61**(11): p. 1539-1541.
54. K. B. Krauskopf, *Dissolution and Precipitation of Silica at Low Temperatures.* Geochimica Et Cosmochimica Acta, 1956. **10**(1-2): p. 1-26.
55. R. Noort, C.J. Spiers, and C.J. Peach, *Structure and properties of loaded silica contacts during pressure solution: impedance spectroscopy measurements under hydrothermal conditions.* Physics and Chemistry of Minerals, 2011. **38**(7): p. 501-516.
56. J. A. Vanlier, P.L. Debruyn, and J.T.G. Overbeek, *The Solubility of Quartz.* Journal of Physical Chemistry, 1960. **64**(11): p. 1675-1682.

57. K. L. Vondamm, J.L. Bischoff, and R.J. Rosenbauer, *Quartz Solubility in Hydrothermal Seawater - an Experimental-Study and Equation Describing Quartz Solubility for up to 0.5M NaCl Solutions.* American Journal of Science, 1991. **291**(10): p. 977-1007.
58. S. H. Garofalini and G. Martin, *Molecular Simulations of the Polymerization of Silicic-Acid Molecules and Network Formation.* Journal of Physical Chemistry, 1994. **98**(4): p. 1311-1316.
59. M. Kagan, G.K. Lockwood, and S.H. Garofalini, *Reactive simulations of the activation barrier to dissolution of amorphous silica in water.* Physical Chemistry Chemical Physics, 2014. **16**(20): p. 9294-9301.
60. J. R. Hill and J. Sauer, *Molecular Mechanics Potential for Silica and Zeolite Catalysts Based on Ab-Initio Calculations .1. Dense and Microporous Silica.* Journal of Physical Chemistry, 1994. **98**(4): p. 1238-1244.
61. J. R. Hill and J. Sauer, *Molecular Mechanics Potential for Silica and Zeolite Catalysts Based on Ab-Initio Calculations .2. Aluminosilicates.* Journal of Physical Chemistry, 1995. **99**(23): p. 9536-9550.
62. Y. T. Xiao and A.C. Lasaga, *Ab initio quantum mechanical studies of the kinetics and mechanisms of quartz dissolution: OH- catalysis.* Geochimica Et Cosmochimica Acta, 1996. **60**(13): p. 2283-2295.
63. A. C. Lasaga and G.V. Gibbs, *Applications of Quantum-Mechanical Potential Surfaces to Mineral Physics Calculations.* Physics and Chemistry of Minerals, 1987. **14**(2): p. 107-117.
64. B. Mondal, D. Ghosh, and A.K. Das, *Thermochemistry for silicic acid formation reaction: Prediction of new reaction pathway.* Chemical Physics Letters, 2009. **478**(4-6): p. 115-119.
65. L. A. Montero-Cabrera, Y. Perez-Badell, and M.J. Mora-Fonz, *An approach to hydration of model silica materials by exploring their multiple minima hypersurfaces. The role of entropy of association.* Journal of Physical Chemistry A, 2008. **112**(13): p. 2880-2887.
66. M. D. Newton and G.V. Gibbs, *Abinitio Calculated Geometries and Charge-Distributions for H_4SiO_4 and $H_6Si_2O_7$ Compared with Experimental Values for Silicates and Siloxanes.* Physics and Chemistry of Minerals, 1980. **6**(3): p. 221-246.
67. M. D. Newton, M. O'Keeffe, and G.V. Gibbs, *Abinitio Calculation of Inter-Atomic Force-Constants in $H_6Si_2O_7$ and the Bulk Modulus of Alpha-Quartz and Alpha-Cristobalite.* Physics and Chemistry of Minerals, 1980. **6**(4): p. 305-312.
68. R.C.Newton and C.E. Manning, *Solubilities of corundum, wollastonite and quartz in H_2O-NaCl solutions at 800 ° C and 10 kbar: Interaction of simple minerals with brines at high pressure and temperature.* Geochimica Et Cosmochimica Acta, 2006. **70**(22): p. 5571-5582.
69. H. Henschel, A.M. Schneider, and M.H. Prosenc, *Initial Steps of the Sol-Gel Process: Modeling Silicate Condensation in Basic Medium.* Chemistry of Materials, 2010. **22**(17): p. 5105-5111.
70. L. T. Zhuravlev, *Concentration of Hydroxyl-Groups on the Surface of Amorphous Silicas.* Langmuir, 1987. **3**(3): p. 316-318.
71. L. T. Zhuravlev, *The surface chemistry of amorphous silica. Zhuravlev model.* Colloids and Surfaces a-Physicochemical and Engineering Aspects, 2000. **173**(1-3): p. 1-38.
72. A. Pelmenschikov, H. Strand, L. G. M., Pettersson, J. Leszczynski, *Lattice resistance to hydrolysis of Si-O-Si bonds of silicate minerals: Ab initio calculations of a single water attack onto the (001) and (111) beta-cristobalite surfaces.* Journal of Physical Chemistry B, 2000. **104**(24): p. 5779-5783.

73. G. Kolbe, *komplexchemische Verhalten der Kieselsaeure.* Dissertation, 1956, Friedrich-Schiller-Universtaet Jena.
74. G. J. McIntosh, *Theoretical investigations into the nucleation of silica growth in basic solution part I - ab Initio studies of the formation of trimers and tetramers.* Physical Chemistry Chemical Physics, 2013. **15**(9): p. 3155-3172.
75. G. J. McIntosh, *Theoretical investigations into the nucleation of silica growth in basic solution part II - derivation and benchmarking of a first principles kinetic model of solution chemistry.* Physical Chemistry Chemical Physics, 2013. **15**(40): p. 17496-17509.
76. S. A. Pelster, B. Weimann, B. B. Schaack, W. Schrader, F. Schüth, *Dynamics of silicate species in solution studied by mass spectrometry with isotopically labeled compounds.* Angew Chem Int Ed Engl, 2007. **46**(35): p. 6674-7.
77. N. Ingri, *Equilibrium Studies of Polyanions .4. Silicate Ions in NaCl Medium.* Acta Chemica Scandinavica, 1959. **13**(4): p. 758-775.
78. N. Ingri and G. Schorsch, *On Determination of Formation Constants of $GeO_2(OH)_2^{2-}$ Using a Hydrogen-Electrode - Measurements in 3 M Na(Cl)-Medium.* Acta Chemica Scandinavica, 1963. **17**(3): p. 590-&.
79. P. Becker and B.A. Bilal, *High-Pressure High-Temperature Cell for Potentiometric Measurement in Aqueous-Electrolyte Solutions.* Fresenius Zeitschrift Fur Analytische Chemie, 1984. **317**(2): p. 118-120.
80. S. Y . Yang, A. Navrotsky, D. J. Wesolowski, J. A. Pople, *Study on synthesis of TPA-silicalite-1 from initially clear solutions of various base concentrations by in situ calorimetry, potentiometry, and SAXS.* Chemistry of Materials, 2004. **16**(2): p. 210-219.
81. G. J. McIntosh, *A theoretical kinetic model of the temperature and pH dependent dimerization of orthosilicic acid in aqueous solution.* Physical Chemistry Chemical Physics, 2012. **14**(2): p. 996-1013.
82. T. T. Trinh, A. P. J. Jansen, R. A. van Santen, E. J. Meijer, *Role of Water in Silica Oligomerization.* Journal of Physical Chemistry C, 2009. **113**(7): p. 2647-2652.
83. A. Szabo, N.S. Ostlund, *Modern quantum chemistry: Introduction to advanced electronic structure theory*. 1989: Dover Publications Inc. 480.
84. A. D. Becke, *Density-Functional Thermochemistry .3. The Role of Exact Exchange.* Journal of Chemical Physics, 1993. **98**(7): p. 5648-5652.
85. J. Tomasi, B. Mennucci, and R. Cammi, *Quantum mechanical continuum solvation models.* Chemical Reviews, 2005. **105**(8): p. 2999-3093.
86. J. D. H. Strickland, *The Preparation and Properties of Silicomolybdic Acid .1. The Properties of Alpha-Silicomolybdic Acid.* Journal of the American Chemical Society, 1952. **74**(4): p. 862-867.
87. J. D. H. Strickland, *The Preparation and Properties of Silicomolybdic Acid .2. The Preparation and Properties of Beta-Silicomolybdic Acid.* Journal of the American Chemical Society, 1952. **74**(4): p. 868-871.
88. J. D. H. Strickland, *The Preparation and Properties of Silicomolybdic Acid .3. The Combination of Silicate and Molybdate.* Journal of the American Chemical Society, 1952. **74**(4): p. 872-876.
89. G. Engelhardt, W. Altenburg, D. Hoebbel, W. Wieker, *29Si-NMR-Spektroskopiea n Silicatlosungen. IV [l] Untersuchungen zur Kondensation der Monokieselsaure 121*. Z. anorg. allg. Chem., 1977. **428**: p. 43-52.
90. G. Engelhardt, H. Jancke, *Strukturuntersuchungen an Silikatanionen in wäßriger Lösung mit Hilfe der 29 Si-NMR-Spektroskopie.* Z.Chem, 1974. **14**(3): p. 109-110.
91. G. Engelhardt and D. Michel, *High-resolution solid-state NMR of silicates and zeolites*. 1987, Chichester West Sussex ; New York: Wiley. xiv, 485 p.

92. R. E. Mesmer, C.F. Baes, and F.H. Sweeton, *Acidity Measurements at Elevated Temperature .4. Apparent Dissociation Product of Water in 1M Potassium Chloride up to 292 Degrees.* Journal of Physical Chemistry, 1970. **74**(9): p. 1937-&.
93. R. E. Mesmer, W. L. Marschall, D. A. Palmer, J. M. Simonson, H. F. Holmes, *Thermodynamics of Aqueous Association and Ionization Reactions at High-Temperatures and Pressures.* Journal of Solution Chemistry, 1988. **17**(8): p. 699-718.
94. R. E. Mesmer, D. A. Palmer, J. M. Simonson, H. F. Holmes, P. C. Ho, D. J. Wesolowski, M. S. Gruszkiewicz, *Experimental studies in high temperature aqueous chemistry at Oak Ridge National Laboratory.* Pure and Applied Chemistry, 1997. **69**(5): p. 905-914.
95. J. O'M. Bockris, D.M. Drazic, *Electrochemical Science*. 1972, London: Taylor and Francis Ltd.
96. S. N. Lvov, X.Y. Zhou, and D.D. Macdonald, *Flow-through electrochemical cell for accurate pH measurements at temperatures up to 400°C.* Journal of Electroanalytical Chemistry, 1999. **463**(2): p. 146-156.
97. P. W. Atkins and J. De Paula, *The elements of physical chemistry*. 2005: Oxford University Press New York, NY, USA:.
98. R. G. Kelly, S.J.R., Shoesmith D. W., Buchheit R. G., , *Electrochemical Techniques in Corrosion Science and Engineering*. 1st ed. 2003, New York, Basel: Marcel Dekker Inc.
99. I. L. Rozenfeld, *Corrosion Inhibitors*. 1981: Mcgraw-Hill Inc.
100. M. Pourbaix, *Atlas of Electrochemical Equilibria in Aqueous Solutions*. 1966: NACE International.
101. G. Wulfsberg, *Inorganic Chemistry*. 2000: University Science Books.
102. M. T. Weller, O.T.L., Rourke J. P., Armstrong F. A., , *Inorganic Chemistry*. 2010: Oxford University Press.
103. L. L. Olson and C.R. Omelia, *Interactions of Fe(III) with $Si(OH)_4$.* Journal of Inorganic & Nuclear Chemistry, 1973. **35**(6): p. 1977-1985.
104. H. C. B. Hansen, B. Rabenlange, K. Raulundrassmussen, O. K., Borggaard *Monosilicate Adsorption by Ferrihydrite and Goethite at pH 3-6.* Soil Science, 1994. **158**(1): p. 40-46.
105. H. C. B. Hansen, H.C.B., B. Rabenlange, K. Raulundrassmussen, O. K., Borggaard, *Stability-Constants for Silicate Adsorbed to Ferrihydrite.* Clay Minerals, 1994. **29**(3): p. 341-350.
106. N. S. Jacobson, E. J. Opila, D. L. Myers, E. H. Copland, *Thermodynamics of gas phase species in the Si–O–H system.* The Journal of Chemical Thermodynamics, 2005. **37**(10): p. 1130-1137.
107. E. J. Opila, D.S. Fox, and N.S. Jacobson, *Mass spectrometric identification of Si-O-H(g) species from the reaction of silica with water vapor at atmospheric pressure.* Journal of the American Ceramic Society, 1997. **80**(4): p. 1009-1012.
108. W. R. Wilcox, *preparation and properties of solid state materials*. Vol. 2. 1976: Marcel Dekker Inc.
109. G. Sauerbrey, *Verwendung Von Schwingquarzen Zur Wagung Dunner Schichten Und Zur Mikrowagung.* Zeitschrift Fur Physik, 1959. **155**(2): p. 206-222.
110. C. Lu, and A.W. Czanderna, *Applications of piezoelectric quartz crystal microbalances*. 2012: Elsevier.
111. M. J. T. Frisch, G. W.; Schlegel, H. B.; Scuseria, G. E.; Robb, M. A.; Cheeseman, J. R.; Scalmani, G.; Barone, V.; Mennucci, B.; Petersson, G. A.; Nakatsuji, H.; Caricato, M.; Li, X.; Hratchian, H. P.; Izmaylov, A. F.; Bloino, J.; Zheng, G.; Sonnenberg, J. L.; Hada, M.; Ehara, M.; Toyota, K.; Fukuda, R.; Hasegawa, J.; Ishida, M.; Nakajima, T.; Honda, Y.; Kitao, O.; Nakai, H.; Vreven, T.; Montgomery, J. A., Jr.; Peralta, J. E.;

Ogliaro, F.; Bearpark, M.; Heyd, J. J.; Brothers, E.; Kudin, K. N.; Staroverov, V. N.; Kobayashi, R.; Normand, J.; Raghavachari, K.; Rendell, A.; Burant, J. C.; Iyengar, S. S.; Tomasi, J.; Cossi, M.; Rega, N.; Millam, J. M.; Klene, M.; Knox, J. E.; Cross, J. B.; Bakken, V.; Adamo, C.; Jaramillo, J.; Gomperts, R.; Stratmann, R. E.; Yazyev, O.; Austin, A. J.; Cammi, R.; Pomelli, C.; Ochterski, J. W.; Martin, R. L.; Morokuma, K.; Zakrzewski, V. G.; Voth, G. A.; Salvador, P.; Dannenberg, J. J.; Dapprich, S.; Daniels, A. D.; Farkas, Ö.; Foresman, J. B.; Ortiz, J. V.; Cioslowski, J.; Fox, D. J., *Gaussian 09, Revision D.01*. 2009, Gaussian, Inc.: Wallingford CT.

112. J. C. G. Pereira, C.R.A. Catlow, and G.D. Price, *Ab initio studies of silica-based clusters. Part I. Energies and conformations of simple clusters.* Journal of Physical Chemistry A, 1999. **103**(17): p. 3252-3267.
113. J. C. G. Pereira, C.R.A. Catlow, and G.D. Price, *Ab initio studies of silica-based clusters. Part II. Structures and energies of complex clusters.* Journal of Physical Chemistry A, 1999. **103**(17): p. 3268-3284.
114. R. Cole, *Electrospray Ionization Mass Spectrometry-Fundamentals, Instrumentation and Applications*, ed. R. Cole. 1997: John Wiley and Sons.
115. S. N. Lvov, X. Y. Zhou, G. C. Ulmer, H. L. Barnes, D. D. Macdonald, S. M. Ulyanov, L. G. Benning, D. E. Grandstaff, M. Manna, E. Vicenzi, *Progress on yttria-stabilized zirconia sensors for hydrothermal pH measurements.* Chemical Geology, 2003. **198**(3-4): p. 141-162.
116. S. N. Lvov, X. Y. Zhou, S. M. Ulyanov, A. V. Bandura , *Reference systems for assessing viability and accuracy of pH sensors in high temperature subcritical and supercritical aqueous solutions.* Chemical Geology, 2000. **167**(1-2): p. 105-115.
117. D. J. Pickett and K.L. Ong, *Influence of Hydrodynamic and Mass-Transfer Entrance Effects on Operation of a Parallel Plate Electrolytic Cell.* Electrochimica Acta, 1974. **19**(12): p. 875-882.
118. A. Frias-Ferrer, J. Gonzales-Carcia, V. Saez, C. Ponce de Leon, E. C. Walsh, *The effects of manifold flow on mass transport in electrochemical filter-press reactors.* Aiche Journal, 2008. **54**(3): p. 811-823.
119. R. C. Alkire and R.D. Braatz, *Etectrochemical engineering in an age of discovery and innovation.* Aiche Journal, 2004. **50**(9): p. 2000-2007.
120. G. Naren, H. Ohashi, Y. Okaue, T. Yokoyama, *Adsorption kinetics of silicic acid on akaganeite.* Journal of Colloid and Interface Science, 2013. **399**: p. 87-91.
121. F. Hazel, R.U. Schock, and M. Gordon, *Interaction of Ferric Ions with Silicic Acid.* Journal of the American Chemical Society, 1949. **71**(6): p. 2256-2257.
122. P. J. Swedlund, G.M. Miskelly, and A.J. McQuillan, *An attenuated total reflectance IR study of silicic acid adsorbed onto a ferric oxyhydroxide surface.* Geochimica Et Cosmochimica Acta, 2009. **73**(14): p. 4199-4214.
123. P. J. Swedlund and J.G. Webster, *Adsorption and polymerisation of silicic acid on ferrihydrite, and its effect on arsenic adsorption.* Water Research, 1999. **33**(16): p. 3413-3422.
124. J. D. Russell, *Infrared Spectroscopy of Ferrihydrite - Evidence for the Presence of Structural Hydroxyl-Groups.* Clay Minerals, 1979. **14**(2): p. 109-114.
125. Y. S. Li, J.S. Church, and A.L. Woodhead, *Infrared and Raman spectroscopic studies on iron oxide magnetic nano-particles and their surface modifications.* Journal of Magnetism and Magnetic Materials, 2012. **324**(8): p. 1543-1550.
126. M. Saheb, M. Descostes, D. Neff, H. Matthiesen, A. Michelin, P. Dillmann, *Iron corrosion in an anoxic soil: Comparison between thermodynamic modelling and ferrous archaeological artefacts characterised along with the local in situ geochemical conditions.* Applied Geochemistry, 2010. **25**(12): p. 1937-1948.

127. RRUFF. *Goethite Raman Spectral Data*. 2015; Available from: http://rruff.info/Goethite/R120086.
128. RRUFF. *hematite data Raman*. 2015; Available from: http://rruff.info/Hematite.
129. A. V. Bandura and S.N. Lvov, *The ionization constant of water over wide ranges of temperature and density*. Journal of Physical and Chemical Reference Data, 2006. **35**(1): p. 15-30.

7 Appendix

7.1 Linear fitting of solubility data determined by the UV-Vis method

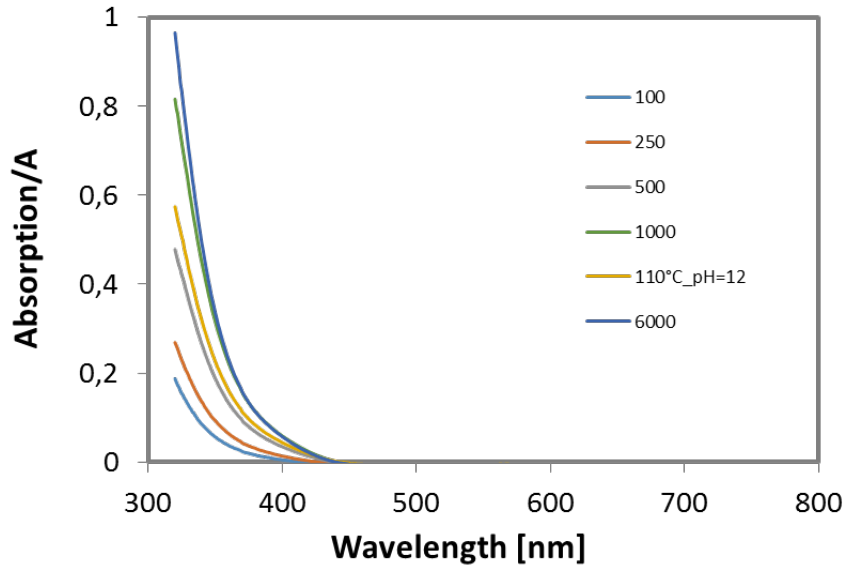

Figure 7-1 – UV-Vis spectrum of diluted calibrated solutions (solution F) and sample solution at 110°C at pH=12

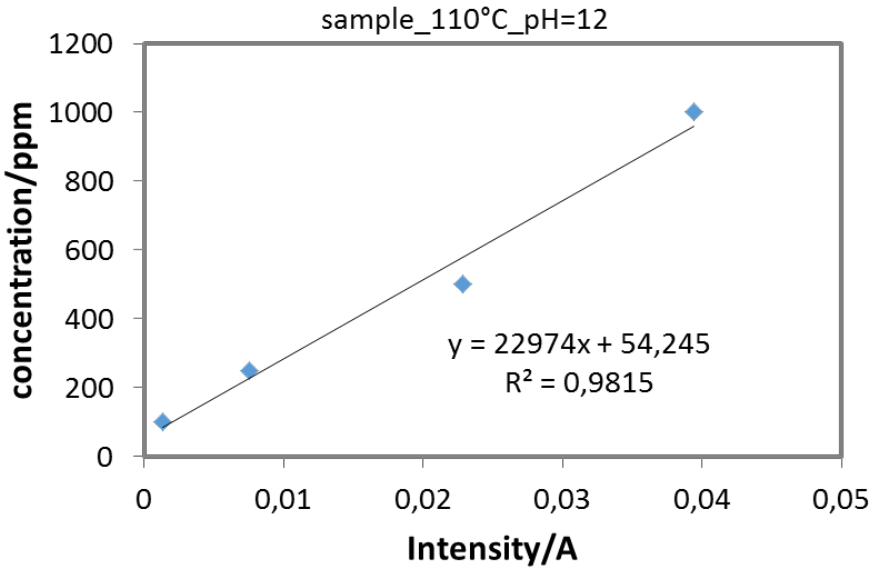

Figure 7-2 – The concentration (y-axis) of the calibrated solution for different intensities (x-axis) at 410nm showing a linear dependency

The fitting curves are given in the form of

$a_{UV\text{-}VIS,\,pH} = m_{UV\text{-}VIS,\,pH}\, b_{UV\text{-}VIS,pH} + c_{UV\text{-}VIS,\,pH}$

Table 7-1 – The fitting parameters for the UV-Vis measurement to determine the concentration of dissolved silica (silicic acid).

pH	07	12	13
$b_{UV\text{-}VIS,pH}$	$lnK_{,sol}$	$lnK_{,sol}$	$lnK_{,sol}$
$m_{UV\text{-}VIS,pH}$	-1.878	-1.580	-0.627
$b_{UV\text{-}VIS,pH}$	1/T	1/T	1/T
$c_{UV\text{-}VIS,\,pH}$	-0.624	-0.707	-1.474

7.2 Corrosion effects

7.2.1 Tafel plots

No silica

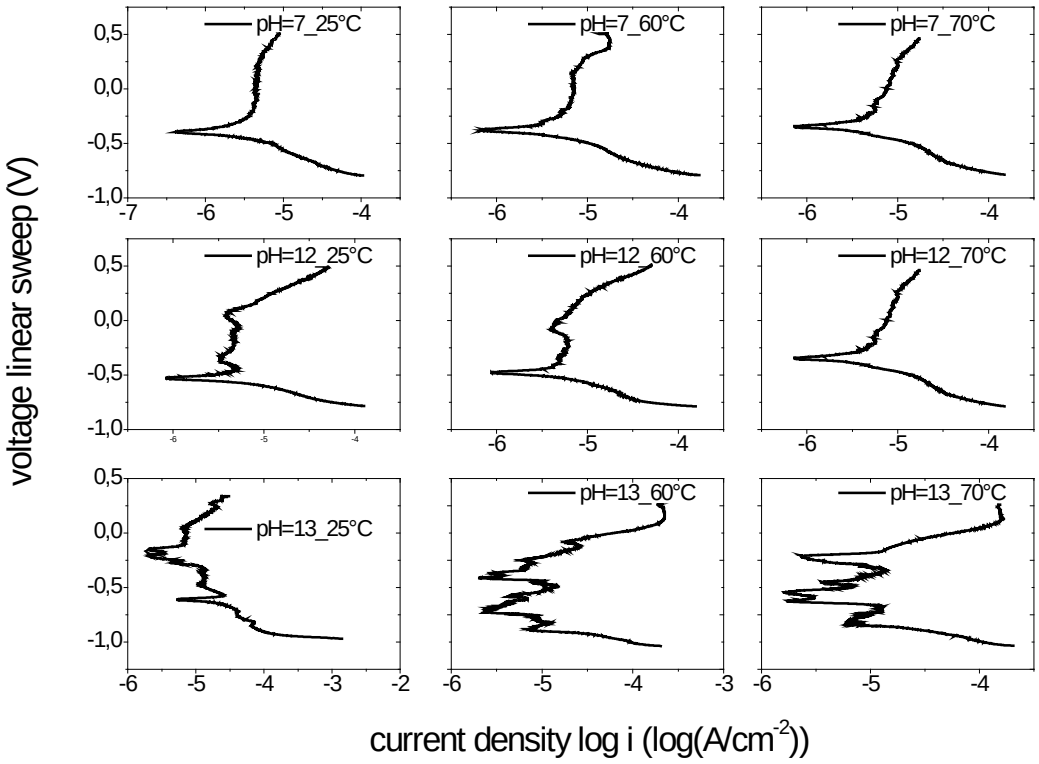

Figure 7-3 - The linear sweep measurements in the absence of dissolved silica at different temperatures and pH.

With silica

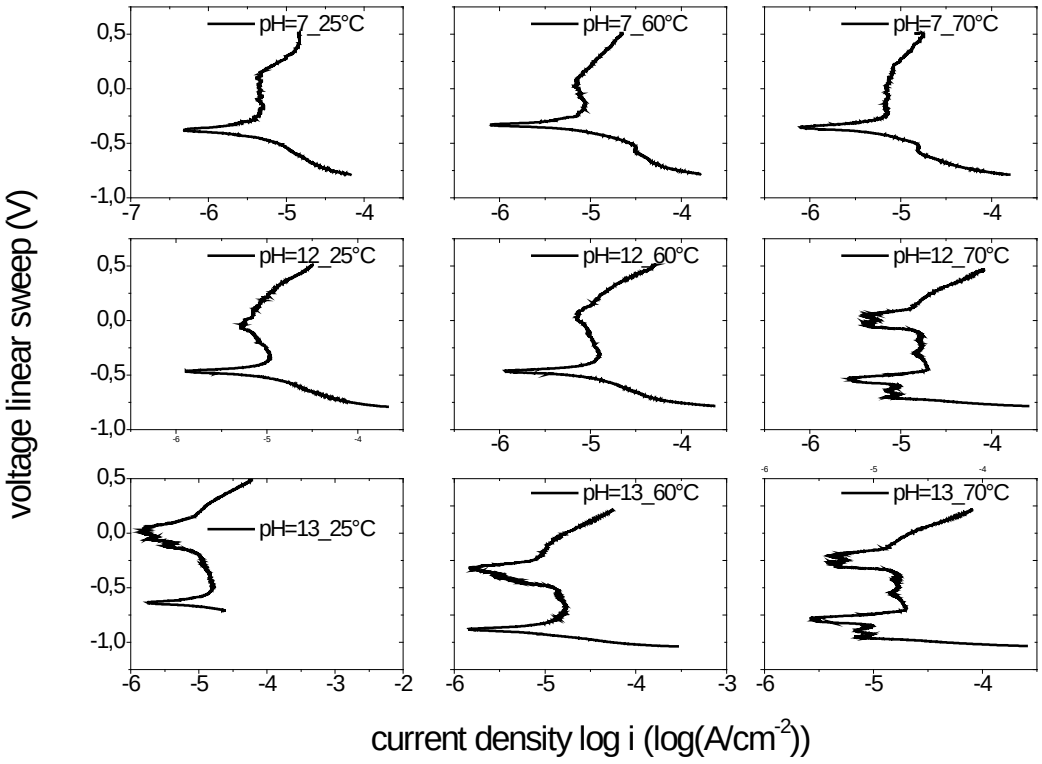

Figure 7-4– The linear sweep measurement in the presence of silica at different temperatures and pH.

7.2.2 Corrosion model

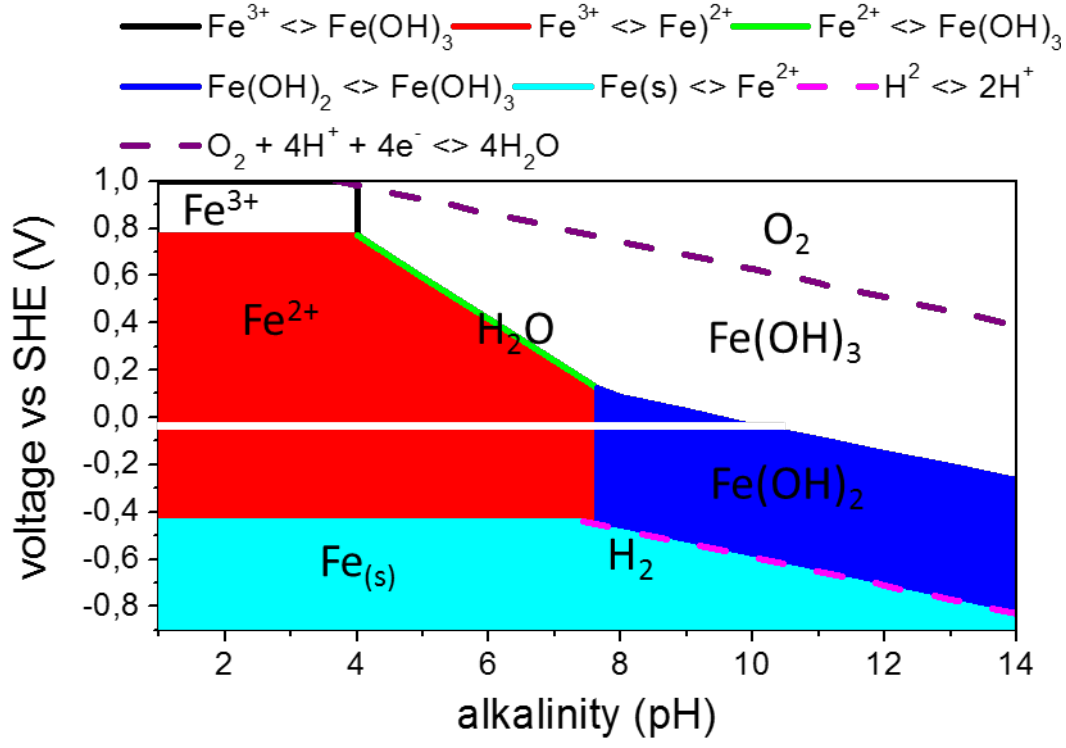

Figure 7-5 – The Pourbaix Diagram of iron

The initial molar concentrations are determined:

$$n_{H_2} = 1 + 2\Delta n_{H^+}; \qquad x_{H_2} = \frac{1 + 2\Delta n_{H^+}}{n_{SUM}}$$ Equation 7-1

$$n_{H^+} = \Delta n_{H^+}; \qquad x_{H^+} = \frac{\Delta n_{H^+}}{n_{SUM}}$$ Equation 7-2

$$n_{Fe^{2+}} = 3\Delta n_{H^+} \qquad x_{Fe^{2+}} = \frac{3\Delta n_{H^+}}{n_{SUM}}$$ Equation 7-3

$$n_{OH^-} = \Delta n_{OH^-} \approx 0; \qquad x_{OH^-} = \frac{\Delta n_{OH^-}}{n_{SUM}}$$ Equation 7-4

The OH^- does not play a significant role in the charge transfer on the stainless steel and hence neglected.

$$n_{H_2O} = 1 - \left(0.25\Delta n_{OH^-} + \left(1 - \Delta n_{H^+}\right)\right); \qquad x_{H_2O} = \frac{1 - \left(0.25\Delta n_{OH^-} + \left(1 - \Delta n_{H^+}\right)\right)}{n_{SUM}}$$

Equation 7-5

$$n_{H_4SiO_4} = \Delta n_{H_4SiO_4}\left(UV - Vis\right); \qquad x_{H_4SiO_4} = \frac{n_{H_4SiO_4}}{n_{SUM}}$$ Equation 7-6

$$n_{SUM} = 2 + 5\Delta n_{H^+} + 0.75\Delta n_{OH^-}$$ Equation 7-7

$$K_{H^+} = \frac{\left(x_{H^+}\right)^2}{x_{H_2}} = \frac{\left(\Delta n_{H^+}\right)^2}{\left(1 + 2\Delta n_{H^+}\right)\left(2 + 5\Delta n_{H^+} + 0.75\Delta n_{OH^-}\right)}$$ Equation 7-8

$$K_{Fe^{2+}} = \frac{\left[Fe^{2+}\right]}{\left[Fe\right]} = x_{Fe^{2+}} = \frac{3\Delta n_{H^+}}{2 + 5\Delta n_{H^+} + 0.75\Delta n_{OH^-}}$$ Equation 7-9

$$K_{Fe(OH)_3} = \frac{\left[Fe(OH)_3\right]\left[H^+\right]^3}{\left[Fe^{2+}\right]\left[H_2O\right]^3} = \frac{\left(x_{H^+}\right)^3}{3\left(x_{Fe^{2+}}\right)\times\left(x_{H_2O}\right)^3}$$

$$= \frac{\left(\Delta n_{H^+}\right)^3\left(2+5\Delta n_{H^+}+0.75\Delta n_{OH^-}\right)}{\left(3\Delta n_{H^+}\right)\times\left(1-0.25\Delta n_{OH^-}+\Delta n_{H^+}\right)^3}$$

Equation 7-10

With H^+_2 being 1 or 10^{-7} and $K_{H2O} = 10^{-14}$

$$K_{DISS,H_2O} = \frac{\left[H^+\right]_1\left[OH^-\right]_1}{\left[H_2O\right]_1}$$

Equation 7-11

Table 7-2 – The OH^- concentration for hydrogen concentration in half-cell 2 of unity on the right and 10^{-7} on the left (values with silica)

		OH^- concentration			OH^- concentration		
T/°C	$K_{DISS,H2O}$	pH=7	pH=12	pH=13	pH=7	pH=12	pH=13
25	1.23×10^{-14}	8.25×10^{-8}	8.82×10^{-8}	9.33×10^{-8}	8.25×10^{-15}	8.82×10^{-15}	9.33×10^{-15}
60	5.50×10^{-14}	3.70×10^{-7}	1.67×10^{-7}	1.53×10^{-7}	3.70×10^{-14}	1.67×10^{-14}	1.53×10^{-14}
70	2.00×10^{-13}	1.35×10^{-6}	4.48×10^{-7}	3.89×10^{-7}	1.35×10^{-13}	4.48×10^{-14}	3.89×10^{-14}
110	5.62×10^{-13}	3.84×10^{-6}	4.36×10^{-7}	3.43×10^{-7}	3.84×10^{-13}	4.36×10^{-14}	3.43×10^{-14}
130	1.15×10^{-12}	7.88×10^{-6}	5.94×10^{-7}	4.53×10^{-7}	7.88×10^{-13}	5.94×10^{-14}	4.53×10^{-14}
150	2.29×10^{-12}	1.58×10^{-5}	8.45×10^{-7}	6.90×10^{-7}	1.58×10^{-12}	8.45×10^{-14}	6.90×10^{-14}
170	3.47×10^{-12}	2.41×10^{-5}	9.65×10^{-7}	7.90×10^{-7}	2.41×10^{-12}	9.65×10^{-14}	7.90×10^{-14}

Table 7-3 – The Fe^{2+} concentration for hydrogen concentration in half-cell 2of unity on the right and 10^{-7} on the left (values with silica)

	Fe^{2+} concentration=$3H^+$			Fe^{2+} concentration=$3H^+$		
T/°C	pH=7	pH=12	pH=13	pH=7	pH=12	pH=13
25	4.48×10^{-7}	4.19×10^{-7}	$3,96 \times10^{-7}$	4.48	4.19	3.96
60	4.45×10^{-7}	9.86×10^{-7}	1.08×10^{-6}	4.45	9.86	10.79
70	4.44×10^{-7}	1.34×10^{-6}	1.54×10^{-6}	4.44	13.36	15.40
110	4.40×10^{-7}	3.87×10^{-6}	4.92×10^{-6}	4.40	38.68	49.18
130	4.37×10^{-7}	5.80×10^{-6}	7.61×10^{-6}	4.37	58.00	76.11
150	4.34×10^{-7}	8.13×10^{-6}	9.97×10^{-6}	4.34	81.31	99.67
170	4.32×10^{-7}	1.08×10^{-5}	1.32×10^{-5}	4.32	107.79	131.75

7.3 Water sorption results – for LUDOX AS 40

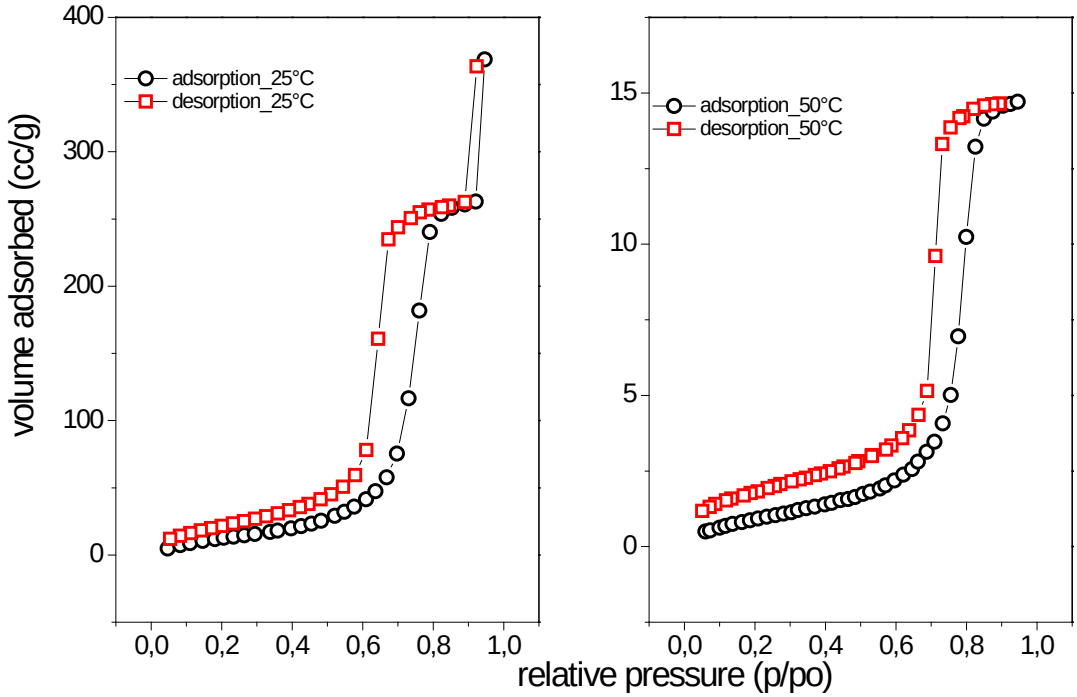

Figure 7-6 – Water sorption results for LUDOX AS-40 at 25°C and 50°C.

7.4 XRD data of LUDOX AS-40

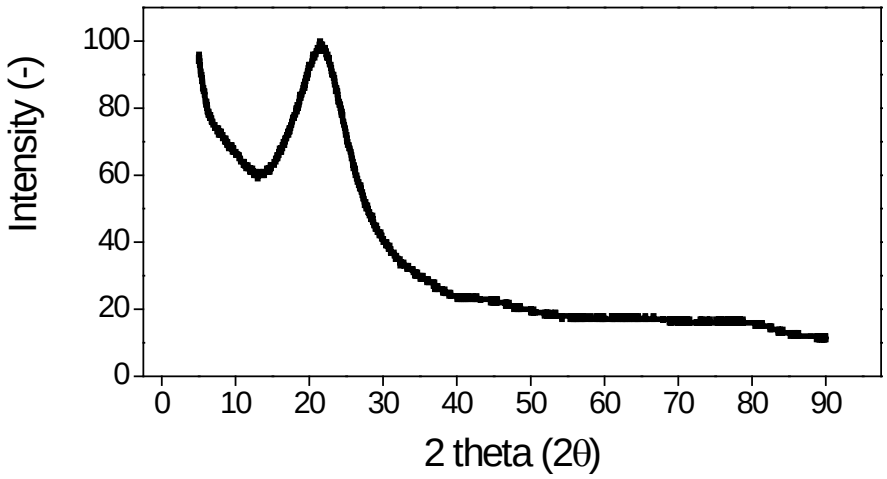

Figure 7-7 – The X-ray diffraction pattern for LUDOX AS-40.

7.5 Fitting equations from ESI-MS Data

Table 7-4 – The fitting equations retrieved from the ESI-MS data of the silicic acid species considered.

Species, i	pH=7	pH=12	pH=13
	$FIT_i = \bar{a} \times exp\ \frac{\bar{b}}{T}$ / [-]	$FIT_i = \bar{a} \times exp\ \frac{\bar{b}}{T}$ / [-]	$FIT_i = \bar{a} \times exp\ \frac{\bar{b}}{T}$ / [-]
Disilicic acid	$\bar{a}$ =231.84 $\bar{b}$ =-1493	$\bar{a}$ =3600.3 $\bar{b}$ =-2973	$\bar{a}$ =885.56 $\bar{b}$ =-1395
Cyclotrisilicic acid	$\bar{a}$ =644.63 $\bar{b}$ =-2284	$\bar{a}$ =0.029 $\bar{b}$ =1796.7	$\bar{a}$ =0.2762 $\bar{b}$ =434.79
Trisilicic acid	$\bar{a}$ 2x10^{-5} $\bar{b}$ =3425.5	$\bar{a}$ =0.0016 $\bar{b}$ =1083.8	$\bar{a}$ =0.0418 $\bar{b}$ =1842
Cyclotrisilicic acid	$\bar{a}$ =0.0048 $\bar{b}$ =2691.1	$\bar{a}$ =0.0823 $\bar{b}$ =1402	$\bar{a}$ =0.0071 $\bar{b}$ =1928.8
Tetrasilicic acid	$\bar{a}$ =4071.4 $\bar{b}$ =-2680	$\bar{a}$ =138.81 $\bar{b}$ =1480	$\bar{a}$ =142.44 $\bar{b}$ =-1384
Cyclopentasilicic acid	$\bar{a}$ =27.036 $\bar{b}$ =-827.5	$\bar{a}$ =4892.9 $\bar{b}$ ==-3049	$\bar{a}$ =68118 $\bar{b}$ =-3104
Pentasilicic acid	$\bar{a}$ =721.52 $\bar{b}$ =-1730	$\bar{a}$ =24.603 $\bar{b}$ =-519.3	$\bar{a}$ =391.36 $\bar{b}$ =-1206
Cyclohexasilicic acid	$\bar{a}$ =16.051 $\bar{b}$ =-645.8	$\bar{a}$ =46.025 $\bar{b}$ =-1102	$\bar{a}$ =58.709 $\bar{b}$ =-1386
Hexasilicic acid	$\bar{a}$ =2522.9 $\bar{b}$ =-1619	$\bar{a}$ =119.42 $\bar{b}$ =-726.6	$\bar{a}$ =14384 $\bar{b}$ =-2756
Cycloheptasilicic acid	$\bar{a}$ =118.91 $\bar{b}$ =-1569	$\bar{a}$ =114783 $\bar{b}$ =-4168	$\bar{a}$ =128.83 $\bar{b}$ =-1487
Heptasilicic acid	$\bar{a}$ =1179.7 $\bar{b}$ =-189.3	$\bar{a}$ =157897 $\bar{b}$ =-3563	$\bar{a}$ =382.68 $\bar{b}$ =-996.7
Octahydroxyoctasilse-quioxane	$\bar{a}$ =53.476 $\bar{b}$ =-1090	$\bar{a}$ =38.746 $\bar{b}$ =-878.8	$\bar{a}$ =69.716 $\bar{b}$ =-1513
Octasilicic acid	$\bar{a}$ =48.157 $\bar{b}$ =-1023	$\bar{a}$ =1x10^{6} $\bar{b}$ =-4903	$\bar{a}$ =1931.5 $\bar{b}$ =-1379

7.6 Images of corrosion of high temperature cell and glass cell stainless steel electrodes

Figure 7-8 – The SEM samples from the high temperature flow-through cell

Figure 7-9 – The SEM and EDX samples of stainless steel from the glass cell.

7.7 VLE Calculation Data

Table 7-5 – The Vapour-Liquid compositions for silicic acid-H_2O for different temperatures at pH=7. Feed composition is given in the last column.

pH=7					
Temperature/°C	x_1	y_1	x_2	y_2	z_1
25	6.7E-06	0.0011	0.99999	0.99887	0.00054
60	1.6E-05	0.0017	0.99998	0.99827	0.00083
70	2.0E-05	0.0019	0.99998	0.99805	0.00094
110	5.2E-05	0.0031	0.99994	0.99686	0.0015
130	8.4E-05	0.0040	0.99991	0.99601	0.0020
150	0.00014	0.0050	0.99986	0.99494	0.0025
170	0.00021	0.0064	0.99978	0.99360	0.0032

Table 7-6 – The Vapour-Liquid compositions for silicic acid-H_2O for different temperatures at pH=12. Feed composition is given in the last column.

pH=12					
Temperature/°C	x_1	y_1	x_2	y_2	z_1
25	4.1-05	0.0028	0.99995	0.99723	0.0013
60	9.2E-05	0.0042	0.99990	0.99583	0.0020
70	0.00011	0.0047	0.99988	0.99532	0.0023
110	0.00030	0.0074	0.99970	0.992603	0.0037
130	0.00046	0.0093	0.99953	0.99072	0.0047
150	0.00073	0.0116	0.99927	0.98839	0.0060
170	0.00113	0.0144	0.99886	0.98552	0.0076

Table 7-7 – The Vapour-Liquid compositions for silicic acid-H_2O for different temperatures at pH=13. Feed composition is given in the last column.

pH=13					
Temperature/°C	x_1	y_1	x_2	y_2	z_1
25	0.0038	0.0261	0.99623	0.97381	0.0146
60	0.0050	0.0302	0.99498	0.9697	0.0172
70	0.0054	0.0314	0.99455	0.96855	0.0180
110	0.0075	0.0369	0.99249	0.96309	0.0218
130	0.0088	0.0399	0.99121	0.9600	0.0239
150	0.0102	0.0431	0.98973	0.95680	0.0263
170	0.0120	0.0466	0.98803	0.95331	0.0289

7.8 Formation and reaction energies from quantum chemical calculations

Table 7-8 - The values below are the energies for all silicic acid species and water. Geometries are optimized with the B3LYP/6-311G level of theory. These values are used to calculate the energy of reactions for polymerisation and cyclisation.**

mixed (linear and branched-cyclic) see page 22			cyclic (simple and fused) – see page 22	
	$\Delta g^{o}_{f(G09),i}$ /Hartrees	$\Delta h^{o}_{f(G09),i}$ /Hartrees	$\Delta g^{o}_{f(G09),i}$ /Hartrees	$\Delta h^{o}_{f(G09),i}$ /Hartrees
monosilicic acid	-593.086587	-593.048781	-	-
disilicic acid	-1109.733536	-1109.680815	-	-
trisilicic acid	-1626.381212	-1626.316225	-1549.934365	-1549.874724
tetrasilicic acid	-2143.026953	-2142.947543	-2066.148156	-2066.09134
pentasilicic acid	-2583.238726	-2583.156087	-2506.745988	-2506.671466

hexasilicic acid	-3099.898015	-3099.804399	-2946.991042	-2946.905241
heptasilicic acid	-3616.553195	-3616.445545	-3387.134745	-3387.049644
Octasilicic acid	-4133.205845	-4133.086257	-3827.430802	-3827.329914
H_2O	-76.444436	-76.422355	-76.444436	-76.422355

Table 7-9 - The values below are the energies for and water, hydroxonium ion, all neutral and anionic silicic acid species. Geometries are optimized with the B3LYP/6-311G level of theory with solvent effects (PCM). These values are used to calculate the energy of dissociation reactions.**

mixed (linear and branched-cyclic)-see page 22			cyclic (simple and fused)-see page 22	
B3LYP	$\Delta g^{o}_{f(G09),i}$ /Hartrees	$\Delta h^{o}_{f(G09),i}$ /Hartrees	$\Delta g^{o}_{f(G09),i}$ /Hartrees	$\Delta h^{o}_{f(G09),i}$ /Hartrees
monosilicic acid	-593.101292	-593.062539		
monosilicic- acid ion	-592.620828	-592.582731		
disilicic acid	-1109.754497	-1109.701395		
disilicic- acid ion	-1109.281211	-1109.228683		
trisilicic acid	-1626.409443	-1626.34413	-1549.961159	-1549.901419
trisilicic- acid ion	-1625.952471	-1625.888806	-1549.490089	-1549.430774
tetrasilicic acid	-2143.061604	-2142.981733	-2066.618497	-2066.547145
tetrasilicic- acid ion	-2142.600600	-2142.529287	-2066.149061	-2066.081777
pentasilicic acid	-2583.277141	-2583.194233	-2506.777401	-2506.702681
pentasilicic- acid ion	-2582.811945	-2582.728846	-2506.309633	-2506.237261
hexasilicic acid	-3099.898863	-3099.804581	-2947.027521	-2946.94339
hexasilicic acid -ion	-3099.493725	-3099.401965	-2946.564075	-2946.481508
heptasilicic acid	-3616.597325	-3616.490770	-3463.671702	-3463.578445
heptasilicic- acid ion	-3616.141135	-3616.033339	-3463.204412	-3463.113597
Octasilicic acid	-4133.255040	-4133.137172	-3827.430802	-3827.329914
octasilicic- acid ion	-4132.805862	-4132.686038	-3827.0026639	-3826.907405
H_2O	-76.451018	-76.429587	-76.451018	-76.429587
H_3O^+	-76.837885	-76.814934	-76.837885	-76.814934

7.8.1 The comparison of the temperature dependent lnK with the Hoff equation

This section of appendix 7.8.1 compare the temperature dependent equilibrium constant (lnK), the temperature independent equilibrium constant lnK_298.15K) and from classical thermodynamics with the van't Hoff equation. For lnK , d_rh and d_rs are temperature dependent $d_rh(T)$ and $d_rs(T)$

$$\ln K = \frac{\Delta s_{reaction}(T)}{R} - \frac{\Delta h_{reaction}(T)}{RT}$$

For $lnK_{298.15K}$, $dh°_{reaction}$ and $ds°_{reaction}$ are not dependent on temperature

$$\ln K_{298.15K} = \frac{\Delta s^o_{reaction}}{R} - \frac{\Delta h^o_{reaction}}{RT}$$

The van't Hoff equation is identical to $lnK_{298.15K}$ (see derivation below)

$$\ln K_p = -\frac{\Delta g^o_{reaction}}{RT^o} - \frac{\Delta h^o_{reaction}}{R}\left(\frac{1}{T} - \frac{1}{T^o}\right)$$

From the figures below calculated for cyclic trisilicic acid and fused-cyclic pentasilicic acid, the deviation between lnK and the temperature independent equilibrium constant as well as the van't Hoff equation is negligible.

7.8.2 Comparison of lnK, $lnK_{298.15K}$ and lnK_p for cyclic trisilicic (cyclotrisilicic) and fused-cyclic pentasilicic (cyclopentasilicic) acid

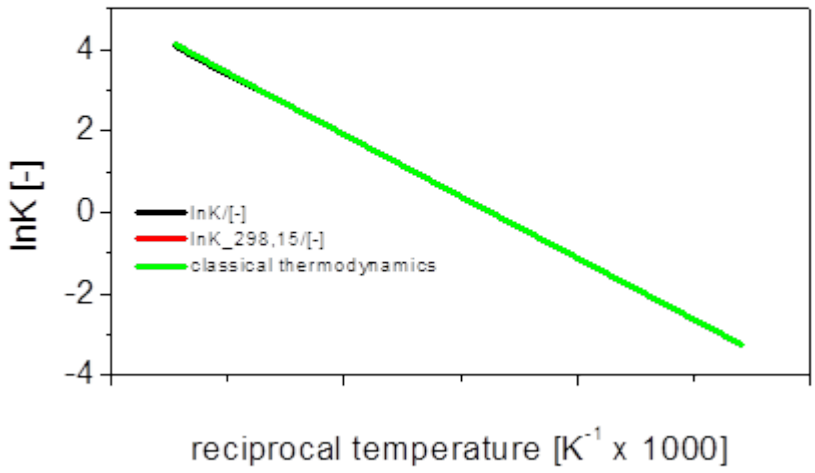

Figure 7-10 – The figure above shows the comparison of lnK, $lnK_{298.15K}$ and lnK_p for cyclic trisilicic acid.

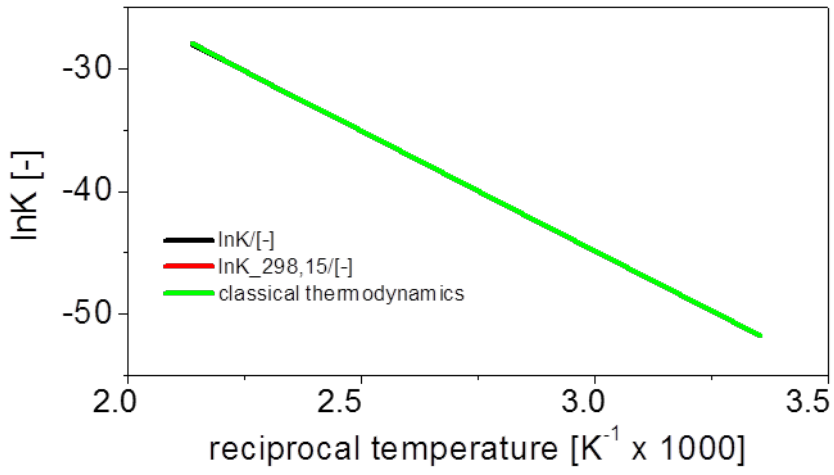

Figure 7-11 – The figure above shows the comparison of lnK, $lnK_{298.15K}$ and lnK_p for cyclopentasilicic acid.

7.8.3 Derivation of the second law from the van't Hoff equation

Assumption: enthalpy and free energy of reaction are considered and are not temperature dependent and only standard enthalpy and free energy of reaction are considered. The equilibrium constant at standard state is directly related to the Gibbs free energy:

$$\ln K_p^o = -\frac{\Delta g_{reaction}^o}{RT^o}$$

In addition, the van't Hoff equation is given from the Gibbs Helmholtz equation as follows:

$$\ln K_p = -\frac{\Delta g_{reaction}^o}{RT^o} - \frac{\Delta h_{reaction}^o}{R}\left(\frac{1}{T} - \frac{1}{T^o}\right)$$

Substituting the $d_r g° = d_r h° - T° d_r s°$

$$\ln K_p = -\frac{\left(\Delta h_{reaction}^o - T^o \Delta s_{reaction}^o\right)}{RT^o} - \frac{\Delta h_{reaction}^o}{R}\left(\frac{1}{T} - \frac{1}{T^o}\right)$$

$$\ln K_p = -\frac{\left(\Delta h_{reaction}^o\right)}{RT^o} + \frac{T^o \Delta s_{reaction}^o}{RT^o} - \frac{\Delta h_{reaction}^o}{RT} + \frac{\Delta h_{reaction}^o}{RT^o}$$

$$\ln K_p = \frac{\Delta s_{reaction}^o}{R} - \frac{\Delta h_{reaction}^o}{RT}$$

8 Nomenclature

Description	Definition	Dimensions
g	Gibbs energy	J/mol or Hartrees
$g_{(G09)}$	Gibbs energy from quantum chemical calculations	Hartrees
s	Entropy	J/mol x K
$s_{(G09)}$	Entropy from quantum chemical calculations	Hartrees / K
h	enthalpy	J/mol or Hartrees

$h_{(G09)}$	enthalpy from quantum chemical calculations	Hartrees
ξ	Reaction coordinate	-
T	Temperature	Kelvin. K
ϑ	Temperature	°C
p	Pressure	Pa or kPa or bar or N/m²
μ	Chemical potential	-
x	Molar fraction-liquid phase	-
y	Molar fraction-vapour phase	-
$[]$	Concentration of arbitrary component	mol/L
A	Activity of an arbitrary chemical component	-
pH	Logarithm of hydrogen concentration in a solution	$-\log([H^+])$
n_{Al_2O}	Amount of alumina as precursor in moles	moles
$n_{Al_2O_3}$	Amount of alumina as zeolite in moles	moles
n_{SiO_2}	Amount of silicium dioxide as precursor and zeolite in moles	moles
$n_{H2O,ZEO}$	Amount of water in the zeolite structure in moles	moles
n_M	Amount of metal precursor as in moles	moles
n_{OR}	Amount of template as precursor in moles	moles
n_{H_2O}	Amount of water in mole	moles
$linear,i$	Arbitrary mixed (linear and branched-cyclic) silicic acid species with i=1 to 4	
$branched,i$	Arbitrary branched-cyclic	

	silicic acid species with i=5 to 8	
$cyclic,i$	Arbitrary cyclic –(simple and fused) silicic acid species with i=3 to 8	
$mixed,i$	Arbitrary mixed (linear and branched-cyclic) silicic acid species with i=1 to 8	
$Si(OH)_4$	Monosilicic acid	
$silicic\,acid$	Arbitrary silicic acid species	
OR	Organic template	-
M	metal in zeolite structure	-
Si	Silicon or silicic acid abbreviation	-
m	Mixture property	-
R	Ideal Gas constant = 8.31452 J/mol x K	J/mol x K
K	Equilibrium constant	a.u.
υ	Charge of anion or cation	-
ν	stoichiometric coefficient	-
ξ	extent of reaction	mol
E	Potential	V or mV
$E°$	Standard Potential	V or mV
Q	Reaction quotient	a.u.
eps	Convergence criteria	a.u.
z	Number of electrons	-
F	Faradays constant=96485	C/mol
H	Hamiltonian of Schrödingers equation	a.u.
Φ	Wave function	
$\hat{E}$	Energy from quantum chemistry	
$lnFIT$	Fitting equation for data of	a.u.

	silicic acid equilibrium constants from ESI-MS results	
$ln\,\overline{a}$	Fitting parameter-y intercept	a.u.
$ln\,\overline{b}$	Fitting parameter-slope	a.u.
$\overline{\varepsilon}$	Extinction coefficient Beer Lambert relation	(L/mol) m
$\overline{E}$	Extinction from Beer Lambert relation	-
I	Intensity	a.u. either from UV-Vis or ESI-MS
ε_o	Permittivity of a fluid in vacuum	F/m
γ	Surface tension	Pa s or kg/m s
q	Ionic charge of analyte sample	Coulomb
r_{drop}	Radius of analyte drop with solvent	m
d	Thickness of solution layer	m
v	Molar volume	m^3/mol
n	No.of moles	mol
Counts	Counts of mass spectrum peak	-
Total counts	Total counts of mass spectrum peak	-
f	frequency	Hz or MHz
ln	Natural logarithm	-
$A_{SiO\,2\,,q}$	Surface area of quartz	cm^{-2}
$\rho_{\,SiO2,q}$	Density of quartz	kg/m^3
$\mu_{SiO2,q}$	Shear modulus of quartz	$gcm^{-1}s^{-2}$
f_{res}	Resonance frequency	Hz or MHz
mass	Mass of deposited compound on quartz crystal	kg or g

CS	Calibration solution	-
SS	Sample solution	-
ES	Electrolyte solution	-
WS	Working electrode solution	-
PC	Potentiometric cell/Electrochemical cell	-
AT	Anodic terminal	-
CT	Cathodic terminal	-
LJ	Liquid junction	-
e^-	electron	-
Ox	Oxidised species	-
Red	Reduced species	-
ECP	Electrochemical potential	mV or V
OCP	Open Circuit Potential	mV or V
Δ	Difference of arbitrary value	-

Subscripts

i	ith components in an arbitrary system	-
j	jth components in an arbitrary system	-
N	Max no. of arbitrary components	-
V	vapour	-
L	liquid	-
S	solid	-
D	dissolved	-
mixed	Mixed (linear and branched-cyclic) silicic acid species	-
cyc	Cyclic (simple-cyclic and fused-cyclic species)	-
diss	dissociation	-
reaction	reaction	-
f	formation	-

exp	experimental	-
iter	iteration	-
el	electronic	-
e	electron	-
k	core	-
Rayleigh	Rayleigh limit for charge of droplet	-
o	Vacuum condition	-
Avogadro	Avogadro number	-
R1	Reaction 1 for potentiometric measurements	-
R2	Reaction 2 for potentiometric measurements	-
RC2	Corrosion reaction 2 – evolution of Fe^{3+}	
RC3	Corrosion reaction 3 – deposition of $Fe(OH)_3$	
R3	Reaction 3 for potentiometric measurements	-
K1	Polymerisation reaction for linear species, Si < 3	
K2	Polymerisation reaction for branched-cyclic species, Si>3	
C1	Cyclisation reaction	
D1	Dissociation reaction for mixed (linear and branched-cyclic) species	
D2	Dissociation reaction for cyclic (simple-and fused-cyclic) species	
Si,i	Arbitrary mixed (linear and branched-cyclic) silicic acid species with i=1 to 8	
Si,icyc	Arbitrary cyclic (simple-and	

	fused-cyclic) silicic acid species with i=3 to 8	
total	Total of an arbitrary definition	-
C	Electrochemical cell	-
HC	Half-cell	
1	Half-cell 1	
2	Half-cell 2	
REF	Reference / Working	-
SAM	Sample	
EXP	experiment	
W	Water	-
H^+	Hydrogen ion	-
OH^-	Hydroxyl ion	-
CORR	corrosion	-

Superscripts

o	Standard conditions (p=100000Pa and 298.15K)	-
+	Positively charged	-
-	Negatively charged	-

Figures

Figure 2-1 – The different secondary building units forming different zeolite compounds [30]. 7
Figure 2-2 – The effective pore diameter and appropriate molecules which access the pore passage for aluminosilicates, aluminophosphates [32]. 8
Figure 2-3 – The figure shows the complete depiction of the reaction mechanism during hydrothermal zeolite syntheses [6]..... 10
Figure 2-4 – The simplified version of zeolite syntheses pathway with a synergy of pathways postulated by Cundy and Cox[6] as well as Althoff, Unger, and Schüth [34]..... 11
Figure 2-5 – The flow diagram of this whole work [35, 36]..... 13
Figure 3-1 – A generalised scheme of the relaxation method is depicted above([38]-p.552). 18

Figure 3-2 – A three dimensional view of the pressure, volume, temperature surface of a pure component ([38]-p.6). 19
Figure 3-3 – A simplified sketch to the calculation method of the Vapour Liquid Equilibria (VLE) according to Rachford and Rice [40]. 21
Figure 3-4 – The figure depicts the difference between cyclic (simple-cyclic for Si ≤ 4and fused-cyclic Si > 4) and mixed (linear for Si ≤ 4 and branched-cyclic for Si > 4) species..... 22
Figure 3-5 – The schematic flow of the equilibrium model consisting all reaction pathways and coupled with each other is clarified above. 26
Figure 3-6 – The probable reaction pathways of respective silicic acid species chosen for this work derived according to data from literature is shown above. 28
Figure 3-7 – Figure taken from Tomasi and Menucci for the depiction of the Apparent Surface Charge (ASC) [85]. 30
Figure 3-8 – A simplified scheme of the initial plan to measure silicic acid dissociation and the eventual plan of measuring corrosion in the presence of dissolved silica. 37
Figure 4-1 – The logarithmic equilibrium constants of cyclisation reactions. 48
Figure 4-2 – The logarithmic equilibrium constants of condensation reactions. 50
Figure 4-3 – A possible intermediate reaction mechanism for the condensation and cyclisation reactions. 53
Figure 4-4 – The figure above presents the logarithmic dissociation values for cyclic species determined with the B3LYP method with solvent effects (PCM). 54
Figure 4-5 – The figure above presents the logarithmic dissociation values for mixed (linear and branched-cyclic) species with the B3LYP method with solvent effects (PCM). 56
Figure 4-6 – The schematic drawing of the apparatus for the solubility measurement of amorphous silica at 25°C is shown. 58
Figure 4-7 – The high pressure and temperature apparatus used for the solubility measurements for the liquid phase and detection of vapour phase silicic acid at 60-170°C and pH-values of 7, 12, and 13. 59
Figure 4-8 – The experimental results above is shown for UV-Vis measurements with comparison to literature data [22, 48, 53]. The equation of the linear curves in the diagram for all pH values are shown in the appendix 7.1 with the degree of fitting to the data points..... 61
Figure 4-9 – The species molar fractions of the silicic acid species considered (molar mass given beside shade representation below) for the first (figure above) and second run (figure below) at pH=7 63

Figure 4-10 – The species molar fractions of the silicic acid species considered (molar mass given beside shade representation below) for the first and second runs at pH=12. 64
Figure 4-11 – The species molar fractions of the silicic acid species considered (molar mass given beside shade representation) for the first and second runs at pH=13. 64
Figure 4-12 –– The comparison of the logarithmic total equilibrium constants from UV-Vis (filled symbols) and ESI-MS measurements (crossed symbols). 66
Figure 4-13 – Fitting data prior to the subject of the equilibrium model of figure 3-5 for mixed species. 68
Figure 4-14 – Fitting data prior to the subject of the equilibrium model of figure 3-5 for cyclic species. 68
Figure 4-15 – Fitting data after equilibrium calculation from the model of figure 3-5 for mixed (linear and branched-cyclic) species. 70
Figure 4-16 – Fitting data after equilibrium calculation from the model of figure 3-5 for cyclic species. 71
Figure 4-17 – All logarithmic equilibrium constants for UV-Vis measurements, ESI-MS measurements and calculated values 72
Figure 4-18 – The design of the high temperature electrochemical cell. 74
Figure 4-19 – The simplified schematic diagram of the apparatus used for the determination of the silicic acid dissociation constant. 75
Figure 4-20 – The potential of the electrochemical cell at different pH-values represented by different colours and varying velocities (0, 0.25 and 0.5) of pumping solutions on both half-cells (represented by different symbols). 79
Figure 4-21 – The actual measurement of the potential with dissolved silica in the sample solutions at different pH values is presented. 81
Figure 4-22 – The equilibrium constant after subtraction of the calibration potential for different pH values is shown. The values for pH = 12 is determined via a linear dependency of the potential between pH = 7 and 13. 83
Figure 4-23 – The literature results for the dissociation constant of Busey and Mesmer [42]. 85
Figure 4-24 – Proof of stainless steel corrosion of the reactor due to injection of H_2 from the conducted experiment in this investigation(a) and the formation of ionic iron species, iron hydroxide and iron oxides from Bockris(b, c, d) ([95]-p.260). 86
Figure 4-25 – The schematic representation of the formation of iron oxide deposits as mentioned by Bockris ([95]-p.260). 87

Figure 4-26 – The electrochemical glass cell for the validation of the equilibrium conditions. 88
Figure 4-27-Tafel extrapolation of anodic and cathodic curves to determine the equilibrium concentration. 88
Figure 4-28-The equilibrium corrosion potential in the presence and absence of dissolved silica at ϑ=25°C to 70°C at pH=7 as well as pH=13 89
Figure 4-29 - The experimental equilibrium potentials from the high temperature electrochemical cell (filled and half-filled symbols) and the electrochemical glass cell (hollow symbols) at temperatures from 25°C to 70°C(hollow symbols) and 25°C to 130°C (solid symbols). 90
Figure 4-30 – EDX pictures of the elements present in the solid deposition. 91
Figure 4-31 – IR-Spectra of the iron oxide deposits from the high temperature electrochemical cell in its calcined(red) and uncalcined(black) form. 92
Figure 4-32 – The Raman spectra of the calcined sample (green) with two reference samples (black and red) is shown in the figure above. 94
Figure 4-33 – Raman shifts of the uncalcined sample(green) and the reference for goethite(blue)[127] and two different pristine iron oxides (black and red). 94
Figure 4-34 - The schematic flow diagram is shown above for the determination of the corrosion reaction to correspond to actual hydrogen ion concentration in the solution. 95
Figure 4-35 – The results constant corrosion constants resulting from the reaction equilibria is shown above and their comparison with experimental results. 97
Figure 4-36 – The comparison of the calculated dissociation constants of silicic acid with literature data from Busey and Mesmer [42] and the calculated values from this work. 98
Figure 4-37 – A schematic diagram of the QCM employed for the vapour phase measurement with the integrated circuit to induce the resonance frequency. 100
Figure 4-38 – Experimental logarithmic equilibrium constants data from the QCM method for the vapour phase is depicted. 101
Figure 4-39 – The comparison of experimental and calculation logarithmic equilibrium constants for the liquid and vapour phases is shown in the figure above. 102
Figure 7-1 – UV-Vis spectrum of diluted calibrated solutions (solution F) and sample solution at 110°C at pH=12 116
Figure 7-2 – The concentration (y-axis) of the calibrated solution for different intensities (x-axis) at 410nm showing a linear dependency 116

Figure 7-3 - The linear sweep measurements in the absence of dissolved silica at different temperatures and pH. 117
Figure 7-4– The linear sweep measurement in the presence of silica at different temperatures and pH. 118
Figure 7-5 – The Pourbaix Diagram of iron 118
Figure 7-6 – Water sorption results for LUDOX AS-40 at 25°C and 50°C. 121
Figure 7-7 – The X-ray diffraction pattern for LUDOX AS-40. 121
Figure 7-8 – The SEM samples from the high temperature flow-through cell 123
Figure 7-9 – The SEM and EDX samples of stainless steel from the glass cell. 123
Figure 7-10 – The figure above shows the comparison of lnK, $lnK_{298.15K}$ and lnK_p for cyclic trisilicic acid. 127
Figure 7-11 – The figure above shows the comparison of lnK, $lnK_{298.15K}$ and lnK_p for cyclopentasilicic acid. 127

Tables

Table 3-1 – The abbreviation of silicic acid reactions considered in this work. 23
Table 3-2 – The mixed (linear and branched-cyclic) and cyclic (simple and fused cyclic) silicic acid species considered in this work 32
Table 4-1 – The optimized geometries of the silicic acid species involved with their respective nomenclature and molar mass[36]. 45
Table 4-2 – The standard enthalpy, free energy and entropy of reaction for the cyclisation reaction 48
Table 4-3 – The standard enthalpy, free energy and entropy of reaction for the condensation reaction 50
Table 4-4 – The standard enthalpy, free energy and entropy of reaction for the dissociation reactions for cyclic (simple-and fused-cyclic –see page 22) species with the consideration of solvent effects 53
Table 4-5 – The standard enthalpy, free energy and entropy of reaction for the dissociation reactions for mixed (linear and branched-cyclic) species with the consideration of solvent effects 55
Table 4-6 – The time period taken to reach equilibrium at different temperature and pH-values for the solubility of silicic acid is shown in the table below. 59
Table 4-7 – The comparison between different flow through electrochemical cell designs and the cell from this work (last column) is shown in the table below 77

Table 7-1 – The fitting parameters for the UV-Vis measurement to determine the concentration of dissolved silica (silicic acid). 117
Table 7-2 – The OH^- concentration for hydrogen concentration in half-cell 2of unity on the right and 10^{-7} on the left (values with silica)..... 120
Table 7-3 – The Fe^{2+} concentration for hydrogen concentration in half-cell 2of unity on the right and 10^{-7} on the left (values with silica)..... 120
Table 7-4 – The fitting equations retrieved from the ESI-MS data of the silicic acid species considered..... 122
Table 7-5 – The Vapour-Liquid compositions for silicic acid-H_2O for different temperatures at pH=7. Feed composition is given in the last column. 123
Table 7-6 – The Vapour-Liquid compositions for silicic acid-H_2O for different temperatures at pH=12. Feed composition is given in the last column. 124
Table 7-7 – The Vapour-Liquid compositions for silicic acid-H_2O for different temperatures at pH=12. Feed composition is given in the last column. 124
Table 7-8 - The values below are the energies for all silicic acid species and water. Geometries are optimized with the B3LYP/6-311G** level of theory. These values are used to calculate the energy of reactions for polymerisation and cyclisation. 124
Table 7-9 - The values below are the energies for and water, hydroxonium ion, all neutral and anionic silicic acid species. Geometries are optimized with the B3LYP/6-311G** level of theory with solvent effects (PCM). These values are used to calculate the energy of dissociation reactions. 125

Curriculum Vitae

Name:	Jaybalan Tamahrajah
Gender	male
Date of Birth / -Place of Birth	13.04.1985 / Kuala Lumpur, Malaysia
Nationality	Malaysian
Education	
04 / 2003 – 06 / 2004	A-Level Examinations in Malaysia – international entrance examination University of Cambridge
09 / 2005 – 12 / 2008	Bachelor of Science (B.Sc.) Bremerhaven University of Applied Sciences
01 / 2009 – 01 / 2011	Master of Science (M.Sc.)-Bremerhaven University of Applied Sciences
03 / 2011 – 10 / 2015	PhD, Technical Chemistry (Dr. rer. nat) University of Oldenburg
Working experience	
05 / 2006 – 05 / 2010	Technical Assistant at Birds Eye Iglo / Frozen Fish International GmbH
08 / 2007 – 02 / 2008	Tutor at the Bremerhaven University of Applied Sciences (Mathematics und Technical Mechanics)
04 / 2011 – 08 / 2014	Research Associate at the University of Oldenburg - (Working group of Technical Chemistry - Prof. Dr. Axel Brehm)
02 / 2012 – 02 / 2013	Lecturer at the Bremerhaven University of Applied Sciences
Language	Tamil(Mother tongue), English, German, Malay, Indonesian
Award(s) 2008	DAAD (German Academic Exchange Service) Best student Award (Prize of 1000 €).
Scholarship(s)	PhD scholarship of the FAZIT-Funding Organisation von September 2014 – August 2015.

Publications

1. Jubaer H., Tamahrajah J., Schütz W., Frickenhaus S., Students in Science - A result of Bologna Convention, Joints Proceedings – Akademia Morska Gdynia and Bremerhaven University of Applied Sciences, No.24, pp 17, Oct 2011, ISSN 0176-1323.
2. Tamahrajah J., A modified Jaegers Equation of State: A comparison with the Peng-Robinson Equation of State, Joints Proceedings – Akademia Morska Gdynia and Bremerhaven University of Applied Sciences, No.24, pp 26-30, Oct 2011, ISSN 0176-1323.
3. Tamahrajah, J. and Brehm, A., In-Situ Hydroelectrothermal Deposition of Silicate Layers on Stainless Steel Surfaces. Advances in Materials Physics and Chemistry, 5, 374-382, Sept 2015, ISSN Print: 2162-531X, ISSN Online: 2162-5328. http://dx.doi.org/10.4236/ampc.2015.59038.
4. Tamahrajah J.,Taffa D.H., Brehm A., Corrosion model of stainless steel in the presence of dissolved silica, International Journal of Engineering and Scientific Research, in Preparation.

Posters

1. Tamahrajah J., Rosenkranz D., Brehm A., Klüner T., Lasar C., Determination of the free energy of formation of silicic acid species at standard conditions, Poster programme at the 26. German Zeolite Conference, 26.-28. February 2014.
2. Tamahrajah J., Rosenkranz D., Brehm A., Klüner T., Lasar C., Chemical equilibria of silicic acids: effects of temperature and pH. Contribution to the understanding of hydrothermal zeolite syntheses, Poster programme at the 27. German Zeolite Conference, 25.-27. February 2015.

Erklärung:

Hiermit versichere ich, dass ich diese Arbeit selbständig verfasst und keine anderen als die angegebene Quellen und Hilfsmittel benutzt habe. Des Weiteren erkläre ich, dass die Dissertation weder in ihrer Gesamtheit noch in Teilen einer anderen wissenschaftlichen Hochschule zur Begutachtung in einem Promotionsverfahren vorliegt oder vorgelegen hat

Oldenburg, den 15.09.2015 _____

Jaybalan Tamahrajah